Pre-assembly of biomolecular condensate seeds drives RSV replication

https://doi.org/10.1038/s41586-025-10071-5

Received: 24 January 2025

Accepted: 17 December 2025

Dhanushika Ratnayake[1], Marie Galloux[2,17], Sanne Boersma[1,17], Marko Noerenberg[3,4,17], Christina Sizun[5], Carlos Sacristan[1], Julien Sourimant[2], Anke J. Lakerveld[6], Anne T. Gelderloos[6], Leonie Apperloo[1], Yana Demyanenko[7], Matthijs J. D. Baars[1], Rupa Banerjee[1], Birgit Dreier[8], Sven Furler[8], Natalie I. Mazur[9,10], Louis J. Bont[9,10,11], Shabaz Mohammed[4,7,12], Andreas Plückthun[8], Jean-François Éléouët[2], Geert J. P. L. Kops[1], Alfredo Castello[3,4], Puck B. van Kasteren[6], Marie-Anne Rameix-Welti[13,14,15] & Marvin E. Tanenbaum[1,16] ✉

During infection, many RNA viruses, including respiratory syncytial virus (RSV), form specialized biomolecular condensates, viral factories (VFs), where viral transcription and replication occur[1,2]. Paradoxically, high protein concentrations are typically required for condensate nucleation[3], yet attaining sufficient protein levels in infection is thought to require VFs for viral transcription and replication. Here, to uncover how viruses solve this paradox to establish VFs, we visualized early infection of RSV in real time with single genomic viral ribonucleoprotein (vRNP) resolution. Our results reveal that VFs are nucleated from infecting vRNPs rather than de novo in the cytoplasm. VF nucleation further requires in-virion pre-assembly of viral protein–protein interaction networks on vRNPs to form 'pre-replication centres' (PRCs). PRCs are potent condensate nucleation seeds due to their efficient recruitment and retention of viral proteins. The high affinity of PRCs also results in increased association of the viral polymerase and its co-factors, allowing efficient viral transcription even in the absence of VFs. Together, these activities create a feed-forward loop that drives rapid VF formation. PRC assembly depends on in-virion viral protein levels and is highly heterogeneous among virions, explaining cell-to-cell heterogeneity in infection progression, and identifying heterogeneous virions as an important origin of infection heterogeneity. Together, our results show that in-virion pre-assembly of PRCs kick-starts viral condensate nucleation upon host-cell entry and explains cell-to-cell heterogeneity in RSV infection.

Viruses of the *Mononegavirales* order, which include Ebola virus, measles virus and RSV, are among the most infectious human and animal pathogens. Although effective vaccines and antiviral therapies are available for a few viruses from this order, many remain untreatable and cause a major health and economic burden on society. Like other viruses of the *Mononegavirales* order, RSV has a non-segmented negative-sense RNA genome, encapsidated by viral nucleoprotein (N), together called the nucleocapsid (NC)[4–6]. In addition to N, the viral genome also associates with the viral RNA-dependent RNA polymerase (RdRp; 'large' protein (L)), and its essential co-factors: the phosphoprotein (P) and the viral transcription factor M2-1. Together with the NC, these proteins form the vRNP complex (Extended Data Fig. 1a), the minimal infectious unit of RSV that functions as the viral transcriptase and replicase[7,8].

Many viruses, including RSV, form cytoplasmic membrane-less compartments (called inclusion bodies in RSV), which are VFs, acting as important sites of viral transcription and replication[1,2]. Although the importance of VFs for viral infection has been well documented, it is poorly understood how these organelles are initially nucleated. VFs are biomolecular condensates formed by the viral proteins N and P[1,9,10]. However, formation of condensates is typically very sensitive to the concentration of their constituent biomolecules[11–13]; nucleation of condensates generally occurs when the concentration of the constituent biomolecules exceeds a threshold concentration, whereas

---

[1] Oncode Institute, Hubrecht Institute, Royal Netherlands Academy of Arts and Sciences (KNAW) and University Medical Center Utrecht, Utrecht, the Netherlands. [2] Université Paris-Saclay, INRAE, UVSQ, VIM, Jouy-en-Josas, France. [3] MRC–University of Glasgow Centre for Virus Research, Glasgow, UK. [4] Department of Biochemistry, University of Oxford, Oxford, UK. [5] Institut de Chimie des Substances Naturelles, CNRS, Université Paris-Saclay, Gif-sur-Yvette, France. [6] Center for Infectious Disease Control, National Institute for Public Health and the Environment, Bilthoven, the Netherlands. [7] The Rosalind Franklin Institute, Didcot, UK. [8] Department of Biochemistry, University of Zurich, Zurich, Switzerland. [9] Center for Translational Immunology, University Medical Centre Utrecht, Utrecht, the Netherlands. [10] Department of Pediatric Infectious Diseases and Immunology, Wilhelmina Children's Hospital, University Medical Center Utrecht, Utrecht, the Netherlands. [11] Respiratory Syncytial Virus Network (ResViNET) Foundation, Zeist, the Netherlands. [12] Department of Chemistry, University of Oxford, Oxford, UK. [13] M3P unit, Institut Pasteur, Université Paris Cité, Paris, France. [14] UMR 1173 (2I), INSERM, Université de Versailles St. Quentin, Université Paris-Saclay, Paris, France. [15] Hôpital Ambroise Paré, Assistance Publique des Hôpitaux de Paris, Paris, France. [16] Department of Bionanoscience, Kavli Institute of Nanoscience Delft, Technische Universiteit Delft, Delft, the Netherlands. [17] These authors contributed equally: Marie Galloux, Sanne Boersma, Marko Noerenberg. ✉e-mail: m.tanenbaum@hubrecht.eu

condensates dissolve when the concentration drops below this critical concentration[11–14]. Yet, during early infection, viral protein levels are very low, raising the question of how VFs can be nucleated. Moreover, VFs themselves are thought to be needed to accumulate high viral protein concentrations by driving efficient viral transcription and replication, so it is unclear how viruses can increase the concentration of viral proteins in early infection to allow VF formation. How viruses coordinate early infection transcription and replication with VF formation to successfully establish infection is a major open question.

DARPin-P is a synthetic binder of RSV P

To understand RSV infection establishment, we aimed to visualize RSV infection with single vRNP sensitivity to determine when and where VFs are first formed, and how VF formation relates to viral transcription and replication dynamics. We have recently shown for a different negative-sense RNA virus, influenza A virus, that single vRNPs can be visualized in living cells through expression of a fluorescently labelled protein that binds to individual vRNPs in multiple copies[15]. As many copies of N and P are bound to each RSV vRNP, we reasoned that, if a fluorescent protein could be developed that binds specifically to either N or P, such a protein would be recruited in many copies to a vRNP, yielding a sufficiently bright fluorescent signal to visualize single vRNPs during early infection[16,17]. DARPins were assessed as potential N or P binders due to their small size (14–18 kDa), stability and low intracellular aggregation tendencies[18]. As a target, a previously described protein complex composed of the GST-fused C-terminal domain of P (P_{CTD}) associated with a NC-like structure consisting of rings of 10–11 N proteins (Nrings) was used[5,19] (Extended Data Fig. 1b). High-affinity DARPin binders were selected via ribosome display, from which one, DARPin-H6, was selected for further characterization based on its strong binding interaction (Extended Data Fig. 1c).

Mass spectrometry of DARPin-H6 pulldowns performed on RSV virion lysates demonstrated that DARPin-H6 efficiently and selectively pulled down RSV P, with small amounts of other viral proteins also detected, suggesting that DARPin-H6 binds directly to P in its native context (Fig. 1a). This interaction was further confirmed and localized to 40 residues at the N-terminal end of the P_{CTD} (amino acids 162–209) by 2D nuclear magnetic resonance (NMR) spectroscopy, and by gel shift assays using native agarose gel electrophoresis with recombinantly expressed variants of N and P (Fig. 1b,c and Extended Data Fig. 1d–j). The binding kinetics of DARPin-H6 with P_{CTD} were assessed via biolayer interferometry (BLI), which showed a high-affinity interaction with a dissociation constant (K_d) of 12.3 nM (Fig. 1d). On the basis of the direct interaction with P, DARPin-H6 is referred to as DARPin-P.

DARPin-P labels a subset of vRNPs

To assess the ability of DARPin-P to label vRNPs during infection, A549 cells were infected with wild-type (WT) RSV and stained with recombinant, fluorescently labelled DARPin-P together with fluorescently conjugated anti-RSV F and N antibodies to mark vRNPs inside the host cell or inside virions attached to host cells (Extended Data Fig. 2a–e). We identified vRNPs that were strongly stained by DARPin-P, confirming that DARPin-P could be used for vRNP detection early (4 h post-infection (hpi)) during infection (Extended Data Fig. 2e, purple inset). However, only a subset of vRNPs was labelled by the DARPin-P in infected cells (20 ± 14%; Extended Data Fig. 2f). Similarly, when a fluorescently tagged DARPin-P (DARPin-P-fluoro) was expressed in cells (Fig. 1e), it robustly labelled only a subset of vRNPs in the cytoplasm of infected cells (16 ± 4%; Fig. 1f,g and Extended Data Fig. 2g–i), demonstrating the potential for live-cell vRNP imaging by DARPin-P, and confirming that the heterogeneous labelling was not caused by fixation artefacts. DARPin-P-fluoro expression in cells did not detectably interfere with RSV infection progression, as assessed by viral transcript and protein accumulation during infection (Extended Data Fig. 2j–m). Together, these results show that DARPin-P-fluoro expressed in cells represents a powerful tool to visualize vRNPs in live RSV infected cells. Moreover, labelling of a subset of vRNPs by DARPin-P-fluoro suggests that vRNPs are heterogeneous and provides a technology with which to study vRNP heterogeneity.

A virion subset contains DARPin-P$^+$ vRNPs

To study the origin of vRNP heterogeneity and its consequence for infection establishment, an additional vRNP labelling strategy is required to detect all vRNPs, and compare infection by DARPin-P$^-$ and DARPin-P$^+$ vRNPs in live cells. Serendipitously, we found that cellular expression of exogenous, fluorescently tagged P robustly labelled all vRNPs. To minimize the effect of the fluorescent tag on P disrupting P binding to vRNPs, we engineered P (exogenous P (P^{exo})) with a short peptide tag, SunTag[20,21], and co-expressed a genetically encoded antibody that binds to the SunTag peptide, called SunTag antibody (STAb), fused to a fluorescent protein (referred to as P^{exo}-fluoro; Fig. 2a; the fluorescent proteins used in each experiment are listed in Supplementary Table 1). P^{exo}-fluoro labelled the large majority of vRNPs in infected cells (93 ± 4%; Fig. 2b,c and Extended Data Fig. 3a), without detectably affecting viral transcription or replication (Extended Data Fig. 3b–f). Somewhat surprisingly, when the DARPin-P-fluoro and P^{exo}-fluoro were co-expressed in cells and infected with RSV (Fig. 2d), DARPin-P still labelled only a small subset of vRNPs (19 ± 11%), even though DARPin-P binds to P and almost all vRNPs were associated with exogenous P (Fig. 2e). These observations suggest that the DARPin-P$^+$ vRNPs have substantially higher total P levels (combined endogenous P and P^{exo}), and/or DARPin-P binds to a specific conformation of P present predominantly on a subset of vRNPs (as discussed later). Irrespective of this, these results confirm that vRNPs exist in heterogenous states and that the DARPin-P-fluoro and P^{exo}-fluoro tools combined allow real-time tracking of heterogeneous vRNPs in living cells.

Using the DARPin-P-fluoro and P^{exo}-fluoro tools, we set out to characterize RSV infection establishment and VF formation. Consistent with earlier electron microscopy studies[22–24], we found that many infected cells contained multiple vRNPs (66 ± 24%), even when infected at low multiplicity of infection (MOI; 0.1), suggesting that individual virions often contain more than 1 vRNP (Fig. 2f). To exclude that the multiple vRNPs observed in single cells were formed through genome replication of the incoming vRNP, vRNP number in infected cells was assessed in the presence of PC786, a potent RSV polymerase inhibitor that prevents vRNP transcription and replication[25] (Extended Data Fig. 3d–f). Time-lapse microscopy revealed that for most PC786-treated infected cells, a single bright vRNP spot was observed upon viral entry, followed by a rapid increase in foci number (Fig. 2g,h, Extended Data Fig. 3g and Supplementary Video 1), suggesting that multiple vRNPs enter together from a single virion and rapidly split after entry. High time-resolution imaging showed that different vRNPs entering a host cell colocalized in the host cell cytoplasm for several minutes after entry (median of 6.0 min), consistent with vRNPs originating from the same virion (Extended Data Fig. 3h and Supplementary Video 2). Quantification of the number of vRNP foci per infected cell revealed that 38% contained one vRNP, 24% two vRNPs, 13% three vRNPs, 5% four vRNPs and 20% more than four vRNPs at an MOI of 0.1 (Fig. 2i). Although the majority of vRNPs originating from a single virion had split by 20 min post-entry, for virions containing large numbers of vRNPs, this splitting process could take up to 3 h in rare cases (Fig. 2j). It is possible that a subset of vRNPs never undergo splitting, which could result in a (slight) underestimation of the number of vRNPs per virion. The distribution in the number of vRNPs per virion was strikingly similar for different virus strains, for virus produced in different cell lines and primary cell cultures, and even for virus isolated directly from patients infected with RSV (Extended Data Fig. 4a–e). Although multiple vRNPs have been detected in RSV

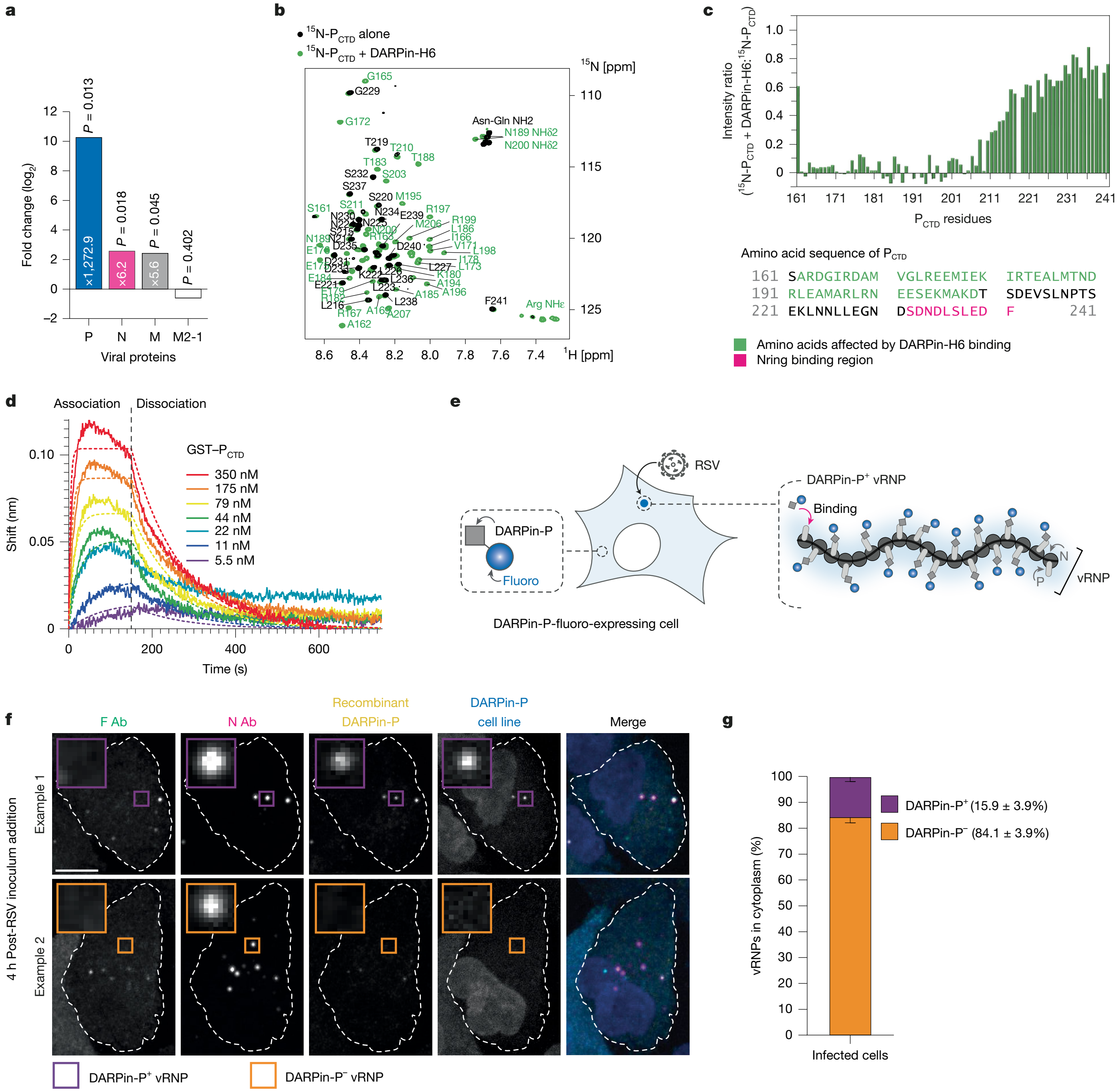

Fig. 1 | RSV vRNPs are heterogenous. a, Ribosome display identified DARPin-H6 as an RSV vRNP binder. Interaction of DARPin-H6 with native RSV vRNPs was assayed by pulldowns on virion lysates followed by mass spectrometry. The fold change of detected viral proteins in the DARPin-H6 pulldown versus beads-only control is plotted. *P* values were calculated by moderated *t*-test and adjusted by the Benjamini–Hochberg method. **b**,**c**, NMR spectroscopy demonstrated interaction of DARPin-H6 with RSV P_{CTD}. ^1H-^{15}N HSQC spectrum of 50 μM ^{15}N-P_{CTD} measured after addition of equimolar amounts of DARPin-H6 (green), superimposed on the spectrum of ^{15}N- P_{CTD} alone (black; **b**). Signals that were fully broadened out by addition of DARPin-H6 are indicated in green. The intensities in the presence of DARPin-H6 divided by the intensities of the reference spectrum (intensity ratios) for each peak in the HSQC spectra are shown as a bar diagram; the amino acid sequence of P_{CTD} is shown below with residues affected by DARPin-H6 binding in green and the C-terminal Nring binding residues in magenta (**c**). **d**, Binding kinetics of the P_{CTD} to DARPin-H6 was assessed using BLI with immobilized DARPin-H6 and GST–P_{CTD} as analyte at the indicated concentrations. The solid lines indicate original data and the dashed lines show fitted curves. The DARPin-H6–RSV P_{CTD} interaction yielded a K_d of 12.3 nM. Given its binding partner, DARPin-H6 is herein referred to as DARPin-P. **e**, Schematic of A549 cells stably expressing fluorescently tagged DARPin-P (DARPin-P-fluoro), enabling live-cell visualization of DARPin-P$^+$ vRNPs. **f**,**g**, RSV-infected DARPin-P-fluoro cells were fixed and stained with RSV F, N and recombinant DARPin-P. Representative images (**f**) and quantification (**g**) are shown. Quantification includes only cytoplasmic vRNPs (F$^-$), and was performed at 4 h post-RSV inoculum addition to ensure that only single vRNPs were analysed (see Fig. 2j). Dashed outlines in **f** identify cells of interest. Scale bar, 10 μm (**f**). Data are mean ± s.d.; *n* = 1,342 foci (**g**). Ab, antibody. Experimental repeats and fluorophores are listed in Supplementary Table 1.

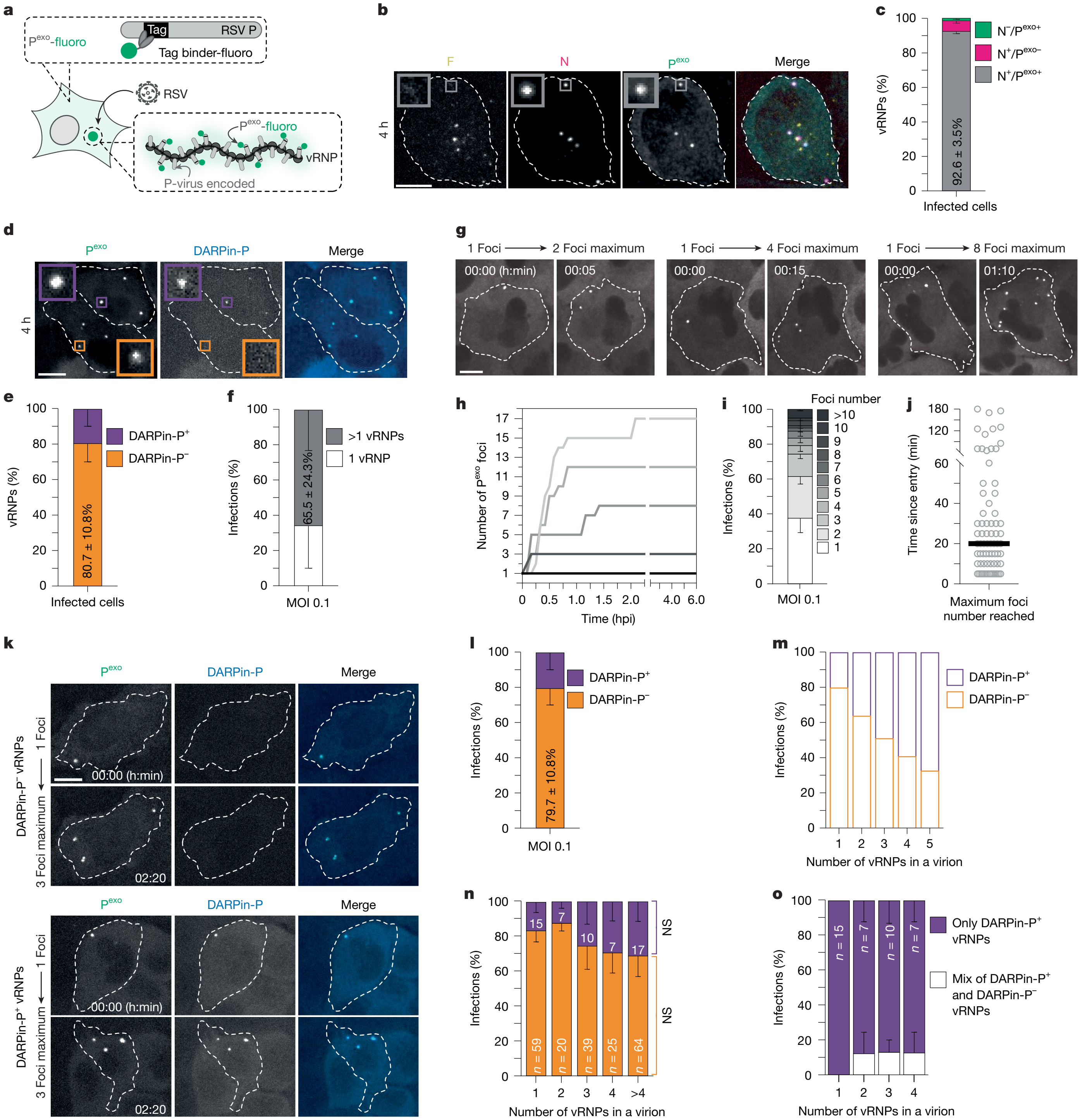

Fig. 2 | A subset of virions carries DARPin-P⁺ vRNPs. **a**, Schematic of the Pexo-fluoro system for RSV vRNP visualization. **b**,**c**, Pexo-fluoro foci colocalize with vRNPs (labelled by anti-RSV N antibody). Anti-RSV F antibody staining was included to identify intact virions, which were not labelled by Pexo-fluoro. Representative images (**b**) and quantification (**c**) of colocalization are shown. Data are mean ± s.d.; *n* = 1,038 foci. **d**,**e**, Stable cell line co-expressing Pexo-fluoro and DARPin-P-fluoro infected with WT RSV. Representative images (**d**) and quantification (**e**) of colocalization are shown. Data are mean ± s.d.; *n* = 1,087 foci. **f**, Quantification of vRNPs per infected cells at 4 h post-viral inoculum addition. Data are mean ± s.d.; *n* = 306 cells. **g**–**j**, WT RSV infection in Pexo-fluoro cells treated with the viral polymerase inhibitor PC786. Representative images (**g**), five example traces of Pexo-fluoro foci number over time (**h**), quantification of maximal vRNP number per cell (**i**) and the time for all virion containing vRNPs to separate (**j**) are shown. See also Supplementary Video 1. Data are mean ± s.d. (**i**) or median (**j**); *n* = 359 cells (**i**) or 74 cells (**j**). **k**–**o**, Single virion infections were assessed to evaluate whether all vRNPs originating from the same virion share the same DARPin-P state. Representative images (**k**) and classification (**l**) of infected cells by the vRNP DARPin-P state are shown. Infected cells were designated DARPin-P⁺ if one or more vRNP was DARPin-P⁺. Data are mean ± s.d.; *n* = 290 cells. Comparison between theoretical (**m**) and experimental (**n**) frequencies of infection with at least one DARPin-P⁺ vRNP revealing non-random distribution of DARPin-P⁺ vRNPs across virions. Data are mean ± s.d.; two-way analysis of variance (ANOVA) with Tukey's multiple comparisons test was used to assess variation in infection fractions across vRNP numbers (**n**). NS, not significant. For infections classified as DARPin-P⁺, the fraction that contained exclusively DARPin-P⁺ vRNPs versus a mixed population of DARPin-P⁺ and DARPin-P⁻ vRNPs is shown (**o**). Data are mean ± s.d. Experiments were performed at low MOI (0.1) to ensure that most cells were infected by a single virion. Scale bars, 10 µm (**b**,**d**,**g**,**k**). Experimental repeats and fluorophores are listed in Supplementary Table 1.

virions by electron microscopy[22–24], our results provide quantitation of vRNP copy number per virion across viral strains, and reveal vRNP dissociation kinetics upon host cell entry.

As many virions contained multiple vRNPs and only a subset of all vRNPs are DARPin-P$^+$, we asked whether individual virions typically contained either DARPin-P$^+$ and DARPin-P$^-$ vRNPs only or mixed populations of vRNPs. Examining the fraction of DARPin-P$^+$ vRNPs per virion revealed that most virions contained only DARPin-P$^+$ or only DARPin-P$^-$ vRNPs (Fig. 2k–o). DARPin-P$^+$ and DARPin-P$^-$ vRNPs were also observed for viruses produced in different cell types, different RSV strains and for virus isolated from patients infected with RSV (Extended Data Fig. 4f–i), validating the broad physiological relevance of vRNP heterogeneity. In summary, these results show that RSV virions are heterogeneous in two different ways, they contain different numbers of vRNPs and their vRNPs can be in different states (DARPin-P$^+$ or DARPin-P$^-$).

DARPIn-P$^+$ vRNPs resemble early VFs

To understand early infection establishment and to determine whether virion heterogeneity impacts infection establishment, we followed single infected cells over time using the P^{exo}-fluoro and DARPin-P-fluoro systems. First, the typical course of infection as observed by P^{exo}-fluoro is described, after which the differences in infection establishment between DARPin-P$^+$ and DARPin-P$^-$ vRNPs are detailed.

Infection typically starts with a single vRNP foci labelled by P^{exo}-fluoro, which, in the majority of cases, rapidly splits into multiple foci (Fig. 3a,b and Supplementary Video 3), as discussed above. In a subset of cells (43 ± 8%), the intensity and size of one or more P^{exo}-fluoro foci increased several hours after cell entry (Fig. 3a–c, Extended Data Fig. 5a,b and Supplementary Video 3, successful infections). Growing P^{exo}-fluoro foci subsequently fused with other P^{exo}-fluoro foci present in the same cell to form large, slow-moving foci, in a process that was dependent on viral polymerase activity (Fig. 3a, 'vRNP fusion', Fig. 3b,d, Extended Data Fig. 5a,b and Supplementary Video 3). Typically, many new, smaller P^{exo}-fluoro foci, which stained positive for viral genomic RNA, appeared several hours after large P^{exo}-fluoro foci were formed (Fig. 3a, 'vRNP replication', Fig. 3b,e, Extended Data Fig. 5a–c and Supplementary Video 3). On the basis of this series of events, we hypothesized that large P^{exo}-fluoro foci formed by growth and vRNP fusion represent VFs, the sites of viral replication, and that the smaller P^{exo}-fluoro foci formed afterwards represent progeny vRNPs synthesized through viral replication. To test whether large P^{exo}-fluoro foci indeed represent VFs, cells were fixed at the end of the timelapse videos, and large P^{exo}-fluoro foci were assessed for the presence of viral RNA and proteins known to localize to VFs. Large P^{exo}-fluoro foci stained positive for viral genomes ((−)vRNA), antigenomes ((+)vRNA), viral transcripts and viral N and M2-1 proteins (Fig. 3f,g and Extended Data Fig. 5d,e), strongly suggesting that they represent VFs. Moreover, antigenomes, which are generated through viral replication, were exclusively observed in large P^{exo}-fluoro foci formed after vRNP fusion, and not in smaller P^{exo}-fluoro foci present before vRNP fusion (Fig. 3f–h), indicating that replication only occurs after VF formation. We then assessed whether a subset of VFs showed biphasic organization with inclusion body-associated granules[1,26,27]. Inclusion body-associated granules were visualized using fluorescently tagged M2-1 (M2-1^{exo}-fluoro) and observed to form inside a subset of large P^{exo}-fluoro foci only after vRNP fusion and replication had occurred (Extended Data Fig. 5f–h). Thus, we define large vRNPs that are formed through growth and fusion with other vRNPs as VFs, and define the moment of vRNP fusion as the moment of VF biogenesis. Although a single VF was typically formed during early infection, multiple VFs were sometimes observed in cells by 20 hpi (Extended Data Fig. 5i). In all cases in which vRNPs fused to form VFs, vRNP progeny was also subsequently formed (Fig. 3e), indicating that viral replication occurs reliably after VF formation. Although VF and vRNP progeny formation was observed in a subset of infections (43 ± 8%), in the majority of infections (57 ± 8%), vRNP entry and initial splitting occurred normally, but vRNP growth and fusion to form VFs failed to occur and no progeny vRNPs were produced (Fig. 3a–c and Supplementary Video 3, stalled infections). Together, these results show that VFs are nucleated by incoming vRNPs, that VF formation precedes viral replication and that VF nucleation represents an important bottleneck towards infection success.

To assess the effect of the number and DARPin-P state of incoming vRNPs on infection success, we combined the P^{exo}-fluoro and DARPin-P-fluoro imaging systems (Fig. 3i and Supplementary Video 4). To simplify calling of 'infection success' (defined as infections that produce VFs and progeny vRNPs) in single infected cells, we made use of G protein staining at the plasma membrane, which we found is a simple and reliable proxy for VF and vRNP progeny formation (Extended Data Fig. 5j,k). G protein could be labelled and quantified in living cells using a non-neutralizing G antibody conjugated to a fluorophore (AbG-fluoro) added to the cell culture medium (Extended Data Fig. 5l–p). When examining the effect of vRNP number per virion on infection success, somewhat surprisingly, we found that the chance of infection success was similar for virions containing one or more vRNPs (Fig. 3j). We therefore turned our attention to the DARPin-P state of incoming vRNPs. Virions containing DARPin-P$^+$ vRNPs and DARPin-P$^-$ vRNPs entered host cells with similar kinetics and showed similar vRNP numbers per virion (Extended Data Fig. 5q,r). However, in contrast to vRNP number, DARPin-P positivity was a very strong predictor of infection success: 100% of infections initiated by DARPin-P$^+$ vRNPs were successful, whereas only 35% of infections originating from DARPin-P$^-$ vRNPs were successful (Fig. 3k and Extended Data Fig. 5s,t). Furthermore, successful DARPin-P$^+$ infections progressed faster than successful DARPin-P$^-$ infections (Fig. 3k and Extended Data Fig. 5s,t). Higher chances of infection success for DARPin-P$^+$ vRNPs was also confirmed in two RSV clinical isolates (Fig. 3l,m). Virions produced in various cell lines had (slightly) different fractions of DARPin-P$^+$ and DARPin-P$^-$ vRNPs and the probabilities of infection success followed the trend of the faction of virions containing DARPin-P$^+$ vRNPs, further confirming the importance of DARPin-P$^+$ vRNPs in determining infection success (Fig. 3n and Extended Data Fig. 4f). Examination of DARPin-P staining throughout infection revealed that both DARPin-P$^+$ vRNPs and VFs were strongly labelled (Extended Data Fig. 5u), suggesting that DARPin-P$^+$ vRNPs and VFs share common features. The failure of DARPin-P$^-$ vRNPs to progress in infection was not due to (large) genome deletions that are known to occur in RSV (resulting in defective viral genomes)[28,29], as both DARPin-P$^-$ and DARPIn-P$^+$ vRNPs mostly contained intact vRNAs, as assessed by single-molecule fluorescence in situ hybridization (smFISH; Extended Data Fig. 6a–m). Collectively, these results show that the DARPin-P state rather than the number of infecting vRNPs per virion dictates the outcome of infection. As DARPin-P stained both (a subset of) incoming vRNPs and VFs, and as DARPin-P$^+$ incoming vRNPs went on to form VFs and successfully replicate to produce viral progeny, we refer to DARPin-P$^+$ vRNPs as pre-replication centres (PRCs). We refer to DARPin-P$^-$ vRNPs as 'passive vRNPs', relating to their poor ability to drive infection success.

PRCs show high transcriptional activity

To understand why PRCs result in high rates of infection success, we examined the transcriptional activity of PRCs and passive vRNPs during infection. To determine viral transcription rates in living cells, we made use of an assay to visualize single translating viral mRNAs, which we have previously developed[16]. In brief, an extra gene was introduced into the RSV genome that encodes for multiple repeats of the SunTag peptide epitope. Viral transcription produces mRNAs encoding for the SunTag array (SunTag mRNA), which are translated by host cell ribosomes. Upon translation, the SunTag peptides are co-translationally bound by the STAb-fluoro molecules expressed

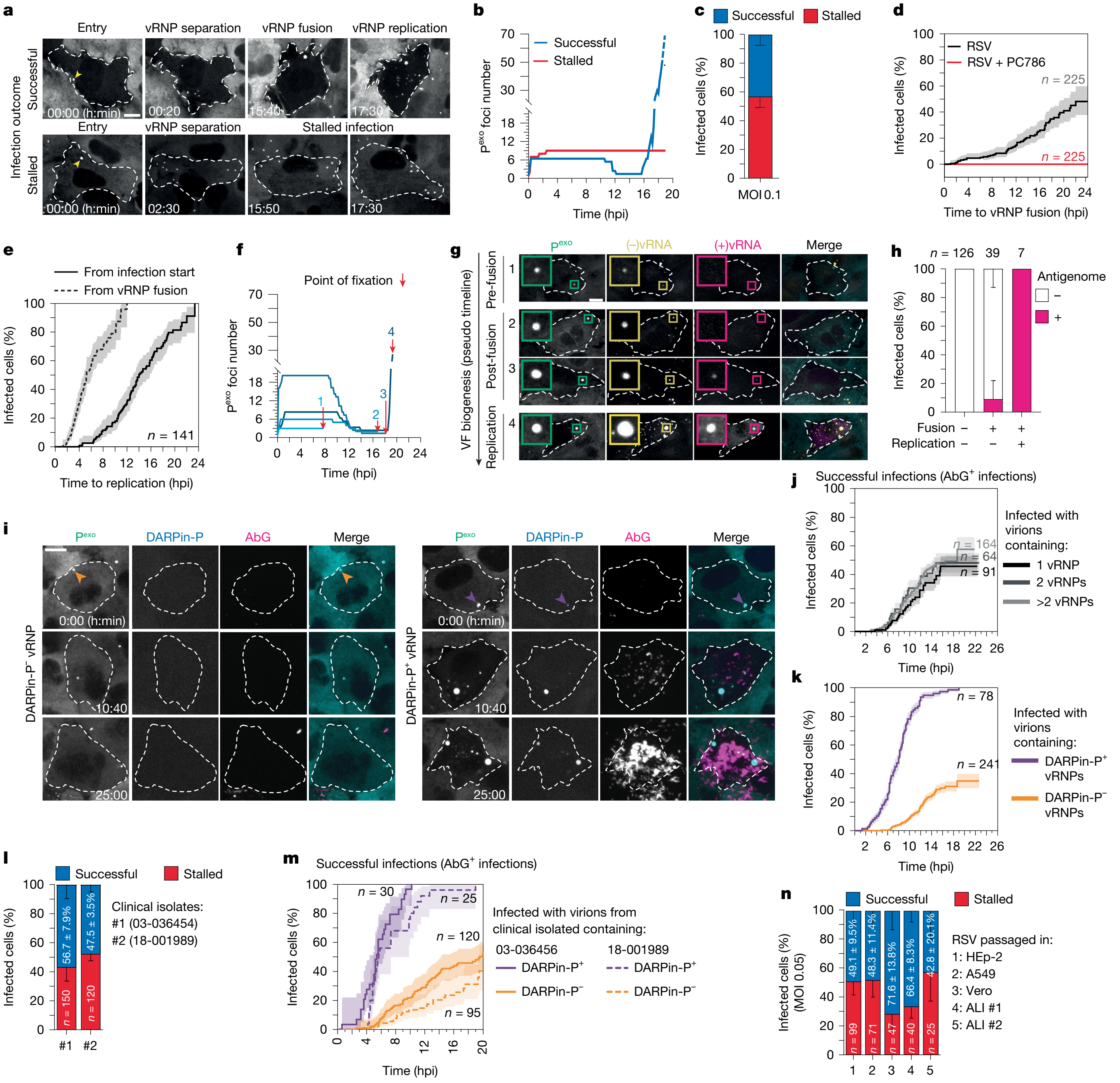

Fig. 3 | DARPin-P^{+} vRNPs give rise to successful infections. a–c, Timelapse imaging of P$^{\text{exo}}$-fluoro cells infected with WT RSV. Representative images from two videos (**a**) and corresponding P$^{\text{exo}}$-fluoro foci counts (**b**) over time are shown. The top image series shows a successful infection and the bottom image series shows a stalled infection (**a**). The arrowheads mark initial P$^{\text{exo}}$-fluoro foci. See also Supplementary Video 3. The frequency of successful and stalled infections is also shown (**c**). Data are mean ± s.d.; *n* = 225 cells (**c**). **d**,**e**, vRNP fusion (**d**) and replication dynamics (**e**) in infections with more than one infecting vRNP. The graphs show time from cell entry to vRNP fusion (**d**). For infections showing fusion, the time from vRNP entry (solid line) or fusion (dashed line) to replication, indicated by an increase in P$^{\text{exo}}$-fluoro foci number, is shown (**e**). vRNP fusion always precedes replication. **f**–**h**, Dynamics of vRNP fusion (**f**), VF formation (**g**) and viral replication (**h**). Following P$^{\text{exo}}$-fluoro imaging, genomes ((−)vRNA) and antigenomes ((+)vRNA) were detected by smFISH. Time traces of P$^{\text{exo}}$-fluoro foci in four representative cells; the fixation point (red arrows) is shown (**f**). Representative images (**g**) and quantification (**h**) indicate antigenome appearance timing. Data are mean ± s.d. (**h**). **i**–**k**, Infection outcomes in relation to vRNP number and DARPin-P state. Representative timelapse images of infections with a single DARPin-P^{-} (orange arrowheads) or DARPin-P^{+} (purple arrowheads) vRNP (**i**). See also Supplementary Video 4. The graphs display infection success relative to vRNP number (**j**) and DARPin-P state (**k**). **l**,**m**, Infection dynamics of clinical RSV isolates showing infection success frequency (**l**) and its dependence on the vRNP DARPin-P state (**m**). Data are mean ± s.d. (**l**). **n**, Infection outcomes for RSV produced in different cell lines and primary cultures (see also Extended Data Fig. 4a,b,f). Data are mean ± s.d. Infection success was defined by AbG-fluoro labelling (**j**,**k**,**m**). Cumulative incidence graphs show lines and shaded areas for mean ± s.e., respectively (**d**,**e**,**j**,**k**,**m**). Scale bars, 10 µm (**a**,**g**,**i**). Experimental repeats and fluorophores are listed in Supplementary Table 1.

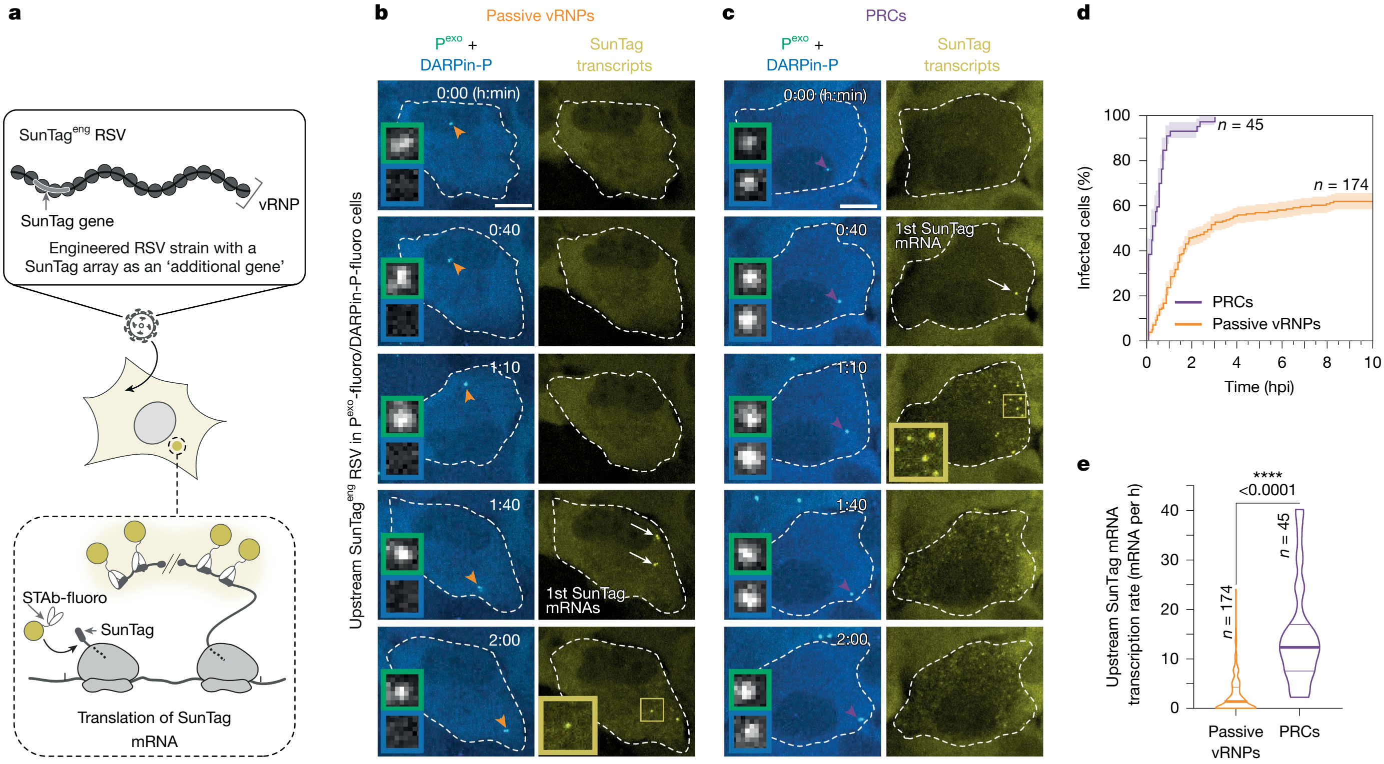

Fig. 4 | PRCs are highly active in transcription. a–**e**, Engineered RSV strain encoding a SunTag peptide array as an additional 'viral gene' (SunTag$^{\text{eng}}$ RSV) allows real-time quantification of the number of (translated) viral mRNAs per infected cell over time, which is a good proxy for early viral transcription rates (see also Extended Data Fig. 7e,f). The SunTag array was inserted between the viral P and M genes (upstream SunTag$^{\text{eng}}$ RSV). P$^{\text{exo}}$-fluoro, DARPin-P-fluoro and SunTag mRNA imaging assays were combined in a single experiment. Schematic of the SunTag imaging assay (**a**). Representative images of timelapse videos of cells infected by either a passive vRNP (**b**) or PRC (**c**). The left panels show a merge of P$^{\text{exo}}$-fluoro and DARPin-P-fluoro signals, whereas the right panels show SunTag mRNA (STAb-fluoro foci) images. On the merged images, the orange and purple arrowheads identify passive vRNPs and PRCs, respectively, and the green and blue insets show P$^{\text{exo}}$ and DARPin-P signals, respectively, for the indicated vRNPs. Note that the high levels of translated viral SunTag mRNAs that accumulate in PRC infections leads to dimming of SunTag foci over time (as observed from 1:40 onwards in panel **c**) due to depletion of free cellular STAb-fluoro as a result of cytoplasmic accumulation of mature SunTag peptides, which sequester free STAb-fluoro, as previously reported[53,54]. See also Supplementary Video 5. Cumulative incidence graph depicts the start of viral transcription for infections by passive vRNPs and PRCs (**d**). The lines are means and the shaded areas are s.e. The viral transcription rate was calculated and plotted as violin plots with the median and quartiles shown (horizontal lines; **e**). A two-tailed unpaired Student's *t*-test was used for statistical analysis. Scale bars, 10 μm (**b**,**c**). Experimental repeats and fluorophores are listed in Supplementary Table 1.

in host cells, resulting in bright fluorescent foci representing single translating mRNAs (Fig. 4a). The SunTag gene was inserted into the viral genome either between the viral P and M genes (upstream SunTag$^{\text{eng}}$) or between the F and M2 genes (downstream SunTag$^{\text{eng}}$; Extended Data Fig. 7a). Introduction of the SunTag gene had minimal effect on viral growth kinetics, with comparable fitness with that of the previously described RSV–mCherry engineered strain[17] (Extended Data Fig. 7b,c). Fluorescent SunTag mRNA foci appeared after infection with the SunTag$^{\text{eng}}$ RSV strain. These represented translating SunTag mRNAs, as signals rapidly disappeared upon treatment with the translation inhibitor puromycin (Extended Data Fig. 7d). The number of foci observed in live cells correlated very well with the number of SunTag mRNAs detected by smFISH in the same fixed cells ($R^2 = 0.97$; Extended Data Fig. 7e,f), demonstrating that the number of translated SunTag mRNAs measured in live cells accurately reflects the number of total viral SunTag mRNAs, and can thus be used to determine viral transcription rates. Analysis of the number of SunTag mRNAs over time revealed that the rate of mRNA transcription was substantially higher in the SunTag$^{\text{eng}}$ strain with the upstream insert than the SunTag$^{\text{eng}}$ strain with the downstream insert, consistent with transcription rates being higher for genes at the 3′ end of the viral genome[30] (Extended Data Fig. 7g). Together, these results show that the SunTag mRNA imaging method is a reliable and robust approach to quantify viral transcription dynamics in living cells.

To interrogate viral transcription dynamics of heterogeneous vRNPs, we combined SunTag mRNA imaging with the P$^{\text{exo}}$-fluoro and DARPin-P-fluoro imaging systems. The SunTag peptide used in the P$^{\text{exo}}$-fluoro system to label P was replaced by an orthogonal tagging system, the ALFA-Tag and the nanobody-ALFA-fluoro[31], to enable combined P$^{\text{exo}}$-fluoro and SunTag transcriptional imaging. Following three-colour timelapse imaging, transcriptional activity was assessed for both PRCs and passive vRNPs (Fig. 4b,c, Extended Data Fig. 7h and Supplementary Video 5). All infections with PRCs showed rapid viral transcriptional activation upon vRNP entry, with 100% of infection events showing transcription by 3 hpi, for both the upstream and the downstream SunTag genes, compared with only 64% and 42% for passive vRNPs, respectively (Fig. 4d and Extended Data Fig. 7i). Even for the passive vRNP infections that did show transcription, transcriptional dynamics were severely delayed, with only 28% of the upstream and 11% of the downstream infections showing transcripts at 1 hpi, whereas 94% of upstream and 50% of downstream PRC infections showed transcripts at that time point (Fig. 4d and Extended Data Fig. 7i). PRC-containing infections also had substantially higher rates of transcription (5.4× and 15.1× higher for the upstream and downstream SunTag$^{\text{eng}}$ RSV strains, respectively) than their passive vRNP-containing counterparts (Fig. 4e and Extended Data Fig. 7j). Collectively, these findings demonstrate that PRCs have much higher rates of transcription, probably explaining their high infection success.

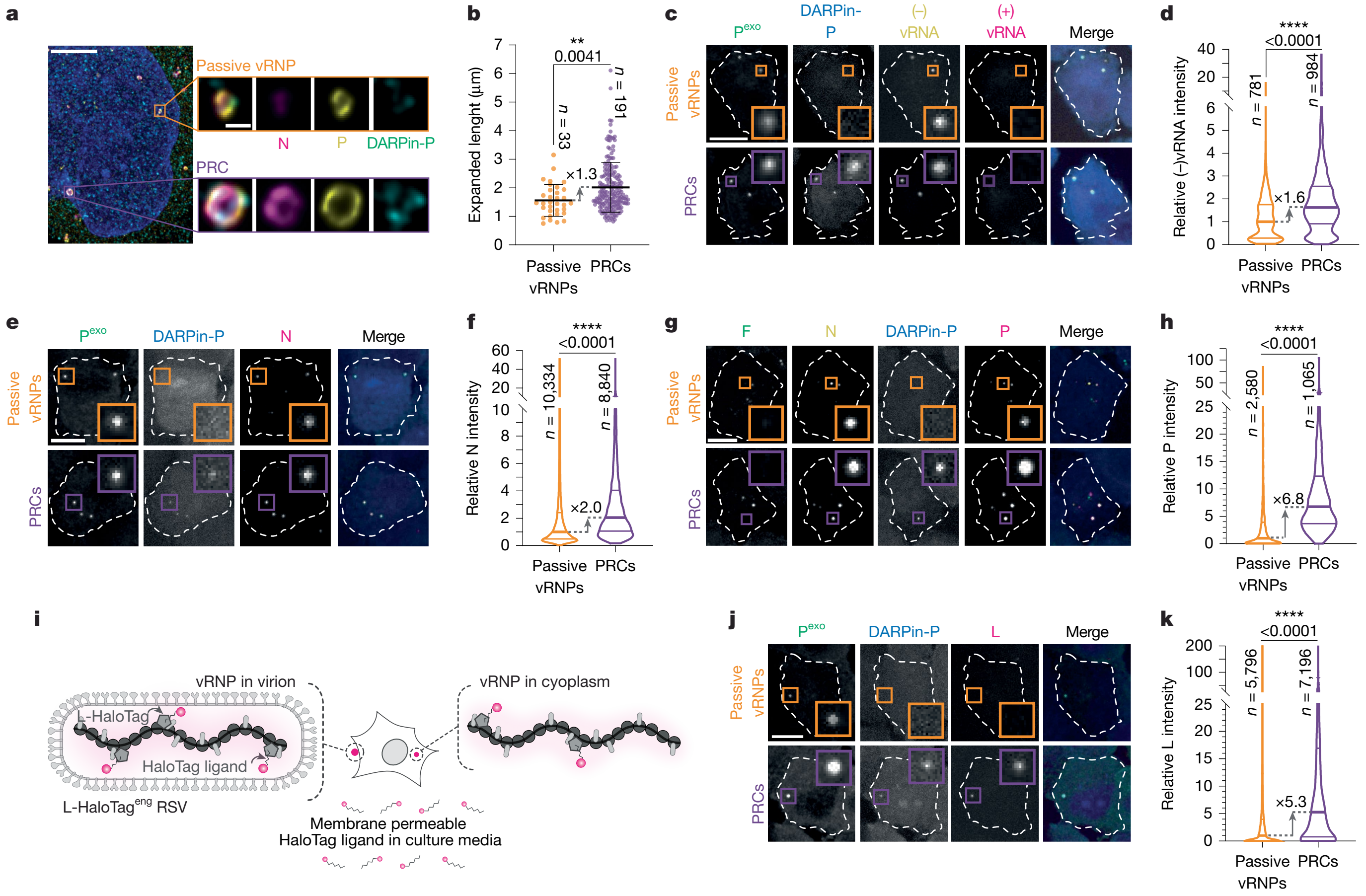

Fig. 5 | PRCs have higher quantities of associated viral proteins. Incoming passive vRNPs and PRCs were assessed at 4 h following viral inoculum addition. The translation inhibitor emetine was added to cells together with virus addition to prevent progression of infection. **a**,**b**, Super-resolution imaging of RSV vRNPs by ExM (approximately ×4.5). Representative images (**a**) and quantification (**b**) highlight size differences between passive vRNPs and PRCs. **c**,**d**, Genome ((−)vRNA) and antigenome ((+)vRNA) presence in vRNPs was evaluated. Representative images of smFISH staining carried out on the P^{exo}-fluoro/DARPin-P-fluoro cell line (**c**) and quantification of the (−)vRNA intensity for passive vRNPs and PRCs (**d**) are shown. **e**–**k**, RSV vRNP-constituent protein levels were assessed in passive vRNPs and PRCs. Representative images (**e**) and quantification (**f**) of N levels. Representative images (**g**) and quantification (**h**) of P levels. A schematic highlighting the L-HaloTag^{eng} RSV strain, which enables real-time visualization of viral polymerase (L) levels in the presence of fluorescently tagged, cell membrane-permeable HaloTag ligands (**i**) is shown. This strain allows visualization of viral polymerase levels both in the virion and on vRNPs in infected cells. Representative images (**j**) and quantification (**k**) of L levels. The violin plots show median and quartiles (horizontal lines; **d**,**f**,**h**,**k**). A two-tailed unpaired Student's *t*-test was used for statistical analysis (**b**,**d**,**f**,**k**). Scale bars, 10 µm (**c**,**e**,**g**,**j**), and 10 µm and 1 µm (zoomed out image and zoomed in image, respectively, in panel **a**). Note that these samples were subjected to approximately 4.5-fold expansion, as such 1 µm in the image corresponds to approximately 222 nm before expansion. Experimental repeats and fluorophores are listed in Supplementary Table 1.

PRCs have high levels of vRNP proteins

As PRCs and passive vRNPs showed major functional differences, we asked whether they also had distinct morphologies. We used super-resolution expansion microscopy (ExM) to image vRNPs at an approximate resolution of 60 nm (ref. 32). Although we found that vRNP morphology was highly heterogeneous for both types of vRNPs, the overall size of PRCs (approximately 448 nm in diameter) was larger than that of passive vRNPs (approximately 346 nm in diameter; note that values are adjusted for the approximately 4.5-fold expansion factor; Fig. 5a,b and Extended Data Fig. 8a,b). The size differences between vRNPs could reflect variations in vRNA or protein composition. To investigate this, we first assessed viral genome and antigenome content of PRCs and passive vRNPs by smFISH. This showed that both types of vRNPs contained mostly genomes, with a low frequency of vRNP foci containing both a genome and an antigenome (Fig. 5c and Extended Data Fig. 8c). The genome smFISH staining for PRCs was 1.6-fold higher in intensity than their passive vRNP counterparts (Fig. 5d), suggesting that either a subset of PRC foci contains two or more genomes, or that vRNAs of PRCs are more accessible for smFISH probes. In either case, the difference in genome content is substantially smaller than the difference in transcriptional activity (more than tenfold), demonstrating that individual PRC genomes have much higher transcriptional activity than genomes of passive vRNPs.

To further explore compositional differences between PRCs and passive vRNPs that could result in their functional differences, we assessed the levels of the vRNP-associated proteins N, P and L. As vRNAs are thought to be fully encapsidated by N proteins[4,5,33], we would expect N levels to mirror the vRNA content. Using antibody staining, we found that PRCs were associated with twofold higher N levels than passive vRNPs (Fig. 5e,f), which is in a similar range as the observed increase in vRNA labelling, suggesting that PRCs have similar or slightly higher levels of N per vRNA compared with passive vRNPs. The slightly higher N levels could reflect association of additional free N, referred to as N^0, with PRCs, as is the case for VFs[34].

We next examined P and L levels on different vRNPs. Antibody staining revealed that PRCs contained 6.8-fold higher P levels than passive vRNPs (Fig. 5g,h and Extended Data Fig. 8d). To assess L protein (viral polymerase) levels on incoming RSV vRNPs, we generated an engineered RSV strain carrying a HaloTag in the coding sequence of the

L gene, which can be labelled by membrane-permeable fluorescent dyes[35] (L-HaloTag^{eng} RSV; Fig. 5i and Extended Data Fig. 8e). L levels were 5.3-fold higher on PRCs than passive vRNPs (Fig. 5j,k and Extended Data Fig. 8f). The levels of P and L proteins associated with PRCs (5–7-fold) are substantially higher than the difference in the number of genomes (1.6-fold), indicating that PRCs have a higher viral protein occupancy per genome. The higher levels of vRNP-associated proteins on PRCs provide a plausible explanation for their high transcriptional activity and more rapid replication dynamics. Moreover, higher P levels on PRCs also could provide (part of) the explanation for why PRCs were selectively labelled by DARPin-P, as discussed later.

PRCs represent condensate seeds

We considered two, non-mutually exclusive explanations for the substantially higher levels of P and L on PRCs; first, it is possible that PRCs originate from virions with higher viral protein levels. Second, PRCs may show stronger interactions between viral proteins, retaining binding of viral proteins present in virions more effectively upon cytoplasmic entry. To assess these two possibilities, we measured L levels both in virions and subsequently on single vRNPs after cytoplasmic entry using the L-HaloTag^{eng} strain (Figs. 5i and 6a). We found that L intensity was not just higher on PRCs after cell entry but also in the virions from which the PRCs originated (Figs. 5k and 6b), demonstrating that vRNP compositional heterogeneity originates, at least in part, from infecting virions. In addition, when L intensity on vRNPs was followed as virions fused with host cells and released their vRNPs into the cytoplasm, we found that L rapidly dissociated from passive vRNPs, while remaining bound to PRCs (Fig. 6a,c). To determine whether P shows a similar higher off-rate from passive vRNPs than PRCs after cell entry, we engineered an RSV strain in which the endogenous P protein was fluorescently tagged (referred to as P^{endo}; see Methods; Fig. 6d). The P^{endo} strain demonstrated growth kinetics comparable with WT RSV (Extended Data Fig. 8g), and allowed robust detection of endogenous P levels, as 98 ± 1% of virions contained detectable levels of the tagged P protein (Extended Data Fig. 8h,i). Upon cell entry, the levels of endogenous P on incoming PRC vRNPs was 3.5-fold higher than on passive vRNPs, consistent with our antibody staining (Figs. 5g,h and 6e,f). P protein rapidly dissociated from passive vRNPs, as was observed for L, while remaining tightly associated with PRCs, suggesting that the P affinity for vRNPs also depends on their vRNP state (Fig. 6e,g). We next explored association kinetics of P towards PRCs and passive vRNPs. We examined binding kinetics of P^{exo}-fluoro to vRNPs immediately after viral entry into the cytoplasm (Fig. 6h). We observed that PRCs not only brought in more endogenous P (assessed via P^{endo}), but also attracted more P that was present in the cytoplasm than passive vRNPs (assessed via P^{exo}-fluoro binding; Fig. 6i,j). RSV infection in a cell line expressing fluorescently tagged N (N^{exo}-fluoro) allowed visualization of free N (N^0) association with vRNPs in early infection before VF formation and replication (Extended Data Fig. 8j). Although total N levels were comparable on PRCs and passive vRNPs, we found that association kinetics of N^0 was higher for PRCs (Extended Data Fig. 8k,l). In conclusion, PRCs are more efficient at retaining and recruiting viral proteins (that is, they are 'sticky' for viral proteins), probably explaining their potent ability to nucleate biomolecular condensates (that is, VFs), as condensates are formed through multimeric protein–protein interactions[36].

The substantially higher levels of both endogenous P and P^{exo}-fluoro on PRCs than passive vRNPs probably explains why PRCs are selectively labelled (that is, above the detection threshold) by DARPin-P, as DARPin-P binds directly to P. However, it is possible that, in addition, DARPin-P also preferentially binds to PRCs because of differences in P phosphorylation, structure or epitope accessibility. As we found that DARPin-P labels VFs very strongly (see Extended Data Fig. 5u), we hypothesized that DARPin-P may preferentially label P inside condensates. Consistent with this, we observed that, DARPin-P staining intensity increased substantially more rapidly than overall P levels as PRCs grew into VFs (Extended Data Fig. 8m), indicating that DARPin-P labelling efficiency does not exclusively reflect overall P levels. Indeed, DAPRin-P showed a preferential labelling of P inside condensates, both for VFs and pseudo-VFs formed upon overexpression of N and P (Extended Data Fig. 8n). We also assessed the role of P phosphorylation in DARPin-P binding selectivity. P is also known to be highly phosphorylated, with three potential phosphorylation sites on P overlapping with the DARPin-P-binding epitope of P. However, DARPin-P binding to either a phospho-mimetic or a non-phosphorylatable variant of P was similar (Extended Data Fig. 8o,p), suggesting that phosphorylation of P does not directly alter binding of DARPin-P. Consistently, mass spectrometry and gel shift assays did not reveal major differences in the phosphorylation state of P that was bound by DARPin-P compared with total cellular P (Extended Data Fig. 8q,r and Supplementary Table 2), although small differences in phosphorylation may have gone undetected due to the technical noise of these assays. Together, these results show that DARPin-P specifically labels PRCs both because of higher total levels of P on PRCs and also because P in condensates may be more readily bound by DARPin-P. Future high-resolution cryo-electron tomography studies will hopefully resolve the precise in vivo structure of P associated with both PRCs and passive vRNPs.

Building on the selective viral protein association with PRCs, we next asked whether PRCs also exhibit enhanced interactions with other vRNPs. First, we measured the separation dynamics of vRNPs originating from a single virion upon cytoplasmic entry, and observed that on average PRCs took longer to split than passive vRNPs (45 min versus 20 min; Fig. 6k). This result indicates that PRCs are not only more effective at recruiting and retaining viral proteins but also show increased affinity towards other vRNPs. Possibly, the affinity to other vRNPs is so high that a subset of incoming vRNPs remain associated upon cell entry, providing an explanation for why PRCs have a slightly higher average viral genomic RNA content than passive vRNPs (Fig. 5d). The increased affinity of PRCs for other vRNPs was also observed during later infection, where 100% of PRCs underwent vRNP fusion, with a median time of 5.5 hpi (Fig. 6l). By contrast, only 16% of passive vRNPs showed vRNP fusion, and the fusion events that did occur, happened substantially later in infection (Fig. 6l). These observations show that PRCs recruit not only viral proteins but also other vRNPs. It is likely that most PRCs are not yet 'sticky' enough to maintain vRNP association upon cell entry due to insufficient viral proteins, explaining initial vRNP splitting, but as PRCs grow due to new viral protein synthesis and association, their 'stickiness' increases with the increasing size of the protein–protein interaction network to the point that vRNPs start to fuse (Extended Data Fig. 9a). Consistent with PRCs sharing biochemical properties with VFs, PRCs were also highly sensitive to cyclopamine, a drug known to interfere with the liquid-like properties of VFs[37,38] (Extended Data Fig. 9b–e). As many of the features that define mature VFs are already present in incoming PRCs, PRCs resemble biomolecular condensate 'seeds' that are primed to nucleate VFs.

If PRCs indeed seed VFs, we would predict that PRC formation would always precede VF formation. Our earlier results showed that a subset of incoming passive vRNPs eventually undergo viral replication (Fig. 3k, DARPin-P$^-$ vRNPs), and we wondered whether vRNPs in these infections transitioned from passive vRNPs to PRCs before undergoing VF formation and subsequent replication. Indeed, we observed that in all cases in which incoming vRNPs started as passive vRNPs but successfully formed VFs, one or more passive vRNP became PRCs before VF formation and viral replication ensued (Fig. 6m–o, Extended Data Fig. 9f,g and Supplementary Video 6). When we examined infections for which passive vRNPs eventually acquired the PRC state, they showed higher transcription rates even during very early infection than passive vRNPs that remained passive (Extended Data Fig. 9h–k). Moreover, these passive vRNPs that went on to become PRCs also demonstrated increased recruitment and retention of viral proteins (Extended Data

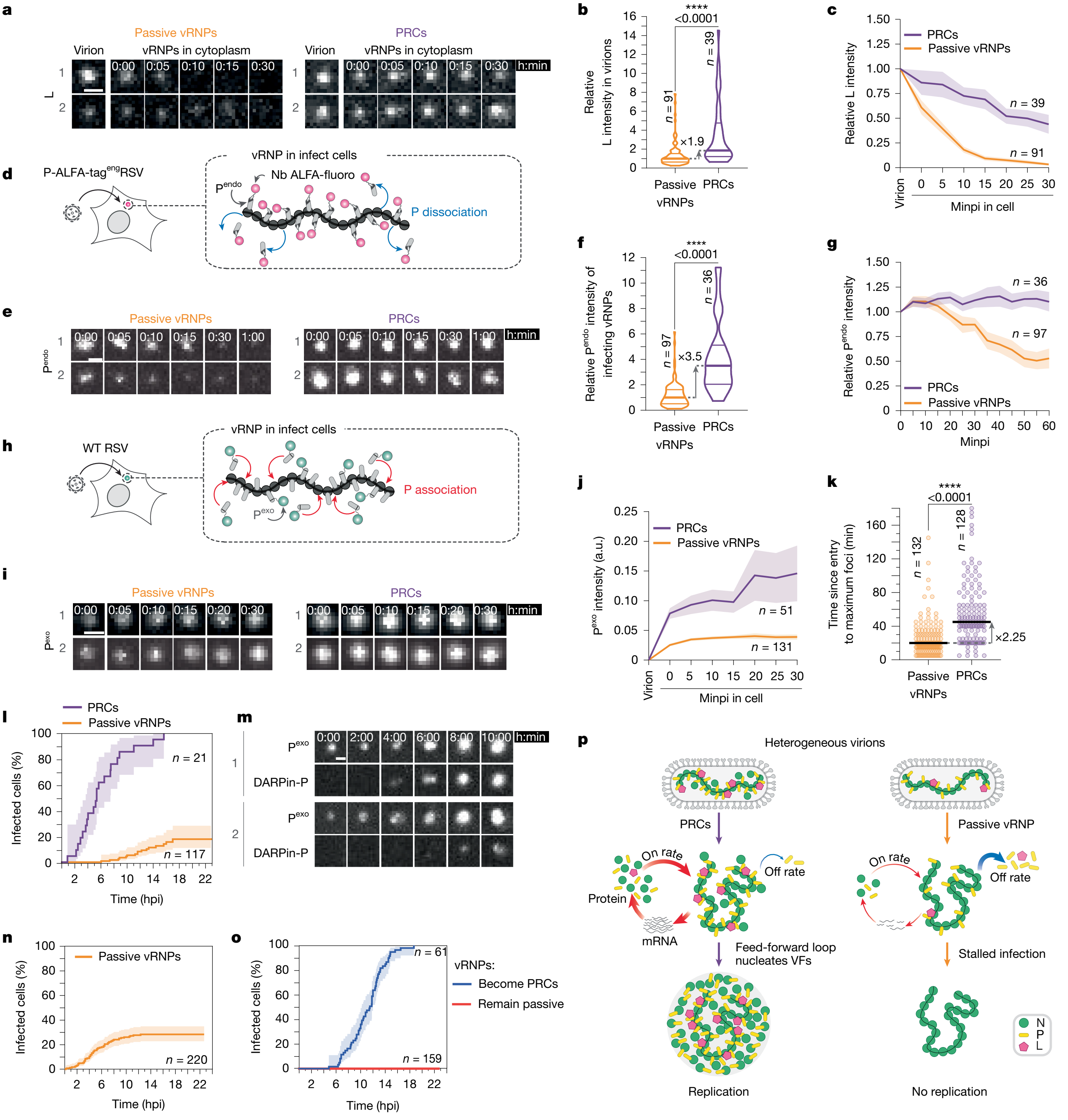

Fig. 6 | PRCs are biomolecular condensate seeds. a–c, Visualization of L protein levels in virions and on vRNPs after host cell. Representative image series showing L protein levels in virions before entry and on vRNPs after entry for passive vRNPs and PRCs (**a**). Quantification of L levels in virions (**b**) and on vRNPs over time (**c**). Minpi, minutes post infection. **d–g**, Visualization of endogenous P (P^{endo}) on vRNPs using the P-ALFA-Tag^{eng} RSV strain. A schematic of P^{endo} visualization in cells expressing Nb-ALFA-fluoro (**d**); a representative image series of the vRNP P^{endo} signal over time on passive vRNPs and PRCs (**e**); quantification of P^{endo} levels on the infecting vRNP (**f**) and the relative P^{endo} levels on vRNPs over a 1-h period post-entry (**g**) are shown. **h–j**, Viral protein association kinetics with passive vRNPs and PRCs, assessed using the P^{exo}-fluoro/DARPin-P-fluoro system. Infections using the P-ALFA-Tag^{eng} RSV strain in cells additionally expressing Nb-ALFA-fluoro, allowed vRNP identification independent of the P^{exo}-fluoro signal. A schematic showing visualization of exogenous viral P protein association with cytoplasmic vRNPs (**h**); a representative image series of the vRNP P^{exo}-fluoro signal over time (**i**); and quantification of the P^{exo}-fluoro levels on vRNPs over 30 min (**j**). **k**,**l**, Quantification of vRNP separation kinetics (**k**) and vRNP fusion kinetics (**l**) as cumulative incidence graphs. Data are median (**k**). **m–o**, Analysis of passive vRNPs transitioning to PRCs. A representative image series illustrating such transitions (**m**; see also Supplementary Video 6), cumulative incidence graphs showing the kinetics of passive vRNPs becoming PRCs (**n**) and their infection success rate (**o**) are shown. **p**, Schematic showing the mechanism by which a subset of infecting vRNPs seed VFs. For simplicity, single vRNP virions are shown. The lines are means and the shaded regions are s.e. (**c**,**g**,**j**,**l**,**n**,**o**). A two-tailed unpaired Student's *t*-test was used for statistical analysis (**b**,**f**,**k**). Scale bars, 1 µm (**a**,**e**,**i**,**m**). Experimental repeats and fluorophores are listed in Supplementary Table 1.

Fig. 9l). These results suggest that the PRC state may not be a binary phenotype, but rather a continuum that reports on the ability of vRNPs to nucleate VFs and is dependent on the levels of viral proteins associated with vRNPs. These results suggest that increasing viral protein association with passive vRNPs may allow passive vRNPs to transition to PRCs. Indeed, we found that co-expression of both N and P in host cells stimulated passive vRNPs to become PRCs and nucleate VFs (Extended Data Fig. 9m), consistent with the model that passive vRNPs fail to progress in infection due to insufficient levels of associated viral N and P protein.

Discussion

In this study, we have developed technologies to visualize RSV infection with single vRNP resolution in living cells. Using these technologies, we have tracked viral infection from vRNP entry through viral transcription, VF formation and viral replication. We identified PRCs as crucial structures that nucleate VFs and are thus essential for viral genome replication. Our results identify two key features of PRCs that make them potent nucleators of VFs. First, PRCs are transcriptionally highly active, driving rapid accumulation of newly synthesized viral proteins needed for vRNP growth into VFs. Second, PRCs have high affinities for viral proteins, resulting in high stability at low viral protein concentrations and efficient recruitment of newly synthesized viral proteins, features essential to nucleate biomolecular condensates at low viral protein concentrations. Together, these features result in a feed-forward loop that drives rapid growth of PRCs into VFs (Fig. 6p). We found that PRCs are pre-formed and packaged into virions, which allows rapid kickstarting of viral infection once vRNPs enter host cells. As only a small subset of virions contain PRCs, our results also identified virion heterogeneity as a major cause of cell-to-cell variation in RSV infection.

RSV virions are compositionally diverse

We observed virion diversity with respect to viral protein composition and the number and type of vRNPs that are packaged. We found that the number of vRNPs per virion is not a major determinant of infection success, but rather it is the vRNP state that determines infection success. vRNPs originating from the same virion are generally in the same vRNP state. Therefore, a subset of RSV virions, those containing one or more PRCs, are highly infectious and most likely the main drivers establishing a successful (primary) infection. Why certain virions contain mostly PRCs while others contain mostly passive vRNPs remains an interesting open question. One possibility is that virion composition is determined at the level of virus-producing cells. In line with this, we found that virus produced in different cell types showed different frequencies of virions containing PRCs. Although virion heterogeneity is an important determinant of infection success, other features, including host cell heterogeneity or stochastic events during (early) infection, may also contribute to cell-to-cell variations in infection progression.

Transcription–replication coordination

The RSV genome acts as a template for both viral transcription and replication. Viral transcription should precede viral replication, because newly synthesized N protein is required for encapsidation of new genomes and antigenomes produced during replication. However, if and how transcription and replication are temporally coordinated remained unknown. Here we showed that even though transcription occurs in VFs during late-stage infection, VFs are not required for viral transcription, as viral transcription occurs on vRNPs that are freely diffusing in the cytoplasm, before the formation of VFs. By contrast, our results show that replication occurs exclusively in VFs, and as such, VFs are essential for viral replication. As VF formation requires synthesis of new viral proteins and thus requires viral transcription, VF formation temporally coordinates viral transcription and replication to ensure correct vRNA encapsidation.

Biomolecular condensate biogenesis

VFs have been demonstrated to concentrate the RSV vRNP constituent proteins N, P, L and M2-1 (refs. 1,9,39–41), as well as viral genomes and transcripts[1,42–44], and constitute key sites of viral transcription and replication in late-stage viral infection. VF formation is probably driven by low-affinity multimeric protein–protein interactions mediated by the intrinsically disordered regions of N and P[45–48]. Indeed, overexpression of N and P alone is sufficient for formation of viral condensates, even in uninfected cells[10]. Despite our understanding of the composition and physiochemical properties of VFs, the mechanism of their biogenesis during natural infection, when N and P levels are initially very low, was lacking. Here we showed that VFs are typically nucleated by individual vRNPs, rather than being formed de novo in the cytoplasm. PRCs may act as nucleation seeds by providing a scaffold for recruitment of viral and non-viral proteins, thereby enabling VF formation during early infection, when viral protein concentrations are probably below the critical threshold for de novo nucleation of biomolecular condensates. PRCs are potent nucleators of VFs, as they are associated with high levels of viral N, P and L protein. High levels of these proteins probably result in higher viral transcription and protein synthesis rates, which results in recruitment of even more viral proteins to these vRNPs. In addition, higher levels of N and P on PRCs probably also create a stable multimeric protein interaction network surrounding vRNPs that prevents N, P and L molecules from dissociating from PRCs upon host cell entry, and creates increased numbers of binding sites to recruit newly synthesized viral N, P and L proteins, further enhancing their growth into VFs. Higher transcription rates combined with higher rates of viral protein recruitment create an effective positive-feedback loop that drives PRC growth into VFs. Once viral protein interaction networks in PRCs have grown above a critical threshold, PRCs can either fuse with other vRNPs, if present in infected cells, or themselves form mature VFs. The feedback loop that drives PRC growth can also result in stalled infections when vRNPs associated with low levels of viral proteins enter the host cell. Not only do these vRNPs produce few viral proteins due to low transcription rates but viral proteins also dissociate rapidly from these vRNPs. Consistent with this, cellular expression of both N and P allows passive PRCs to transition to PRCs, probably through rapid binding of N and P to passive vRNPs, thus generating a more robust protein–protein network and allowing passive vRNPs to transition to a PRC state. In addition to N, P and L, the RSV M2-1 protein also localizes to VFs, where it functions in viral transcription by engaging P and viral mRNA[49–52]. It will be interesting to determine whether M2-1 also associates with incoming vRNPs and whether differences in M2-1 association impact transcriptional output. Many different viruses utilize biomolecular condensates for their transcription and/or replication and will thus face similar physiochemical challenges in condensate formation at low viral protein levels. It will therefore be interesting to determine whether seeding of viral condensates by incoming vRNPs is a universal mechanism to overcome these challenges. More broadly, our study on RSV VF nucleation may provide a paradigm for condensate nucleation beyond virology.

Online content

Any methods, additional references, Nature Portfolio reporting summaries, source data, extended data, supplementary information, acknowledgements, peer review information; details of author contributions and competing interests; and statements of data and code availability are available at https://doi.org/10.1038/s41586-025-10071-5.

1. Rincheval, V. et al. Functional organization of cytoplasmic inclusion bodies in cells infected by respiratory syncytial virus. *Nat. Commun.* **8**, 563 (2017).
2. Dolnik, O., Gerresheim, G. K. & Biedenkopf, N. New perspectives on the biogenesis of viral inclusion bodies in negative-sense RNA virus infections. *Cells* **10**, 1460 (2021).
3. Mitrea, D. M., Mittasch, M., Gomes, B. F., Klein, I. A. & Murcko, M. A. Modulating biomolecular condensates: a novel approach to drug discovery. *Nat. Rev. Drug Discov.* **21**, 841–862 (2022).
4. Bakker, S. E. et al. The respiratory syncytial virus nucleoprotein–RNA complex forms a left-handed helical nucleocapsid. *J. Gen. Virol.* **94**, 1734–1738 (2013).
5. Tawar, R. G. et al. Crystal structure of a nucleocapsid-like nucleoprotein-RNA complex of respiratory syncytial virus. *Science* **326**, 1279–1283 (2009).
6. Šantak, M. & Matić, Z. The role of nucleoprotein in immunity to human negative-stranded RNA viruses — not just another brick in the viral nucleocapsid. *Viruses* **14**, 521 (2022).
7. Yu, Q., Hardy, R. W. & Wertz, G. W. Functional cDNA clones of the human respiratory syncytial (RS) virus N, P, and L proteins support replication of RS virus genomic RNA analogs and define minimal *trans*-acting requirements for RNA replication. *J. Virol.* **69**, 2412–2419 (1995).
8. Collins, P. L. et al. Production of infectious human respiratory syncytial virus from cloned cDNA confirms an essential role for the transcription elongation factor from the 5′ proximal open reading frame of the M2 mRNA in gene expression and provides a capability for vaccine development. *Proc. Natl Acad. Sci. USA* **92**, 11563–11567 (1995).
9. García, J., García-Barreno, B., Vivo, A. & Melero, J. A. Cytoplasmic inclusions of respiratory syncytial virus-infected cells: formation of inclusion bodies in transfected cells that coexpress the nucleoprotein, the phosphoprotein, and the 22K protein. *Virology* **195**, 243–247 (1993).
10. Galloux, M. et al. Minimal elements required for the formation of respiratory syncytial virus cytoplasmic inclusion bodies in vivo and in vitro. *mBio* https://doi.org/10.1128/mbio01202-01220 (2020).
11. Alberti, S. et al. Current practices in the study of biomolecular condensates: a community comment. *Nat. Commun.* **16**, 7730 (2025).
12. Banani, S. F., Lee, H. O., Hyman, A. A. & Rosen, M. K. Biomolecular condensates: organizers of cellular biochemistry. *Nat. Rev. Mol. Cell Biol.* **18**, 285–298 (2017).
13. Jeon, S. et al. Emerging regulatory mechanisms and functions of biomolecular condensates: implications for therapeutic targets. *Signal Trans. Target. Ther.* **10**, 4 (2025).
14. Alberti, S. Phase separation in biology. *Curr. Biol.* **27**, R1097–R1102 (2017).
15. Rabouw, H. H. et al. Mapping the complete influenza A virus infection cycle through single vRNP imaging. Preprint at *bioRxiv* https://doi.org/10.1101/2025.01.20.633851 (2025).
16. Boersma, S. et al. Translation and replication dynamics of single RNA viruses. *Cell* **183**, 1930–1945.e23 (2020).
17. Rameix-Welti, M.-A. et al. Visualizing the replication of respiratory syncytial virus in cells and in living mice. *Nat. Commun.* **5**, 5104 (2014).
18. Plückthun, A. Designed ankyrin repeat proteins (DARPins): binding proteins for research, diagnostics, and therapy. *Annu. Rev. Pharmacol. Toxicol.* **55**, 489–511 (2015).
19. Galloux, M. et al. Characterization of a viral phosphoprotein binding site on the surface of the respiratory syncytial nucleoprotein. *J. Virol.* **86**, 8375–8387 (2012).
20. Tanenbaum, M. E., Gilbert, L. A., Qi, L. S., Weissman, J. S. & Vale, R. D. A protein-tagging system for signal amplification in gene expression and fluorescence imaging. *Cell* **159**, 635–646 (2014).
21. Wörn, A. et al. Correlation between in vitro stability and in vivo performance of anti-GCN4 intrabodies as cytoplasmic inhibitors. *J. Biol. Chem.* **275**, 2795–2803 (2000).
22. Kiss, G. et al. Structural analysis of respiratory syncytial virus reveals the position of M2-1 between the matrix protein and the ribonucleoprotein complex. *J. Virol.* **88**, 7602–7617 (2014).
23. Loney, C., Mottet-Osman, G., Roux, L. & Bhella, D. Paramyxovirus ultrastructure and genome packaging: cryo-electron tomography of sendai virus. *J. Virol.* **83**, 8191–8197 (2009).
24. Liljeroos, L., Krzyzaniak, M. A., Helenius, A. & Butcher, S. J. Architecture of respiratory syncytial virus revealed by electron cryotomography. *Proc. Natl Acad. Sci. USA* **110**, 11133–11138 (2013).
25. Coates, M. et al. Preclinical characterization of PC786, an inhaled small-molecule respiratory syncytial virus L protein polymerase inhibitor. *Antimicrob. Agents and Chemother.* https://doi.org/10.1128/aac00737-00717 (2017).
26. Jobe, F. et al. Viral PIC-pocketing: RSV sequestration of translational preinitiation complexes into bi-phasic biomolecular condensates. *J. Virol.* **98**, e00153-00124 (2024).
27. Zhang, Q. et al. PABP-driven secondary condensed phase within RSV inclusion bodies activates viral mRNAs for ribosomal recruitment. *Virol. Sinica* **39**, 235–250 (2024).
28. Sun, Y. et al. A specific sequence in the genome of respiratory syncytial virus regulates the generation of copy-back defective viral genomes. *PLoS Pathog.* **15**, e1007707 (2019).
29. Felt, S. A. et al. Detection of respiratory syncytial virus defective genomes in nasal secretions is associated with distinct clinical outcomes. *Nat. Microbiol.* **6**, 672–681 (2021).
30. Donovan-Banfield, I. A. et al. Direct RNA sequencing of respiratory syncytial virus infected human cells generates a detailed overview of RSV polycistronic mRNA and transcript abundance. *PLoS ONE* **17**, e0276697 (2022).
31. Götzke, H. et al. The ALFA-tag is a highly versatile tool for nanobody-based bioscience applications. *Nat. Commun.* **10**, 4403 (2019).
32. Chen, F., Tillberg, P. W. & Boyden, E. S. Expansion microscopy. *Science* **347**, 543–548 (2015).
33. Gonnin, L. et al. Structural landscape of the respiratory syncytial virus nucleocapsids. *Nat. Commun.* **14**, 5732 (2023).
34. Basse, V. et al. Regulation of respiratory syncytial virus nucleoprotein oligomerization by phosphorylation. *J. Biol. Chem.* **301**, 108256 (2025).
35. Los, G. V. et al. HaloTag: a novel protein labeling technology for cell imaging and protein analysis. *ACS Chem. Biol.* **3**, 373–382 (2008).
36. Shin, Y. & Brangwynne, C. P. Liquid phase condensation in cell physiology and disease. *Science* **357**, eaaf4382 (2017).
37. Risso-Ballester, J. et al. A condensate-hardening drug blocks RSV replication in vivo. *Nature* **595**, 596–599 (2021).
38. Diot, C. et al. Hardening of respiratory syncytial virus inclusion bodies by cyclopamine proceeds through perturbation of the interactions of the M2-1 protein with RNA and the P protein. *Int. J. Mol. Sci.* **24**, 13862 (2023).
39. Norrby, E., Marusyk, H. & Örvell, C. Morphogenesis of respiratory syncytial virus in a green monkey kidney cell line (Vero). *J. Virol.* **6**, 237–242 (1970).
40. García-Barreno, B., Delgado, T. & Melero, J. A. Identification of protein regions involved in the interaction of human respiratory syncytial virus phosphoprotein and nucleoprotein: significance for nucleocapsid assembly and formation of cytoplasmic inclusions. *J. Virol.* **70**, 801–808 (1996).
41. Carromeu, C., Simabuco, F. M., Tamura, R. E., Farinha Arcieri, L. E. & Ventura, A. Intracellular localization of human respiratory syncytial virus L protein. *Arch. Virol.* **152**, 2259–2263 (2007).
42. Lindquist, M. E., Lifland, A. W., Utley, T. J., Santangelo, P. J. & Crowe, J. E. Jr. Respiratory syncytial virus induces host RNA stress granules to facilitate viral replication. *J. Virol.* **84**, 12274–12284 (2010).
43. Santangelo, P. J. & Bao, G. Dynamics of filamentous viral RNPs prior to egress. *Nucleic Acids Res.* **35**, 3602–3611 (2007).
44. Lifland, A. W. et al. Human respiratory syncytial virus nucleoprotein and inclusion bodies antagonize the innate immune response mediated by MDA5 and MAVS. *J. Virol.* **86**, 8245–8258 (2012).
45. Cardone, C. et al. A structural and dynamic analysis of the partially disordered polymerase-binding domain in RSV phosphoprotein. *Biomolecules* **11**, 1225 (2021).
46. Simabuco, F. M. et al. Structural analysis of human respiratory syncytial virus P protein: identification of intrinsically disordered domains. *Braz. J. Microbiol.* **42**, 340–345 (2011).
47. Brocca, S., Grandori, R., Longhi, S. & Uversky, V. Liquid–liquid phase separation by intrinsically disordered protein regions of viruses: roles in viral life cycle and control of virus–host interactions. *Int. J. Mol. Sci.* **21**, 9045 (2020).
48. Su, J. M., Wilson, M. Z., Samuel, C. E. & Ma, D. Formation and function of liquid-like viral factories in negative-sense single-stranded RNA virus infections. *Viruses* **13**, 126 (2021).
49. Bouillier, C. et al. The interactome analysis of the respiratory syncytial virus protein M2-1 suggests a new role in viral mRNA metabolism post-transcription. *Sci. Rep.* **9**, 15258 (2019).
50. Braun, M. R. et al. Respiratory syncytial virus M2-1 protein associates non-specifically with viral messenger RNA and with specific cellular messenger RNA transcripts. *PLoS Pathog.* **17**, e1009589 (2021).
51. Tanner, S. J. et al. Crystal structure of the essential transcription antiterminator M2-1 protein of human respiratory syncytial virus and implications of its phosphorylation. *Proc. Natl Acad. Sci. USA* **111**, 1580–1585 (2014).
52. Richard, C.-A. et al. RSV hijacks cellular protein phosphatase 1 to regulate M2-1 phosphorylation and viral transcription. *PLoS Pathog.* **14**, e1006920 (2018).
53. Khuperkar, D. et al. Quantification of mRNA translation in live cells using single-molecule imaging. *Nat. Protoc.* **15**, 1371–1398 (2020).
54. Yan, X., Hoek, T. A., Vale, R. D. & Tanenbaum, M. E. Dynamics of translation of single mRNA molecules in vivo. *Cell* **165**, 976–989 (2016).

Methods

Cell culture

Cell lines. A549 (CCL-185, American Type Culture Collection (ATCC)), BSR T7/5 (ref. 55) (BHK-21 cells that constitutively express the T7 RNA polymerase, RRID:CVCL_RW96) and HEK293T cells (CRL-3216, ATCC) were cultured in DMEM (31966021, Thermo Fisher Scientific) supplemented with 10% fetal bovine serum (FBS; F7524, Merck) and 1% penicillin–streptomycin (pen–strep; 15140122, Thermo Fisher Scientific). Vero cells (CCL-81, ATCC) were cultured in DMEM supplemented with 5% FBS and 1% pen–strep. HEp-2 cells (CCL-23, ATCC) were cultured in MEM (42360032, Thermo Fisher Scientific) with 10% FBS and 1% pen–strep. All cells were maintained at 37 °C and 5% CO_2. Cell lines used in this study were confirmed to be mycoplasma negative.

Primary cells. Primary human nasal epithelial cells (HNECs) from healthy donors (EP51AB, Epithelix) were cultured in an air–liquid interface (ALI) transwell system, as previously described[56]. In brief, HNECs were expanded to log phase in PneumaCult Ex Plus medium (05040, StemCell Technologies). Passage 1 cells were cryopreserved in 78% Ham's F12 (51651C, Merck/Sigma), 10% heat-inactivated FBS, 2% HEPES (pH 7.2) and 10% DMSO, then stored at −135 °C. After thawing, cells were expanded with medium, replaced every 1–2 days, then seeded at a density of 7×10^4 cells per well on PET transwells (CLS3470, Corning; 0.4-µm pores, 6.5 mm in diameter) with 100 µl apical and 650 µl basolateral PneumaCult Ex Plus medium. After 48–72 h, confluent monolayers were airlifted by aspirating media and adding PneumaCult ALI medium (05001, StemCell Technologies) supplemented with 100 U ml^{-1} penicillin, 0.1 mg ml^{-1} streptomycin (P4333, Sigma), 0.48 µg ml^{-1} hydrocortisone (07926, StemCell Technologies) and 4 µg ml^{-1} heparin (07980, StemCell Technologies) to only the basolateral chambers. Medium was replaced every 2–3 days; from 2 weeks post-airlift, apical surfaces were washed 1–2 times weekly with 200 µl HBSS (14025050, Gibco) to remove mucus. Cultures were maintained at 37 °C with 5% CO_2.

Nasal wash samples

Nasal wash samples from individuals infected with RSV were obtained from participants enrolled in a previously described controlled human infection model (CHIM) study[57]. That study, conducted independently of the present work, involved inoculation of healthy adults with RSV-A Memphis-37b[58]. Nasal wash samples were collected at defined time points, frozen and stored for subsequent analysis. For the present study, nasal wash samples collected from a single participant on study days 4 and 5, which showed detectable nasal viral load as determined by quantitative PCR with reverse transcription (RT–qPCR), were utilized.

RSV protein samples

RSV Nrings without tag were purified by co-expression in *Escherichia coli* and co-purification with GST–P_{CTD} (amino acids 161–241), using the GST tag, as previously described[19]. When specified, the GST tag was removed by thrombin cleavage. For NMR measurements, ^{15}N-labelled P_{CTD} was expressed in *E. coli* from P_{CTD} cloned into the pGEX-4T3 plasmid, and purified as previously described[59]. For expression and purification of all the GST–P fragments, the corresponding P sequences were cloned into pGEX-4T3 plasmid, and the proteins were expressed in *E. coli*. Purifications were performed as previously described[19].

Screening of DARPins binding to RSV vRNP

To generate DARPin binders for the GST–P_{CTD} + Nrings complex, the biotinylated GST–P_{CTD} + Nrings complex was immobilized alternatingly on either MyOne T1 streptavidin-coated beads (65601, Thermo Fisher Scientific) or Sera-Mag neutravidin-coated beads (78152104011150, Cytiva) depending on the selection round. Ribosome display selection was performed as previously described[60], but using a semiautomatic KingFisher Flex MTP96 well platform.

The fully synthetic library includes N3C-DARPins with three randomized internal repeats with the original randomization strategy as reported[61], but including a stabilized C-cap[18,62,63]. In addition, the library is a 1:1 mixture of DARPins with randomized and non-randomized N-caps and C-caps, respectively[18,64], and successively enriched pools were ligated in a ribosome display-specific vector[60]. Selection was performed over four rounds with decreasing concentrations of biotinylated GST–P_{CTD} + Nrings complex (250 pmol, 125 pmol and 5 pmol) for the first three rounds and 50 pmol of target for the last recovery round, and increasing washing steps[60,65]. For rounds 2–4, prepanning with biotinylated GST was used to remove potential binders against GST.

To screen individual DARPins for their binding properties, the selected pool of DARPins from ribosome display was subcloned by restriction digest with BamHI and HindIII into the pQE30-derived bacterial expression vector pQIq (Qiagen). This creates DARPins with an N-terminal MRGS(H_6) tag and a C-terminal FLAG-M2 tag. Single DARPin clones ($n = 192$) were screened against the GST–P_{CTD} + Nrings complex and GST only, both directly immobilized, by a crude extract ELISA. The crude extracts were prepared as previously described[66]. Thirty-two identified DARPin clones were sequenced and 13 of these clones were unique in their sequence. These 13 clones were IMAC purified and validated in an ELISA, as previously described[66], against the GST–P_{CTD} + Nrings complex and GST.

Purified DARPin-P production

DARPin-H6 with an N-terminal MRGS(H_6) tag and a C-terminal FLAG-M2 tag (His$_6$–DARPin–H6–FLAG, referred to as DARPin–H6 in Fig. 1 and DARPin-P thereafter, originally obtained as 011-1055-C6-2605-H5 in the selection), was cloned into the pQIq vector backbone[67] (Supplementary Table 1). The plasmid was further modified to generate fluorescent protein fusions: DARPin-P–BFP, DARPin-P–sfGFP and DARPin-P–mRuby3 (Supplementary Table 1). DARPin-P and the fluorescent fusion proteins were recombinantly expressed in *E. coli* XL-1 blue cells (200249, Agilent) and purified using the MRGS(H_6) tag. In brief, a 20 ml primary culture of transformed cells was grown overnight in 2× YT medium (Y2377-250G, Merck) supplemented with 1% glucose and 100 µg ml^{-1} ampicillin (A5354-10ML, Merck) at 37 °C with shaking at 160 rpm. The primary culture was diluted into 400 ml of the same medium and incubated at 37 °C with shaking at 160 rpm until the OD_{600} reached 0.5–0.8. Protein expression was induced with 0.5 mM IPTG (AM9464, Thermo Fisher Scientific), and the culture was further incubated at 37 °C and 160 rpm for 4 h. Cells were harvested by centrifugation at 4,000*g* for 20 min and stored at −20 °C until use. The cell pellets were thawed and resuspended in 25 ml of buffer A (PBS, pH 7.2, supplemented with 150 mM NaCl and 30 mM imidazole) containing 5% (v/v) glycerol and cOmplete Mini EDTA-free Protease Inhibitor Cocktail (11836170001, Merck). Cells were lysed by sonication, and the lysate was clarified by centrifugation at 20,000*g* for 30 min. The resulting clear supernatant was loaded onto an Ni-NTA agarose column (R90115, Thermo Fisher Scientific), which was subsequently washed with 20 column volumes (CV) of buffer A. Bound MRGS(H_6)-tagged proteins were eluted using buffer A supplemented with 400 mM imidazole. Fractions containing the recombinant protein were pooled, and the imidazole was removed using a PD SpinTrap G-25 Desalting Column (28918004, Cytiva). Purified proteins were stored as single-use aliquots at −80 °C until further use.

DARPin-P characterization

Mass spectrometry. DARPin-P immunoprecipitation on RSV virions for mass spectrometry. Sucrose purified RSV ($4.4–9.2 \times 10^7$ plaque-forming units (PFU)) per condition were lysed in ice-cold RIPA lysis buffer (50 mM Tris pH 7.5, 150 mM NaCl, 0.1% sodium dodecyl sulfate (SDS), 0.5% sodium deoxycholate and 1% Triton X-100) supplemented with 100 µg ml^{-1} AEBSF serin protease inhibitor (78431, Thermo Fisher Scientific). Purified DARPin-P (12.5 µg) was adsorbed with 10 µl anti-DYKDDDDK magnetic agarose (A36797, Thermo Fisher

Scientific) for 1 h at 4 °C in RIPA lysis buffer under mild rotation. DARPin-P-adsorbed beads or untreated beads were washed in RIPA lysis buffer before incubating with virus lysate for 2 h at 4 °C followed by five washes in ice-cold RIPA lysis buffer. Proteins were eluted in 1% SDS in D-PBS at 50 °C under agitation. For proteomic analysis, three replicates were generated.

Immunoprecipitation for phosphorylation mass spectrometry. A549 cells (7.5×10^5) infected with RSV for 24 h were lysed in ice-cold RIPA lysis buffer supplemented with 100 μg ml^{-1} AEBSF serin protease inhibitor and 1× PhosSTOP (4906837001, Roche). Purification was performed either with anti-RSV P (polyclonal; see details below) for total P or with DARPin-P as follows: for total P, 10 μg anti-RSV P (polyclonal) antibody was incubated with whole-cell lysate for 1 h at 4 °C in RIPA lysis buffer under mild rotation. Protein A and protein G magnetic beads (50 μl 1:1; 10002D and 10004D, Thermo Fisher Scientific) were washed and added for 1 h at 4 °C, washed three times with ice-cold RIPA and eluted in 1% SDS in D-PBS at 50 °C under agitation. For DARPin-P purification, 12.5 μg purified DARPin-P was adsorbed with 10 μl Pierce anti-DYKDDDDK magnetic agarose (A36797, Thermo Fisher Scientific) for 1 h at 4 °C in RIPA lysis buffer under mild rotation. DARPin-P-adsorbed beads were washed in RIPA lysis buffer before incubating with whole-cell lysate for 2 h at 4 °C followed by three washes in ice-cold RIPA lysis buffer. Proteins were eluted in 1% SDS in D-PBS at 50 °C under agitation. For phospho-proteomic analysis, three replicates were generated.

Protein digestion for proteomics analysis. Immunoprecipitation eluates were precipitated onto 400 μg of carboxyl-coated beads (45152105050250 and 65152105050250, Cytiva), washed and digested according to a standard solid-phase-enhanced sample preparation (SP3) protocol[68] using 50 ng of sequencing grade trypsin (V5111, Promega).

Phospho-enrichment. Following digestion, samples were desalted using the Oasis HLB 96-well μElution Plate (186001829, Waters), as per the manufacturer's instructions. Peptides were eluted in 25 μl of elution (phospho-enrichment loading solvent) containing 80% acetonitrile, 1 M glycolic acid, 6% trifluoroacetic acid (TFA) and 0.4 mg of pre-equilibrated MagReSyn Zr-IMAC beads were added to each sample (MR-ZRM002, Resyn Biosciences). Samples were incubated for 20 min (at room temperature at 1,350 rpm), then washed once in 400 μl of loading solvent, twice in 400 μl wash buffer 1 (30% acetonitrile and 1% TFA), and twice in 400 μl wash buffer 2 (10% acetonitrile and 0.1% TFA). Phospho-peptides were then eluted with 4% ammonium hydroxide for 10 min (at room temperature at 1,350 rpm). The elution step was repeated twice more, and eluates were acidified with formic acid to a final concentration of 5%. The collected peptides were then desalted using the Oasis HLB plate and eluted once in 25 μl SPE elution buffer (50% acetonitrile and 0.1% formic acid in water) and then diluted in 100 μl 5% DMSO and 5% formic acid before liquid chromatography–tandem mass spectrometry analysis.

Mass spectrometry. Analysis of immunoprecipitation peptides was carried out using an Ultimate 3000 nano-LC 1000 system coupled to an Orbitrap Exploris (Thermo Fisher Scientific). Phospho-enriched peptides were analysed using an Ultimate 3000 nano-LC 1000 system coupled to an Orbitrap Ascend Tribrid Mass Spectrometer (Thermo Fisher Scientific). Peptides were initially trapped on a C18 PepMap100 pre-column (300 μm inner diameter × 5 mm, 100 A) and then separated on an in-house built C18 column (Reprosil-Gold, Dr. Maisch, 1.9-μm particle size) column (ID: 50 μm, length of 50 cm) at a flow rate of 100 nl min^{-1}. Total immunoprecipitation peptides were separated over 60 min (10–33% B) and phospho-enriched peptides were separated over 30 min (10–36% B). In both cases, mobile phase A (water, 5% DMSO and 0.1% formic acid) and mobile phase B (acetonitrile, 5% DMSO and 0.1% formic acid) were used. Separated peptides were directly electrosprayed into the mass spectrometer. Mass spectra were acquired in the Orbitrap (350–1,400 m/z, resolution of 60,000, automatic gain control (AGC) target of 3 × 106 and maximum injection time of 50 ms) in a data-dependent mode. For total immunoprecipitation samples, the top 40 most-abundant peaks in the survey scan were fragmented using higher-energy collisional dissociation (HCD, resolution of 7,500, AGC target of 4 × 104 and maximum injection time of 64 ms). For phospho-enriched samples, the top 30 most-abundant peaks in the survey scan were fragmented using HCD (MS2 scans were acquired using the ion trap analyser in Turbo mode; AGC target of 2 × 104 and maximum injection time of 35 ms).

Phosphorylation analysis of DARPin-P-isolated RSV P. A549 cells (5×10^5) infected with RSV for 24 h were lysed in ice-cold RIPA lysis buffer supplemented with 100 μg ml^{-1} AEBSF serin protease inhibitor and 1× PhosSTOP (4906837001, Roche). Purification was performed either with anti-RSV P (polyclonal) for total P or with DARPin-P as follows: for total P, 10 μg anti-RSV P (polyclonal) antibody was incubated with 50 μl 1:1 protein A and protein G magnetic beads (10002D and 10004D, Thermo Fisher Scientific) for 1 h at 4 °C, washed with D-PBS and crosslinked to the beads with 2.5 mM BS3 (A39266, Thermo Fisher Scientific) for 30 min at room temperature before quenching with 50 mM Tris pH 7.4 for 15 min. After washing three times in RIPA, beads were incubated with whole-cell lysate for 1 h at 4 °C, three times with ice-cold RIPA and eluted in 1% SDS in D-PBS at 50 °C under agitation. For DARPin-P purification, 12.5 μg purified DARPin-P was adsorbed with 10 μl Pierce anti-DYKDDDDK magnetic agarose (A36797, Thermo Fisher Scientific) for 1 h at 4 °C in RIPA lysis buffer under mild rotation. DARPin-P-adsorbed beads were washed in RIPA lysis buffer before incubating with whole-cell lysate for 2 h at 4 °C followed by three washes in ice-cold RIPA lysis buffer. Proteins were eluted in 1% SDS in D-PBS at 50 °C under agitation. Three replicates were generated. For phosphorylation analysis 50 μM or 100 μM Phos-Tag-acrylamide (TA9H9A175FCA, Merck) containing 12% SDS–PAGE, gels were generated, samples separated at 180 V and washed in transfer buffer with 1 mM EDTA followed by wash in transfer buffer before being transferred to nitrocellulose membranes. Samples were blocked in 3% milk in D-PBS-T before probing with anti-RSV P (polyclonal) at a 1:1,000 dilution, using donkey anti-rabbit IgG (H + L) highly cross-adsorbed secondary antibody, Alexa Fluor Plus 680 (A32802, Thermo Fisher Scientific) for detection with a Li-COR Odyssey Fc.

NMR. NMR experiments were carried out on a Bruker 800 MHz Avance III spectrometer equipped with a TCI cryoprobe. Protein samples were dialysed into PBS at pH 6.4 and mixed or diluted to obtain the desired final concentration. All samples contained 7.5% D_2O as a lock substance. ^{1}H–^{15}N HSQC spectra were acquired on samples with ^{15}N-P$_{\mathrm{CTD}}$ (50 μM) at a temperature of 288 K. The GST purification tag was removed from ^{15}N-P$_{\mathrm{CTD}}$, which ensured that the protein was monomeric and precluded any steric hindrance that might interfere with binding. NMR data were processed with TopSpin 4.0 (Bruker) software and analysed with CcpNMR Analysis software[69]. Amide assignment of ^{15}N-P$_{\mathrm{CTD}}$ was previously performed (Biological Magnetic Resonance Bank entry ID 26906)[59].

Native agarose gel electrophoresis. Samples in the presence of 50% sucrose loading buffer were loaded on native 1% agarose gel and migration was performed in 1× Tris–glycine buffer during 1 h 30 min at 80 V before staining with amido black 10B[70].

BLI. Purified MRGS(H_6)-tagged DARPin-P (ligand) was diluted in BLI assay buffer (PBS + 0.01% bovine serum albumin (BSA) + 0.002% Tween 20, pH 7.4) at room temperature. Ligand at 20 μg ml^{-1} was loaded on His1K (anti-penta-his) biosensors (Sartorius) for 150 s. Kinetic experiments were performed at 30 °C with 1,000 rpm shaking in 96-well black plates using the Octet Red 96e system (Fortebio). Biosensors loaded with DARPin-P were successively equilibrated for 60 s in assay buffer (baseline step), incubated in a dilution of the analyte GST–P$_{\mathrm{CTD}}$ (twofold from 350 nM to 5.5 nM) for 150 s (association step), then incubated in assay buffer for 600 s (dissociation step). One ligand-bound sensor was incubated in assay buffer as a reference to measure signal drift. As references for binding specificity, biosensors in the absence of ligand were used in a parallel kinetics experiment. Real-time binding kinetics were analysed and calculated using the Octet Red software package (v9.0). Raw signal was processed using the double-reference method, by subtracting both the biosensors without ligand (unspecific signal) and the signal in the absence of analyte (drift), after baseline alignment and interstep correction at the dissociation. Kinetic modelling was done by analysing association and dissociation signals using global fitting with a 1:1 model.

Reporter cell line generation

Plasmids for lentiviral vectors. Self-inactivating lentiviral vectors were based on the pHR vector backbone under the control of the spleen focus-forming virus (SFFV) promoter. The WPRE element was omitted to aid in obtaining low transgene expression levels (pHR-pSFFV-insert-ΔWPRE). The sequences of the inserted transgenes are listed in Supplementary Table 1.

Lentiviral transduction. All cell lines that stably express transgenes were generated via lentiviral transduction. Unless stated otherwise, transgenes were introduced into A549 cells. Lentivirus was produced by polyethylenimine transfection (23966, Polysciences) of lentiviral plasmid carrying the transgene of interest and the helper plasmids pMD2G and psPAX2. Three days after transfection the supernatant containing lentivirus was collected and filtered (0.45-µm filter) to remove cellular debris, and was added to recipient cells of interest along with 10 mg ml^{-1} polybrene (sc-134220, Santa Cruz Biotechnology) and subject to spin infection for 120 min at 2,000 rpm at 25 °C. Following spin infection, the medium was refreshed, and after two passages, single cells from polyclonal cell populations were sorted in 96-well plates by FACS. The fluorescence expression level for each individual cell line was carefully determined by initial investigation on the polyclone followed by screening of multiple monoclones. In general, reporter cell lines were selected with low levels of cytoplasmic fluorescence (to have minimal fluorescence background and suppress aggregate formation). Furthermore, we only selected cell lines in which RSV infection kinetics were not affected compared with parental cell lines. If a cell line required the expression of multiple transgenes, lentiviral transduction was either carried out simultaneously (maximally two different lentiviruses) or sequentially (minimally starting from 3 days following spin infection). The specific cell lines used in each experiment is listed in Supplementary Table 1.

RSV strains, design, production and validation

Strains. Unless otherwise stated, human RSV, subgroup A, strain Long, (ATCC VR-26, GenBank AY911262.1; referred to as RSV (Long strain)) was used. In addition, the laboratory strains, human RSV-A2 (ATCC VR-1540) and RSV-98-25147-X (GenBank FJ948820; referred to as RSV-X) and two RSV subgroup A clinical isolates (03-036465 (GenBank JQ901457.1) and 18-0011989) were used for specified experiments. The RSV clinical isolates were provided by M. C. Viveen and F. Coenjaerts, and further information about their isolation, assessment and storage has been previously described[71].

Design. All viral sequences were derived from RSV (Long strain). Engineered RSV strains were designed based on a previously established recombinant human RSV reverse genetics system in which unique restrictions sites have been introduced between individual RSV genes to facilitate cloning of the viral genome (reverse genetics vector pACNR-rHRSV)[17].

The recombinant RSV virus encoding for an additional mCherry fluorescent protein (located between the P and M genes on the viral genome) encoded by the pACNR-rHRSV-mCherry was previously described[17].

The genome expression construct encoding for recombinant upstream and downstream SunTag^{eng} RSV, were generated by designing introduction of the SunTag gene inserts at the MluI restriction site between P and M genes and BstEII restriction site between F and M2 for the upstream and downstream strains, respectively. The introduced SunTag genes were designed to contain the same gene-regulatory elements, gene start (GS), gene end (GE) and the 5′ and 3′ untranslated regions (UTRs), as the N gene. Furthermore, the reporter genes were introduced such that the gene-regulatory elements of the upstream and downstream genes with respect to the insert location were not disrupted. The coding sequence of the reporter genes contained a translation start codon in an optimal Kozak sequence (GCCACCATGG), followed by a sequence encoding a SunTag array and downstream gene (to generate a longer transcript allowing for more ribosomes to simultaneously translate the SunTag-encoding mRNAs, which results in higher fluorescence signal of translation sites). The upstream reporter carries a 24×SunTag–BFP and the downstream reporter carries a 12×SunTag–Kif18b. The sequences of the additional SunTag genes introduced are provided in Supplementary Table 1.

The engineered RSV strains carrying endogenously tagged RSV proteins (P and L) were designed by targeting regions in the respective gene sequence that have previously been shown to be conducive for insertions with minimal disruption to viral function. An ALFA tag was inserted into the coding sequence of P at amino acid 72 (ref. 37) to generate a P-ALFA-tag^{eng} RSV and an HaloTag was inserted into the coding sequence of L at amino acid 1749 (refs. 72,73) to generate a L-HaloTag^{eng} RSV. All insertions were flanked by flexible linker sequences (ALFA tag flanked by 5′ and 3′ six-amino-acid-long linkers and HaloTag flanked by a 5′ 18-amino-acid and 3′ 14-amino-acid linker). The engineered gene sequences are provided in Supplementary Table 1.

Generation of plasmids encoding recombinant RSV strains. The pACNR reverse genetics vectors containing the RSV genomes with the upstream and downstream SunTag genes were generated by Gibson assembly and correct insertion verified by sequencing the insert and the gene upstream and downstream of the insert location.

The reverse genetics vectors carrying the P-ALFA-Tag^{eng} and L-HaloTag^{eng} RSV strains were generated by transformation-associated recombination (TAR) cloning in yeast as previously described[74]. In brief, overlapping PCR products containing the RSV genome, ALFA tag/HaloTag and TAR vector (pCC1BAC-His3)[75] were transformed into the yeast strain VL6-48N[76]. Yeast-assembled full-length clones were isolated, amplified in *E. coli* strain EPI300 and sequences were verified by full-plasmid nanopore sequencing (Plasmidsaurus), where remaining uncertainties in the viral sequence were confirmed by Sanger sequencing.

RSV rescue and concentration. Recombinant WT and tagged RSV strains were rescued by reverse genetics and amplified in HEp-2 cells as previously described[77]. In brief, the appropriate pACNR reverse genetics vector (1.25 µg) was co-transfected together with the expression vectors pCITE-N (1 µg), pCITE-P (1 µg), pCITE-L (0.5 µg) and pCITE-M2-1 (0.25 µg)[17,78], each under the control of the T7 promoter[72] in BSR T7/5 using Lipofectamine 3000 (L3000001, Thermo Fisher Scientific), according to the manufacturer's protocol. Three days following transfection, virus was collected and efficiency of rescue assessed by plaque assay carried out on HEp-2 cells. The viruses were amplified for a subsequent 3–4 passages on HEp-2 cells at an MOI of 0.01 PFU per cell to minimize formation of defective viral genomes. For the P-ALFA-tag^{eng} and L-HaloTag^{eng} RSV strains, the rescue protocol was similar, with the exception that the helper plasmids were in pcDNA3 (NR-36462, NR-36463, NR-36464 and NR-36461, BEI Resources), transfection of BSR T7/5 cells was performed using Lipofectamine LTX (A12621, Thermo

Fisher Scientific), passaging was performed on Vero cells, and viruses were titrated by 50% tissue culture infective dose (TCID$_{50}$) assay. The final stocks were grown on Hep-2 cells. RSV-A2 and RSV-X were propagated in HEp-2 cells and Vero cells, respectively.

Viral supernatants from passage 3–4 were precleared for cells and debris by centrifugation and subsequently concentrated. Concentration was done either via polyethylene glycol-mediated precipitation (viral supernatant was stirred with 10% PEG6000 (50 mM Tris-HCL, pH 7.4, 150 mM NaCl and 1 mM EDTA) for 3 h at 4 °C, followed by centrifugation at 3,500 RCF for 30 min at 4 °C), or by pelleting through a 10% sucrose-containing buffer (50 mM Tris-HCl, pH 7.4, 100 mM NaCl and 0.5 mM EDTA; centrifuge viral supernatant in 10% sucrose buffer (4:1 v/v ratio) at 10,000 RCF for 4 h at 4 °C). The virus containing pellets were resuspended in 10% sucrose in PBS, snap-frozen and stored at −80 °C as single-use aliquots. RSV-A2 and RSV-X were purified between layers of 10% and 50% sucrose by ultracentrifugation, washed with plain RPMI and concentrated on 100-kDa filters (UFC910024, Millipore) by centrifugation. The virus was washed from the filters in phenol red-free RPMI (11835-030, Gibco) supplemented with 10% sucrose and subsequently snap-frozen and stored at −80 °C.

Viral growth assays. Viral growth assays were performed to assess the fitness of the engineered RSV strains with respect to their WT counterpart.

The upstream and downstream SunTag$^{\mathrm{eng}}$ RSV strains growth kinetics were assessed on A549 cells. A549 cells were inoculated with virus at an MOI of 3 PFU per cell (in DMEM + 10% FBS + 1% pen–strep) for 1 h, following which cells were washed in PBS and supplemented with fresh media (DMEM + 10% FBS + 1% pen–strep). New progeny virus production was assessed up to 5 days post-infection by collecting samples at multiple time points along the time course. The viral titres of the samples were determined by plaque assays on HEp-2 cells.

The growth kinetics of the P-ALFA-tag$^{\mathrm{eng}}$ and L-HaloTag$^{\mathrm{eng}}$ RSV strains were assessed on Vero cells via qPCR. Cells were infected with an MOI of 0.04 PFU per cell and supernatant was collected up to 48 h post-infection in MagNA Pure External Lysis Buffer (06374913001, Roche) for RNA isolation. Sample (120 µl) was mixed with 50 µl AMPure XP Reagent (A63880, Beckman Coulter), loaded in a 96-well PCR plate, washed three times with 70% ethanol using a DynaMag-96 Side Skirted Magnet and RNA was eluted in 50 µl RNase-free H$_2$O. RNA, 5 µl per 20 µl reaction volume, was reverse transcribed and amplified in one reaction using the TaqMan Fast Virus 1-step Master Mix (4444432, Thermo Fisher Scientific) according to the manufacturer's protocol on a StepOnePlus System. RSV-A primers with a FAM probe were used (Supplementary Table 1) and a serially diluted RSV-A plasmid was included as a reference.

Assessing RSV P phosphorylation mutations

RSV P phosphorylation mutants, in which the phosphorylation sites overlapping the DARPin-P binding sites were mutated, were generated on the pCITE-P plasmid backbone. The sequences of the inserted phospho-mutant P sequences are listed in Supplementary Table 1. BSR T7/5 cells were transfected with WT P and mutants at 70% confluence in a 96-well glass-bottom plate (MGB096-1-2-LG-L, Brooks Life Science Systems and 89627, Ibidi) with 1 µg of plasmid DNA using Lipofectamine 3000 Transfection Reagent (L3000015, Thermo Fisher Scientific) following the manufacturer's protocol. Twenty-four hours post-transfection, cells were fixed and subject to downstream analysis.

Assessing RSV pseudo-VFs

BSR T7/5 cells were transfected at 70% confluence in a 96-well glass-bottom plate (MGB096-1-2-LG-L, Brooks Life Science Systems and 89627, Ibidi) with a plasmid mixture containing pCITE-P (1 µg) and pCITE-N (1 µg) using Lipofectamine 3000 Transfection Reagent (L3000015, Thermo Fisher Scientific) following the manufacturer's protocol. Twenty-four hours post-transfection, cells were fixed and subject to downstream analysis.

RSV infection for imaging-based studies

Inoculum for RSV infection. One day before imaging, the required A549 cell lines were seeded on 96-well glass-bottom plates (MGB096-1-2-LG-L, Brooks Life Science Systems and 89627, Ibidi) such that cells were at approximately 80–90% confluency at the point of viral inoculum addition. For fixed-cell experiments, the viral inoculum was made in cell culture medium (DMEM + 10% FBS + 1% pen–strep). For live-imaging experiments, viral inoculum was made in imaging medium (CO$_2$-independent Leibovitz's-L-15 media (21083027, Thermo Fisher Scientific) supplemented with 10% FBS and 1% pen–strep).

For live-cell assessment of RSV infection progression and success, a 1:1,000 dilution of RSV glycoprotein G antibody (133; referred to as AbG-fluoro; Janelia Fluor 646, NBP2-50411JF646 and Alexa Fluor 405, NBP2-50411AF405, NOVUS Biologicals) was added directly into the viral inoculum. For visualization of the L-HaloTag$^{\mathrm{eng}}$ RSV, the viral inoculum was supplemented with 5 nM HaloTag ligand JFX650 (ref. 79). Both fluorescent media supplementations gave negligible fluorescence background and was maintained on cells until experimental end point. The details of viral inoculums used in each experiment is listed in Supplementary Table 1.

Nasal wash samples were added undiluted onto the relevant A549 cell lines (as described in the figure legend and Supplementary Table 1) and maintained for 4 h at 37 °C, following which cells were rinsed in PBS and topped with warmed imaging media before imaging.

For ExM, WT A549 cells were grow on 12-mm coverslips (no. 1.5H) such that cells were at approximately 90% confluence at the point of viral inoculum addition. Cells were infected with WT RSV (MOI of 2) in the presence of the translation inhibitor emetine (see below) in cell culture medium. At 4 hpi, cells were fixed, stained and subject to downstream analysis.

MOI used for imaging-based studies. For imaging studies, MOI was based on the fraction of cells containing vRNPs at 6 h following viral inoculum administration. In fixed-cell experiments with WT A549 cells, this was assessed by the presence of N^{+}/F^{-} foci (antibody staining), and in live-cell experiments, this was assessed in the P$^{\mathrm{exo}}$-fluoro transgenic cell line by the presence of P$^{\mathrm{exo}}$ foci. The MOI value established using this imaging-based method is three orders of magnitude higher than the MOI calculated using plaque assay-based viral titration on HEp-2 cells (0.1 imaging-based MOI relates to 0.0001 PFU per cell). Unless otherwise specified, the imaging-based MOI used was between 0.05 and 0.25.

Chemical inhibitors. The following inhibitors were used in this study: PC786 (15 µM, RSV polymerase inhibitor; HY-102038, MedChemExpress), TMC353121 (180 nM, RSV fusion inhibitor; HY-11097, MedChemExpress), emetine dihydrochloride (emetine; 50 µg ml^{-1}; inhibits translation by preventing translocation of the tRNA–mRNA complex; 324693, Merck), cyclopamine (CPM; 4 µM; inhibits RSV infection by disorganizing and hardening VFs; HY-17024, MedChemExpress)[37,38] and puromycin dihydrochloride (puromycin; 0.1 mg ml^{-1}; a tyrosyl-tRNA mimic that blocks translation by releasing elongating polypeptide chains; A1113803, Thermo Fisher Scientific). When used, PC786 and emetine were added directly with the viral inoculum, and TMC353121, CPM and puromycin were added to infected cells at indicated time points. Following addition, the inhibitors were maintained on cells until experimental end point. For multi-day inhibitor treatment protocols, the inhibitors were refreshed after each 24 h.

Assessing infecting vRNPs. Assessment of the viral protein and RNA levels on infecting RSV vRNPs were carried out in the presence of the translation inhibitor emetine. Emetine containing inoculum was maintained on cells for 1 h, following which the RSV fusion inhibitor TMC353121 was added to the inoculum to prevent subsequent infections. Three hours post-fusion inhibitor addition, the cells were assayed, either by live imaging or following fixation and subject to antibody or smFISH staining protocols. This time point was chosen to ensure that all infecting vRNPs had fully separated such that infecting individual vRNPs could be assessed.

Generation and assessment of RSV passaged in different cell types. HNECs cultured in an ALI transwell system were fully differentiated for 5–7 weeks, with maturity confirmed by ciliary beating and mucous production. Three days before infection, basal medium was replaced with complete PneumaCult ALI medium without heparin and hydrocortisone (ALI infection medium). On the day of infection, apical surfaces were washed once with 200 µl HBSS and incubated for 10 min at 37 °C. The apical wash and basal medium were aspirated, and 650 µl fresh ALI infection medium was added to the basal compartment. RSV (Long strain) was diluted in HBSS, and 200 µl of the inoculum was applied per transwell to achieve 1×10^4 $TCID_{50}$ per well. Two wells per donor were infected and incubated for 1 h at 37 °C. The inoculum was aspirated, and cells were washed three times with 200 µl HBSS. Cultures were then maintained at 37 °C and 5% CO_2. Apical washes were collected at 24, 48 and 72 hpi by adding 200 µl HBSS, incubating for 10 min at 37 °C, and collecting the wash for viral quantification. Washes were mixed with sucrose to a final 10% concentration, aliquoted, snap-frozen and stored at −80 °C.

Vero, HEp-2 and A549 cells were seeded in 48-well plates (in the appropriate media, see above), with two wells per cell line per experimental repeat. RSV inoculum was prepared by diluting RSV (Long strain) in MEM. Culture medium was removed, and 100 µl inoculum was added to achieve 1×10^4 $TCID_{50}$ per well. Cells were incubated with the inoculum for 3 h at 37 °C, then inoculum was aspirated, and cells were washed twice with PBS. Fresh medium containing 2% FBS was added. At 24, 48 and 72 hpi, supernatants were collected, mixed with sucrose to 10% final concentration, aliquoted, snap-frozen and stored at −80 °C.

The 72 hpi viral supernatant samples were used for subsequent analysis. Viral supernatants were titrated on the P^{exo}-fluoro A549 cell line and used at an MOI of 0.05.

Immunofluorescence

A detailed step by step protocol for immunofluorescence on different samples can be found in Supplementary Information.

Antibody conjugation. RSV nucleoprotein antibody (RSV3132 (B023); referred to as anti-RSV N; NB100-64752, NOVUS Biologicals) was fluorescently labelled using N-hydroxysuccinimide (NHS)-esters (Alexa Fluor 555 NHS ester and Alexa Fluor 647 NHS ester; AF555, A20009, AF647 and A20106, Thermo Fisher Scientific) for use in immunofluorescence. The antibody was buffer exchanged and concentrated with a 10 kDa MWCO PES concentrator (88535, Thermo Fisher Scientific) to yield 3 mg ml^{-1} antibody solution in 7.5% sodium bicarbonate buffer, pH 8.3 (25080094, Thermo Fisher Scientific). The dye-NHS stocks were prepared in anhydrous DMSO (AM9342, Thermo Fisher Scientific). A threefold molar excess of the dye-NHS was incubated with 1 mg of the antibody for 2 h at room temeprature with continuous rotation. Free dye was removed using a PD SpinTrap G-25 Desalting Column (Cytiva). Protein concentration and degree of labelling (fluoro-to-protein ratio) were determined using NanoDrop spectrophotometric absorbance values. All antibody conjugations yielded a degree of labelling of 2–3 dyes per antibody.

Immunofluorescence of infected cells and RSV virions on glass. Infected cells and uninfected control cells were fixed with 4% paraformaldehyde (043368.9M, Thermo Fisher Scientific) for 10 min at room temperature at experimental end point. All fluorescence of genetically encoded fluorescent proteins was maintained following this fixation and antibody staining protocol. If virions attached to the extracellular membrane of cells needed to be stained, RSV glycoprotein F antibody (11-2-F3; referred to as anti-RSV F; DyLight550, NBP2-50412R and Alexa Fluor 488, NBP2-50412AF488, NOVUS Biologicals) staining was carried out before permeabilization and blocking. Antibody diluted to the appropriate concentration in PBS + 10% FBS was added to cells and incubated for 1 h at room temperature (1:500 anti-RSV F (AF488/DL550)). Following incubation, samples were washed three times in PBS. Samples were subsequently blocked and permeabilized, simultaneously, with blocking buffer (PBS + 10% FBS + 0.05% Triton X-100) for 1 h at room temperautre. Antibodies and recombinant proteins were diluted to the appropriate concentration in blocking buffer and were incubated for 1 h at room temperature or overnight at 4 °C (for recombinant proteins: 1:1,000 of 0.4 mg ml^{-1} DARPin-P-mRuby3, 1:1,000 of 0.4 mg ml^{-1} DARPin-P-sfGFP, 1:500 of 0.4 mg ml^{-1} DARPin-P; for antibodies: 1:1,000 (for ExM, 1:100) of 0.5 mg ml^{-1} anti-RSV N (AF555/AF647), 1:1,000 RSV phosphoprotein antibody (2H102; Janelia Fluor 646; referred to as anti-RSV P (JF646); NBP2-50276JF646, NOVUS Biologicals), 1:10,000 (for ExM, 1:5,000) rabbit anti-P antiserum[80] (referred to as anti-RSV P (polyclonal)), 1:1,000 RSV M2-1 protein antibody (5H5; Alexa Fluor 647; referred to as anti-RSV M2-1 (AF647); NBP2-50481AF647, NOVUS Biologicals). Following incubation, samples were washed three times in wash buffer (PBS + 0.05% Triton X-100). If secondary antibody staining was required, the antibodies were diluted to the appropriate concentration in blocking buffer and were incubated for 1 h at room temperature (1:300 of DYKDDDDK tag monoclonal antibody (FG4R; DyLight 488; referred to as anti-FLAG tag-DL488; MA1-91878-D488, Thermo Fisher Scientific), 1:300 of donkey anti-rabbit IgG (H + L) highly cross-adsorbed secondary antibody (Alexa Fluor 568; referred to anti-rabbit-AF568; A10042, Thermo Fisher Scientific). Following incubation, samples were washed three times in wash buffer (PBS + 0.05% Triton X-100). Following incubation, samples were washed three times in wash buffer. If whole-cell segmentation was required, total protein was stained using Pacific Blue succinimidyl ester (Thermo Fisher Scientific; 1:2,000 of 1 mg ml^{-1} stock solution made up in anhydrous DMSO) in PBS for 10 min at room temperature followed by three washes in wash buffer. Samples were kept in PBS at 4 °C until imaging. To visualize extracellular G protein expression on RSV infected cells, 1:1,000 dilution of AbG-fluoro (JF646/JF405) was added directly to the cell culture media and maintained for 30 min at 37 °C. Following incubation, the cells were washed three times in PBS, fixed and stained, as described above.

Virion protein levels were assessed by incubating RSV inoculum in PBS (total volume 100 µl) for 1 h at 37 °C directly in a well of a 96-well square glass-bottom plate. Following incubation, virions were fixed by adding 4% paraformaldehyde directly into the inoculum and incubating for 15 min at room temperature. The antibody staining was carried out as described above. In addition to the antibodies listed above, 1:1,000 FluoTag-X2 anti-ALFA (Atto 488; referred to as anti-ALFA (Atto488); N1502, NanoTag Biotechnologies) was used for virion labelling.

All antibodies, purified proteins and staining protocols used in this study have been optimized to yield minimal to no background foci signal, such that the staining can be used to evaluate RSV infections at a single vRNP resolution. The specific antibody–fluorescent conjugations used per experiment are listed in Supplementary Table 1.

smFISH

A detailed step-by-step protocol for smFISH staining on different samples can be found in Supplementary Information.

smFISH probe generation. Stellaris probe designer (https://www.biosearchtech.com/support/tools/design-software/stellaris-probe-designer) was used to design probes targeting the entirety and subregions of the negative-sense RSV genome, intergenic regions of the positive-sense RSV antigenome (to minimize cross-reactivity with viral mRNAs), positive-sense RSV transcript mRNAs and SunTag mRNA. For detection of defective viral genomes (DVGs), probes targeting the first 1,000 bp of the RSV 5′ trailer region were used, based on the strong enrichment of copy-back DVG rejoin junctions within this area[28,29]. This design enables sensitive and robust detection of diverse DVG species, as previously validated by PCR and RNA sequencing methodologies in clinical and experimental samples[28,29]. Oligonucleotide probes were ordered from Integrated DNA technologies (sequences are listed in Supplementary Table 1). All probes targeting a single RNA were pooled and labelled with ddUTP-coupled ATTO 565 (AD565-31, ATTO-Tec) or ATTO 633 (AD633-31, ATTO-Tec) dyes using terminal deoxynucleotidyl transferase (EP0161, Thermo Fisher Scientific) as previously described[81]. For the RSV transcriptome, probes targeting all RSV transcripts were pooled. Fluorescent probes were purified by ethanol precipitation and resuspended in nuclease-free water to a final stock concentration of 30 µM.

smFISH of infected cells. The smFISH staining procedure was carried out as previously described[82]. In brief, following fixation, cells were washed three times in PBS, permeabilized in 100% ethanol for 1 h at 4 °C and then washed three times for 15 min in smFISH wash buffer (2× saline-sodium citrate (SSC), 10% formamide (17899, Thermo Fisher Scientific) in nuclease-free water) at room temperature. Labelled smFISH probes were diluted to 10 nM in hybridization buffer (1% dextran sulfate (D8906, Merck), 2× SSC, 10% formamide, 1 mg ml^{-1} tRNA (R1753, Merck), 2 mM ribonucleoside vanadyl complex (S1402S, New England Biolabs) and 200 µg ml^{-1} BSA (AM2616, Thermo Fisher Scientific) in nuclease-free water) and hybridization was performed at 37 °C for 16 h. Unbound smFISH probes were removed by 3 × 30 min washes in smFISH wash buffer at 37 °C and a 15 min wash at room temperature. If whole-cell segmentation was required, total protein was stained using Pacific Blue succinimidyl ester (1:2,000 of 1 mg ml^{-1} stock solution; P10163, Thermo Fisher Scientific) in PBS for 10 min at room temperature followed by a 15 min wash with smFISH wash buffer at room temperature. Samples were stored at 4 °C and imaged in smFISH imaging buffer (10 mM Tris pH 8, 2× SSC and 0.4% glucose, supplemented with glucose oxidase (G2133, Merck) and catalase (C3515, Merck)). Imaging was performed within 3 days after probe hybridization. The specific smFISH probe sets used in each experiment are listed in Supplementary Table 1.

smFISH of virions and vRNPs on glass. Virion and vRNP vRNA levels were assessed by incubating RSV inoculum in PBS or PBS + 1% Triton X-100 (total volume of 100 µl), respectively, for 4 h at 37 °C directly in a well of a 96-well square glass-bottom plate. Following incubation, samples were fixed by adding 4% paraformaldehyde directly into the inoculum and incubating for 15 min at room temperature. smFISH staining was carried out as mention above with minor modifications aimed at enhancing accessibility for the smFISH probes to bind to the vRNA. Following fixation and washing, vRNPs were permeabilized in 80% ethanol overnight at 4 °C and then washed once for 15 min in smFISH wash buffer at room temperature. Samples were incubated in 80% formamide for 40 min at 37 °C followed by 2 × 15 min washes in smFISH buffer at room temperature. Samples were incubated with 1:2,000 proteinase K in 2× SSC (124568, Merck) for 1 h at room temperature and washed 2 × 15 min in smFISH buffer at room temperature. Probe hybridization and subsequent steps in the protocol were carried out as above.

Combining smFISH and N antibody staining. To combine smFISH with anti-RSV N antibody staining, the wash buffer was additionally supplemented with 3% BSA and the fluorescently conjugated antibody was directly added into the smFISH hybridization buffer at a 1:100 dilution. The remaining protocol is carried out as detailed above.

Combined smFISH and STAb staining. To combine smFISH with STAb–sfGFP staining, after the three washes with smFISH wash buffer at 37 °C, samples were incubated with purified scFv–sfGFP–STrepII[16] (STAb–sfGFP; 1:100 dilution in PBS + 10% BSA) for 1 h at room temperature. Following incubation, samples were washed three times in PBS. A final room temperature wash step of 30 min in smFISH wash buffer was then performed before sample storage and imaging in smFISH imaging buffer.

Combining smFISH staining with fluorescence originating from transgenic cell lines. For the P^{exo}-fluoro cell line, used to visualize all RSV vRNPs, the foci signal (in the AausFP1 fluorescent protein) was well retained following the smFISH protocol and can be visualized simultaneously with the smFISH foci. For the DARPin-P visualizing transgenic cell line, the foci signal (in the BFP fluorescent protein) was somewhat compromised following the smFISH protocol and as such needed to be first imaged post-fixation, but before ethanol permeabilization, and then followed by the smFISH protocol. When DARPin-P signal visualization with smFISH signals were required, experiments were only carried out in the P^{exo}-fluoro and DARPin-P-fluoro combined transgenic line. Acquiring the P^{exo} signal both in the post-fixation and post-smFISH imaging rounds allowed it to be used to align the data from the two acquisition rounds, ensuring that accurate values for the DARPin-P signal (from post-fixation imaging) could be used for the cells being analysed.

ExM

ExM was performed as previously described[32] with some adaptations. Stained samples were crosslinked with 1.2% paraformaldehyde (11586711, Thermo Fisher Scientific)–3% acrylamide (A4058, Sigma-Aldrich) in PBS for 3 h, washed three times with PBS and incubated for 5 min in monomer solution (1× PBS, 2 M NaCl, 2.5% (w/w) acrylamide, 0.15% (w/w) N,N′-methylenebisacrylamide (M1533, Merck) and 8.625% (w/w) sodium acrylate (408220, Sigma-Aldrich)). Coverslips were placed on top of a drop of 90 µl of freshly prepared gelation solution (monomer solution supplemented with 0.2% (w/w) TEMED (T9281, Sigma-Aldrich) and 0.2% (w/w) APS (A7460, Sigma-Aldrich)) and incubated for 1 h at 37 °C. Gels were then incubated in digestion solution (8 units per millilitre proteinase K (1.24568, Merck), 1× TAE, 0.5% Triton X-100 (X100, Sigma-Aldrich) and 0.8 M guanidine HCl (G3272, Sigma-Aldrich) for 3 h at 37 °C and washed in PBS containing DAPI (1 µg ml^{-1}). Expansion was performed by several washings with excess volume of Milli-Q water (approximately 4.5-fold expansion). Expanded samples were immobilized on 25 mm (no. 1.5H) coverslips covered with 0.01% (w/v) poly-L-lysin (P8920, Sigma-Aldrich) and imaged.

Flow cytometry-based assessment of successful RSV infections

A flow cytometry-based assay quantifying expression of viral G protein by infected cells was used as a readout of successful RSV infections. This assay was used to assess RSV infection success in the DARPin-P-fluoro transgenic A549 cell line compared with WT A549 cells. WT A549 cells and DARPin-P-fluoro cells were plated, in parallel, on a 96-well glass-bottom imaging plate (for establishment of MOI) and a 24-well plate (for flow cytometry assessment). The next day, cells were infected with RSV (0.001 PFU per cell). For MOI establishment, following 6 h of infection, the cells plated on the imaging plate were fixed and subject to antibody staining for anti-RSV N and F and the number of infected cells (N^+/F^-) determined to obtain a MOI. For flow cytometry assessment, at 6 h, cells infected for flow cytometry assessment were treated with an RSV fusion inhibitor (TMC353121) to prevent subsequent infections. Flow cytometry assessment was carried out at 24 h and 48 h following viral inoculum addition. An hour before flow cytometry, infected cells (and uninfected control cells) were incubated with AbG-fluoro (1:1,000, in cell culture media) for 45 min at 37 °C. After antibody incubation, cells were rinsed in PBS, trypsinized, fixed (in suspension, with 4% paraformaldehyde for 10 min at room temperature with constant rotation) and suspended in PBS.

Flow cytometry analysis was performed using Cytoflex S (Beckman Coulter) and CytExpert software (see Supplementary Fig. 1). The percentage of successful infections in each cell line was calculated in relation to the fraction of infected cells at 6 h post-inoculum addition (MOI) to determine whether expression of the DARPin-P-fluoro reduced the efficiency of RSV infection success.

Microscopy

Microscope and image acquisition details. All fluorescence microscopy was carried out on a Nikon Ti2 inverted microscope equipped with a Yokogawa CSU-X1 spinning disc and a Prime 95B sCMOS camera (Photometrics), unless stated otherwise. Imaging was performed using a ×60/1.40 NA oil-immersion objective. Image acquisition was performed using NIS Elements software, making use of the 'perfect focus system' to correct for *Z* drift during timelapse imaging experiments. The microscope was equipped with a temperature-controlled incubator, and imaging for live-cell experiments was performed at 37 °C and for fixed-cell experiments at room temperature. For timelapse imaging experiments, *x*, *y* positions for imaging were randomly selected. Position selection was carried out immediately following viral inoculum addition and before observing foci in infected cells. Images were acquired every 5, 10, 20 or 30 min (exact intervals are recorded in the figure legends) for 6 h (short-term timelapse imaging) or 12–48 h (for overnight and longer-term timelapse imaging), using 50–70-ms exposure times (50 ms for the BFP channel and 70 ms for all other channels). Multiple *Z*-slices (approximately 9–15 slices with a 0.8-µm step size) were imaged for each channel, ensuring that the entirety of the cell was captured. For fixed cell analysis of immunofluorescence or smFISH staining, *x*, *y* positions for imaging were selected either randomly using the cell segmentation channel (when data regarding the frequency of a phenotype were assessed) or targeted using the channel of interest (when the frequency of a phenotype was not assessed). For smFISH staining in which the transgenic cell line DARPin-P-fluoro signal was acquired post-fixation, the same *x*, *y* positions are used to acquire the smFISH staining. Images were acquired at 45% laser power and 70-ms exposure (for all lasers) with a 0.8-µm step size and a *Z*-stack slice number that ensures the entirety of the cell is captured.

For high temporal resolution imaging of vRNP dynamics following RSV infection, real-time imaging was performed on a Nikon Ti2 inverted microscope equipped with a Yokogawa CSU-X1 spinning disk confocal unit and a Kinetix sCMOS LFOV camera (Photometrics). A Nikon Plan Apo λD ×60/1.42 NA oil-immersion objective was used. Excitation was provided by a 488-nm laser line (50% AOTF power) coupled with a 405/488/555/640/730 RPC-UF1 dichroic and a 525/50 emission filter. Timelapse acquisition was conducted for 4 h at a 10-s interval with the Ti2 perfect focus system engaged for *Z*-drift correction. Camera settings included 16-bit mode, no binning and 250-ms exposure time. The large 29.4-mm diagonal sensor of the Kinetix camera allowed an expanded field of view (approximately 320 µm × 320 µm), increasing imaging throughput. Fast *z*-stack acquisition was enabled using the NIDAQ Piezo. Image acquisition and hardware control were managed with NIS Elements software.

ExM datasets were acquired on a Zeiss LSM900 microscope equipped with an Airyscan2 detector using a ×63/1.3 NA objective. Images were collected in Multiplex SR-2Y mode as *z*-stacks with 0.120-µm spacing. Excitation was performed using 640-nm (20% laser power), 561-nm (2% laser power), 488-nm (30% laser power) and 405-nm (20% laser power) laser lines.

Post-acquisition data processing and video generation. Maximal intensity projections for all *Z*-slices (where multiple *Z*-slices were acquired) were generated using NIS Elements software (Nikon) and all downstream analyses were performed on these projections.

ExM image stacks were deconvolved in Huygens Professional (Scientific Volume Imaging, v20.10) using the classic maximum likelihood estimation algorithm with a theoretical point spread function (PSF), allowing up to 40 iterations.

The single-object-grid tool (https://github.com/TanenbaumLab/SingleObjectGrid) was used to crop a small field of view around tracked cells to create a stabilized time series with the cell centroid centred. The napari-animation plugin was used to generate video output from the napari viewer to create supplementary videos (https://napari.org/napari-animation/).

Quantification

Foci quantification. For all analyses, infected cells were manually identified by the presence of RSV vRNPs (as determined by the P^{exo} foci, anti-RSV N antibody staining or (−)vRNA smFISH staining). Only cells that were completely in the field of view were included in the analysis.

For fixed-cell analysis, infected cells were manually segmented in ImageJ, and foci detection and foci integrated intensity quantification were performed using the 'detect particles and colocalization analysis' function in the ComDet (v0.5.4) plugin in ImageJ (https://github.com/UU-cellbiology/ComDet). Plugin spot detection parameters were optimized for each type of foci analysed. The intensity thresholds used in the analyses were established for each individual experiment using the uninfected control samples. The specific parameters used were: smFISH viral N mRNA spot detection; approximate particle size of 3 µm, intensity threshold range of 15–30 or more (that is, 15–30 times or more the signal-to-noise ratio), large particles not included; smFISH viral genome and antigenome spot detection; approximate particle size of 4 µm, intensity threshold range of 5–50 or more, large particles included; transgenic cell line-derived and antibody staining-derived RSV vRNP spot detection; approximate particle size of 4 µm, and intensity threshold range of 5–200 or more, large particles included. For individual vRNP spot detection (including smFISH, transgenic cell line and antibody staining-derived foci), an additional filtering step was introduced, in which only spots that had an N area value > 6 and value < 30 (pixels in foci) were included in the analysis. Intensity-based cut-offs for each channel were used to call colocalization. These cut-off values were established for each individual experiment using both the uninfected control sample and the individual channel of interest. The lowest intensity where a foci was detected (individual channel of interest) above background was used as the intensity cut-off to call positive and negative values. Foci integrated intensity values (sum of all pixels intensities inside the segmented spot area minus the average spot-specific backgrounds). Background value, calculated as the average intensity of pixels along the perimeter of a bounding rectangle surrounding the segmented spot, of less than 0 was converted to 0 to aid with analysis and data visualization. Integrated intensity values were normalized (to the median value of DARPin-P^- foci, or to the maximum intensity value) to allow for optimal data comparison. For antibody staining experiments, only genomes that were N^+/F^- were considered to be inside cells. If the P^{exo}-fluoro transgenic cell line was utilized, only P^{exo+} foci were considered to be vRNPs inside infected cells.

Quantification of the number of foci per virion was carried out manually. P^{exo}-fluoro cells were infected with an inoculum containing RSV (low MOI, exact value recorded in figure legends) and either the viral polymerase inhibitor PC786 or the translation inhibitor emetine to prevent infection progression. If timelapse data were acquired, imaging was started immediately following inoculum addition. The start of infection was defined as the first time point a P^{exo}-fluoro foci was observed. Only cells in which a minimum of two time points before viral entry were observed were included in the analysis. Foci number was determined for each time point until the end of the acquisition. Only cells that remained completely within the field of view for the entire duration of analysis were included. In addition, only infected cells in which minimally 10 h of infection was observed were used for downstream analysis. In cases in which foci number per virion was assessed at a fixed time point, 1 h after inoculum addition, the fusion inhibitor

TMC353121 was added to prevent subsequent infections. Three hours after fusion inhibitor addition (4 h post-inoculum addition), the cells were imaged. The number of foci in each infected cell was quantified.

Quantification of the time foci appeared and the number of foci present at each time frame in live-cell timelapse imaging videos was carried out manually. Only cells that remained completely within the field of view for the entire duration of the analysis were included. For experiments in which infection was followed from the moment of viral cell entry, only cells in which a minimum of two time frames before viral entry were observed were included. For vRNP analysis, only foci that were present for a minimal of two consecutive time frames were considered in the analysis to minimize false foci calling. For assessing the DARPin-P state, infections were classified as DARPin-P^+ if one or more of the infecting vRNPs were DARPin-P^+ even if the cell additionally had DARPin-P^- vRNPs. Quantification of the number of translating viral reporter mRNAs per cell (infection with the upstream and downstream $SunTag^{eng}$ RSV strains) was performed, based on previously described guidelines[16]. In brief, the number of translation sites at each individual time frame were assessed until individual translation sites could no longer be detected (high translation rate leading to the depletion of free cellular STAb due to the cytoplasmic accumulation of mature SunTag peptides)[53]. AbG-fluoro signal accumulation was also assessed manually and recorded at the first time frame positivity could be observed. Foci calling (P^{exo} and DARPin-P signal for vRNPs and translation sites for the $SunTag^{eng}$ RSV downstream engineered strain) and AbG-fluoro accumulation calling were independently validated by another laboratory member. If intensity quantification of foci in timelapse videos was performed, the cell of interest was manually segmented at each time point and foci intensity quantified using the ComDet plugin. To facilitate visual inspection of general trends in heterogenous intensity values over time (for individually tracked foci), moving averages were plotted with a sliding window of three time points.

Quantification of viral transcription rate. As the number of translating SunTag mRNAs closely correlated with the number SunTag mRNAs (Extended Data Fig. 7f), the increase in the number of translating SunTag mRNAs over time was used as a proxy to calculate viral transcription rate. The number of viral mRNA translation sites within a 1-h period as initial observation was plotted against time. Graphs for individual infections were fit with a linear function using GraphPad prism (v10.1.0) and the slope of this function was used as the viral transcription rate.

Quantification of ExM datasets. Quantification was performed using Imaris software (Bitplane v9.7.2). vRNPs were segmented based on the polyclonal-RSV P antibody signal using the Surface function with a grain size of 100 nm and background subtraction (maximum sphere diameter of 300 nm). All images within the same experiment were processed using identical threshold values, and background surfaces were defined from the inverse portion of the intensity histogram. The mean DARPin-P intensity per segmented vRNP was corrected by subtracting the corresponding background mean and subsequently normalized to the average intensity across all particles from the same experiment. A cut-off value of 0.3 was applied to classify viral particles as DARPin-P^+ or DARPin-P^- (Extended Data Fig. 8a). Particle size was defined as the length of the longest axis of the bounding box aligned to the object. Statistical analyses were performed using Prism 10 (GraphPad Software).

Proteomic quantitative analysis. Protein and phospho-site identification and quantification were performed using Andromeda search engine implemented in MaxQuant (v2.3.0)[83]. Spectra were searched against human proteomes downloaded from Uniprot (on 22 August 2022), RSV custom proteome derived from human RSV subgroup A, strain Long (GenBank accession: AY911262) and DARPin-P sequence. False discovery rate was set at 1% for both peptide and protein identification. MaxQuant search was performed with 'match between run' activated in the searches. Phosphorylation on STY residues was set as a variable modification in addition to protein N-terminal acetylation and methionine oxidation. All other parameters were set to default values. MaxQuant (proteinGroups) outputs were used for downstream relative quantification analysis. Proteins highlighted as potential contaminant and reverse were filtered out. R-package limma (v3.52.4)[84] was used for statistical analysis for protein intensities, applying a moderated *t*-test, with *P* values adjusted for multiple testing using Benjamini–Hochberg methodology.

Statistical analysis

All statistical analyses performed using GraphPad prism (v10.1.0, GraphPad Software) and Microsoft Excel. Unless stated otherwise, statistical tests were performed using a *P* value of 0.05 as a cut-off for significance and assuming normal distribution of experimentally determined averages. The type of test and the type of error bars used in figures are indicated in the figure legend or in the figure itself. The *n* values are recorded in the figures and included in Supplementary Table 1. In addition, Supplementary Table 1 presents an overview of the number of experimental repeats, the total number and type of observations per condition, as well as situations in which the same raw data have been used for multiple independent analyses. Graph creation was also performed in GraphPad.

Material availability

Further information and requests for resources and reagents should be directed to and will be fulfilled by the lead contact M.E.T. (m.tanenbaum@hubrecht.eu). The unique or stable reagents generated in this study are available from the lead contact with a completed Material Transfer Agreement. The plasmids generated in this study for the vRNP visualization tools (P^{exo}–SunTag, P^{exo}–ALFATag, M2-1^{exo}–SunTag, N^{exo}–SunTag and DARPin-P–BFP) have been deposited in Addgene.

Reporting summary

Further information on research design is available in the Nature Portfolio Reporting Summary linked to this article.

Data availability

A selection of raw imaging data that support the findings of this study are openly available (https://doi.org/10.6084/m9.figshare.28269707). The nucleotide sequences for the following RSV strains used in this study are publicly available in GenBank under the accession numbers AY911262.1 (strain Long), FJ948820 (RSV-98-25147-X) and JQ901457.1 (03-036465). Chemical shift assignments for ^{15}N-P_{CTD} are available in the Biological Magnetic Resonance Bank under accession number 26906. The mass spectrometry proteomics data have been deposited to the ProteomeXchange Consortium via the PRIDE[85] partner repository with the dataset identifier PXD070991 (https://doi.org/10.6019/PXD070991).

Code availability

No custom code was used to generate or process the data described in this article.

55. Buchholz, U. J., Finke, S. & Conzelmann, K.-K. Generation of bovine respiratory syncytial virus (BRSV) from cDNA: BRSV NS2 is not essential for virus replication in tissue culture, and the human RSV leader region acts as a functional BRSV genome promoter. *J. Virol.* **73**, 251–259 (1999).
56. Ekanger, C. T. et al. Comparison of air-liquid interface transwell and airway organoid models for human respiratory virus infection studies. *Front. Immunol.* **16**, 1532144 (2025).
57. Terstappen, J. et al. Intranasal monoclonal antibodies do not prevent respiratory infection in a randomized, controlled experimental infection trial. *npj Drug Discov.* **2**, 15 (2025).
58. Kim, Y.-I. et al. Respiratory syncytial virus human experimental infection model: provenance, production, and sequence of low-passaged memphis-37 challenge virus. *PLoS ONE* **9**, e113100 (2014).

59. Pereira, N. et al. New insights into structural disorder in human respiratory syncytial virus phosphoprotein and implications for binding of protein partners. *J. Biol. Chem.* **292**, 2120–2131 (2017).
60. Dreier, B. & Plückthun, A. in *Ribosome Display and Related Technologies: Methods and Protocols* 1st edn (eds Douthwaite, J. A. & Jackson, R. H.) 261–286 (Springer, 2011).
61. Binz, H. K., Stumpp, M. T., Forrer, P., Amstutz, P. & Plückthun, A. Designing repeat proteins: well-expressed, soluble and stable proteins from combinatorial libraries of consensus ankyrin repeat proteins. *J. Mol. Biol.* **332**, 489–503 (2003).
62. Kramer, M. A., Wetzel, S. K., Plückthun, A., Mittl, P. R. & Grütter, M. G. Structural determinants for improved stability of designed ankyrin repeat proteins with a redesigned C-capping module. *J. Mol. Biol.* **404**, 381–391 (2010).
63. Brauchle, M. et al. Protein interference applications in cellular and developmental biology using DARPins that recognize GFP and mCherry. *Biol. Open* **3**, 1252–1261 (2014).
64. Schilling, J., Schöppe, J. & Plückthun, A. From DARPins to LoopDARPins: novel LoopDARPin design allows the selection of low picomolar binders in a single round of ribosome display. *J. Mol. Biol.* **426**, 691–721 (2014).
65. Zahnd, C., Sarkar, C. A. & Plückthun, A. Computational analysis of off-rate selection experiments to optimize affinity maturation by directed evolution. *Protein Eng. Des. Sel.* **23**, 175–184 (2010).
66. Campbell, B. F., Dittmann, A., Dreier, B., Plückthun, A. & Tyagarajan, S. K. A DARPin-based molecular toolset to probe gephyrin and inhibitory synapse biology. *eLife* **11**, e80895 (2022).
67. Simon, M., Zangemeister-Wittke, U. & Plückthun, A. Facile double-functionalization of designed ankyrin repeat proteins using click and thiol chemistries. *Bioconjug. Chem.* **23**, 279–286 (2012).
68. Hughes, C. S. et al. Single-pot, solid-phase-enhanced sample preparation for proteomics experiments. *Nat. Protoc.* **14**, 68–85 (2019).
69. Skinner, S. P. et al. CcpNmr AnalysisAssign: a flexible platform for integrated NMR analysis. *J. Biomol. NMR* **66**, 111–124 (2016).
70. Gonnin, L. et al. Importance of RNA length for in vitro encapsidation by the nucleoprotein of human respiratory syncytial virus. *J. Biol. Chem.* **298**, 102337 (2022).
71. Tan, L. et al. Genetic variability among complete human respiratory syncytial virus subgroup A genomes: bridging molecular evolutionary dynamics and epidemiology. *PLoS ONE* **7**, e51439 (2012).
72. Fix, J., Galloux, M., Blondot, M.-L. & Eléouët, J.-F. The insertion of fluorescent proteins in a variable region of respiratory syncytial virus L polymerase results in fluorescent and functional enzymes but with reduced activities. *Open Virol. J.* **5**, 103–108 (2011).
73. Blanchard, E. L. et al. Polymerase-tagged respiratory syncytial virus reveals a dynamic rearrangement of the ribonucleocapsid complex during infection. *PLoS Pathog.* **16**, e1008987 (2020).
74. Thi Nhu Thao, T. et al. Rapid reconstruction of SARS-CoV-2 using a synthetic genomics platform. *Nature* **582**, 561–565 (2020).
75. Gibson, D. G. et al. Creation of a bacterial cell controlled by a chemically synthesized genome. *Science* **329**, 52–56 (2010).
76. Kouprina, N., Noskov, V. N. & Larionov, V. Selective isolation of large segments from individual microbial genomes and environmental DNA samples using transformation-associated recombination cloning in yeast. *Nat. Protoc.* **15**, 734–749 (2020).
77. Bouillier, C. et al. Generation, amplification, and titration of recombinant respiratory syncytial viruses. *J. Vis. Exp.* https://doi.org/10.3791/59218 (2019).
78. Jin, H. et al. Recombinant human respiratory syncytial virus (RSV) from cDNA and construction of subgroup A and B chimeric RSV. *Virology* **251**, 206–214 (1998).
79. Grimm, J. B. et al. A general method to improve fluorophores using deuterated auxochromes. *JACS Au* **1**, 690–696 (2021).
80. Castagne, N. et al. Biochemical characterization of the respiratory syncytial virus P–P and P–N protein complexes and localization of the P protein oligomerization domain. *J. Gen. Virol.* **85**, 1643–1653 (2004).
81. Gaspar, I., Wippich, F. & Ephrussi, A. Terminal deoxynucleotidyl transferase mediated production of labeled probes for single-molecule FISH or RNA capture. *Bio Protoc.* **8**, e2750 (2018).
82. Lyubimova, A. et al. Single-molecule mRNA detection and counting in mammalian tissue. *Nat. Protoc.* **8**, 1743–1758 (2013).
83. Cox, J. & Mann, M. MaxQuant enables high peptide identification rates, individualized ppb-range mass accuracies and proteome-wide protein quantification. *Nat. Biotechnol.* **26**, 1367–1372 (2008).
84. Ritchie, M. E. et al. limma powers differential expression analyses for RNA-sequencing and microarray studies. *Nucleic Acids Res.* **43**, e47 (2015).
85. Perez-Riverol, Y. et al. The PRIDE database at 20 years: 2025 update. *Nucleic Acids Res.* **53**, D543–D553 (2025).
86. Tran, T.-L. et al. The nine C-terminal amino acids of the respiratory syncytial virus protein P are necessary and sufficient for binding to ribonucleoprotein complexes in which six ribonucleotides are contacted per N protein protomer. *J. Gen. Virol.* **88**, 196–206 (2007).
87. Abramson, J. et al. Accurate structure prediction of biomolecular interactions with AlphaFold 3. *Nature* **630**, 493–500 (2024).
88. Gilman, M. S. et al. Structure of the respiratory syncytial virus polymerase complex. *Cell* **179**, 193–204.e14 (2019).

Acknowledgements We thank B. Verhagen for help with cell line establishment; J. Schokolowski for help with independent validation of timelapse analysis; H. J. Hamstra for plasmid generation and primary rescue of the P-ALFA-Tag and L-HaloTag RSV strains; M. C. Viveen and F. Coenjaerts for providing RSV clinical isolates; M. Müller for discussions on the viral labelling strategy; L. Lavis for the HaloTag ligands; S. Vashee for providing the TAR vector; N. Kouprina for providing the yeast strain; V. Thiel for help with the TAR cloning protocol; the Hubrecht Institute flow cytometry core facility for facilitating cell sorting; members of the Tanenbaum laboratory, Bont laboratory and L. Meyaard for discussions; and J. Schuijers for comments on the manuscript. This work was financially supported by the European Union (ERC; VirIm, 101044794), an NWO M-Invest grant (OCENW.M.22.397), the Howard Hughes Medical Institute through an international research scholar grant to M.E.T. (HHMI/IRS 55008747) and an EMBO Postdoctoral Fellowship to D.R. (ALTF 102-2021). D.R., S.B., L.A., M.J.D.B., R.B. and M.E.T. were supported by the Oncode Institute, which is partly funded by the Dutch Cancer Society (KWF). A.J.L., A.T.G. and P.B.v.K were financially supported by the Dutch Ministry of Health, Welfare and Sport. Y.D. and S.M. were supported by the EPSRC (V011359/1 (P)). A.C. is funded by the ERC Consolidator Grant 'vRNP-capture' 101001634 and the Medical Research Council grants MR/R021562/1 and MC_UU_00034/2. Although this work is funded by the European Union, the views and opinions expressed are, however, those of the authors only and do not necessarily reflect those of the European Union or the ERC Executive Agency. Neither the European Union nor the granting authority can be held responsible for them.

Author contributions D.R., S.B. and M.E.T. conceptualized the study and conducted the methodology. D.R., M.G., S.B., M.N., C. Sizun, C. Sacristan, J.S., A.J.L., A.T.G., B.D., S.F., L.A., R.B. and Y.D. performed the investigation. D.R., M.G., S.B., M.N., C. Sizun, C. Sacristan, J.S., A.J.L. and M.J.D.B. conducted formal analysis. D.R. and S.B. performed validation. D.R., M.G., S.B., M.N., C. Sizun, C. Sacristan, J.S. and A.J.L. performed visualization. M.G., B.D., S.F., N.I.M., L.J.B., S.M., A.P., J.-F.É., G.J.P.L.K., A.C., P.B.v.K., M.-A.R.-W. and M.E.T. provided resources. D.R. and M.E.T. wrote the original draft of the manuscript. All authors reviewed and edited the manuscript. M.G., L.J.B., S.M., A.P., J.-F.É., G.J.P.L.K., A.C., P.B.v.K. and M.E.T. supervised the study. D.R., M.G., C. Sizun., S.M., A.P., J.-F.É., G.J.P.L.K., A.C., P.B.v.K. and M.E.T. acquired funding.

Competing interests N.I.M. has received support for attending meetings and/or travel from the ResViNET Foundation. UMC Utrecht has received grants from AbbVie, AstraZeneca, The Bill & Melinda Gates Foundation, the Dutch Lung Foundation, The Gates Medical Research Institute, GSK, Janssen, MedImmune, MeMed, Merck, Novavax, Pfizer and Sanofi; has received payment or honoraria for lectures, presentations, speakers bureaus, manuscript writing or educational events from AbbVie, Ablynx, AstraZeneca, Bavaria Nordic, GSK, Janssen, MabXience, MedImmune, MEDtalks, Merck, Moderna, Novavax, Pfizer, Sanofi and Virology Education. L.J.B. is the founding chairman of the ReSViNET Foundation. All other authors declare no competing interests.

Additional information
Supplementary information The online version contains supplementary material available at https://doi.org/10.1038/s41586-025-10071-5.
Correspondence and requests for materials should be addressed to Marvin E. Tanenbaum.
Peer review information *Nature* thanks Dalan Bailey, Alexander Borodavka and Mingzhou Chen for their contribution to the peer review of this work.
Reprints and permissions information is available at http://www.nature.com/reprints.

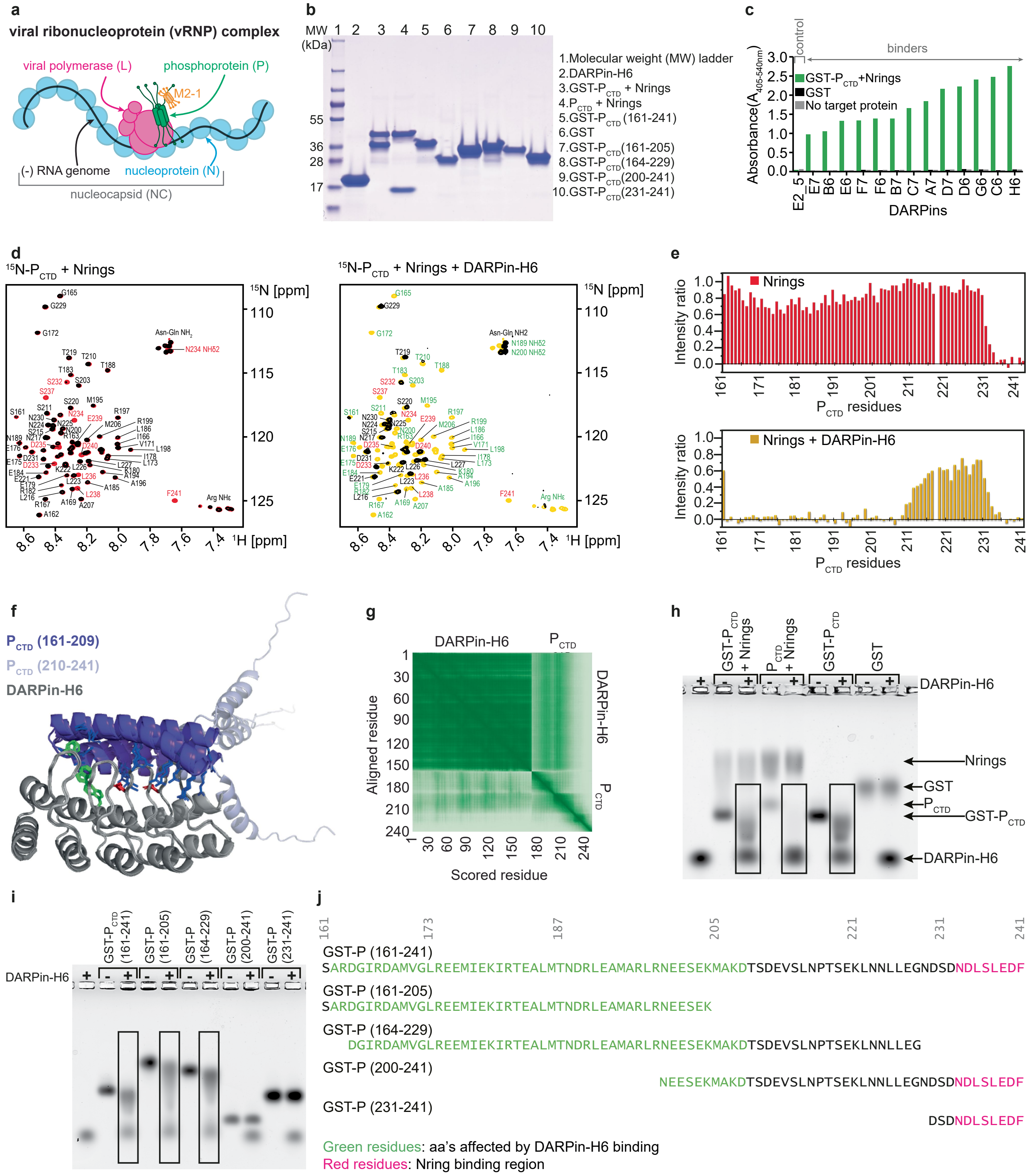

Extended Data Fig. 1 | See next page for caption.

Extended Data Fig. 1 | Identification and in vitro characterization of a DARPin that binds RSV P. a, Schematic of RSV viral ribonucleoprotein (vRNP) complex. **b**, SDS-PAGE and Coomassie blue staining of purified DARPin-H6, P_{CTD}+Nring protein complex and tags used as a target for DARPin selection and P_{CTD} fragments. The first lane shows the molecular weight ladder. **c**, DARPins that bind RSV vRNPs were identified via ribosome display. ELISA measurements show specific binding of different DARPins to the target protein complex. The absorbance for 13 target binding DARPins and a non-binding control DARPin (DARPin E2_5)[61] (green bars) is shown. GST (black bars) and no target (grey bars) were used as controls. DARPin-H6 was selected for further characterization. **d, e**, 2D NMR spectra of RSV ^{15}N-P_{CTD} in the presence of DARPin-H6 and Nrings. (**d**) ^{1}H-^{15}N HSQC spectra of 50 µM ^{15}N-P_{CTD} were measured before and after addition of 1 molar equivalent of RSV Nrings, and after addition of 1 molar equivalent of each RSV Nrings and DARPin-H6. The spectra with added Nring (in red) and Nring+DARPin-H6 (in yellow) were superimposed on the spectrum of ^{15}N- P_{CTD} alone (in black). Assignments of signals that were fully broadened out due to addition of Nrings and DARPin-H6 are indicated in red and green, respectively. Other assignments are in black. (**e**) Backbone amide signal intensities in ^{1}H-^{15}N HSQC spectra of ^{15}N-P_{CTD} were measured for each residue, except proline 218, in the presence of 1 molar equivalent of RSV Nrings, or both RSV Nrings and DARPin-H6, as well as for ^{15}N-P_{CTD} alone. The bar diagrams represent the intensities measured in the presence of interaction partners divided by the intensities of the reference spectrum (intensity ratio). Addition of Nrings to P_{CTD} resulted in broadening of the backbone amide signals corresponding to the last 10 residues at the C-terminal end of the P_{CTD}, amino acids that were previously identified as an Nring binding region[59,86]. When RSV Nrings were added to the DARPin-H6–P_{CTD} complex, the spectral perturbations observed for the ternary mixture were the sum of individual perturbations induced by DARPin-H6 and Nrings (see also Fig. 1b**, c**), indicating that DARPin-H6 binds to P_{CTD} alone and P_{CTD} in complex with Nrings in a similar manner. **f, g**, AlphaFold3 (ref. 87) (AF3) prediction of the DARPin-H6:RSV P_{CTD} complex (https://alphafoldserver.com/, accessed on 5 December 2024). The 40 residue P_{CTD} region identified as the DARPin-H6 binding region is larger compared to the size of DARPin-H6. It would span 65 Å if it formed a single extended α-helix. This is twice the distance between the first and the fourth loop of the variable region of DARPin-H6, and suggests that the P_{CTD} region takes on a compact, folded conformation in the P_{CTD}+DARPin-H6 complex. The NMR data strongly suggests that tumbling of the P_{CTD} (aa 162-209) region is slowed down due to binding DARPin-H6, implying that this region of the P_{CTD} is indeed folded or structured in the DARPin-H6 – P_{CTD} complex. Previous studies have identified two transient α-helices, α_{C1} and α_{C2}, in the largely unstructured CTD of RSV P by NMR[59], and the P_{CTD} has been shown to also adopt a structured conformation when in complex with L[88], consistent with our data that this region can adopt a structured conformation. AF3 was used to predict the potential structure of the DARPin-H6 – P_{CTD} complex. The protein query sequences were DARPin-H6 and P_{CTD} (aa 161-241). (**f**) Superimposition of the 4 best ranked complex models, with DARPin-H6 in grey, P_{CTD} aa 161-209 in purple, and P_{CTD} aa 210-241 residues in light blue. Protein structures were visualized with Pymol (Schrodinger, 2010, https://pymol.org/). P arginine side chains are shown in blue sticks. DARPin-H6 residues that interact with P arginines are in sticks (acidic residues - red, aromatic residues - green). The models generated predicted that the 50 N-terminal residues of the P_{CTD} formed two parallel helices that interact with the variable region of DARPin-H6. (**g**) Predicted aligned error (PAE) matrix of the AF3 prediction (color code for expected position error: 0 to 30 Å from dark green to white). **h**, DARPin-H6 interacts with RSV P, both in its free and Nring bound form. DARPin-H6 was co-incubated with the P_{CTD}+Nrings target protein complex or its individual components (including tags) and interactions were assessed by band shift on native agarose gel. Boxes indicate lanes where interactions are observed. **i, j**, NMR-identified DARPin-H6 interaction region on RSV P was further validated by assessing complex formation of DARPin-H6 with fragments of the P_{CTD}. (**i**) Complex formation was visualized by band shift on native agarose gel. Boxes indicate lanes showing complexes. (**j**) The amino acid sequence of the P_{CTD} and its fragments are shown. P_{CTD} residues identified to interact with DARPin-H6 by NMR are in green and Nring binding residues are in magenta. (**h, i**) Gel shift assays were independently repeated three times with similar results, and a representative native agarose gel image is shown.

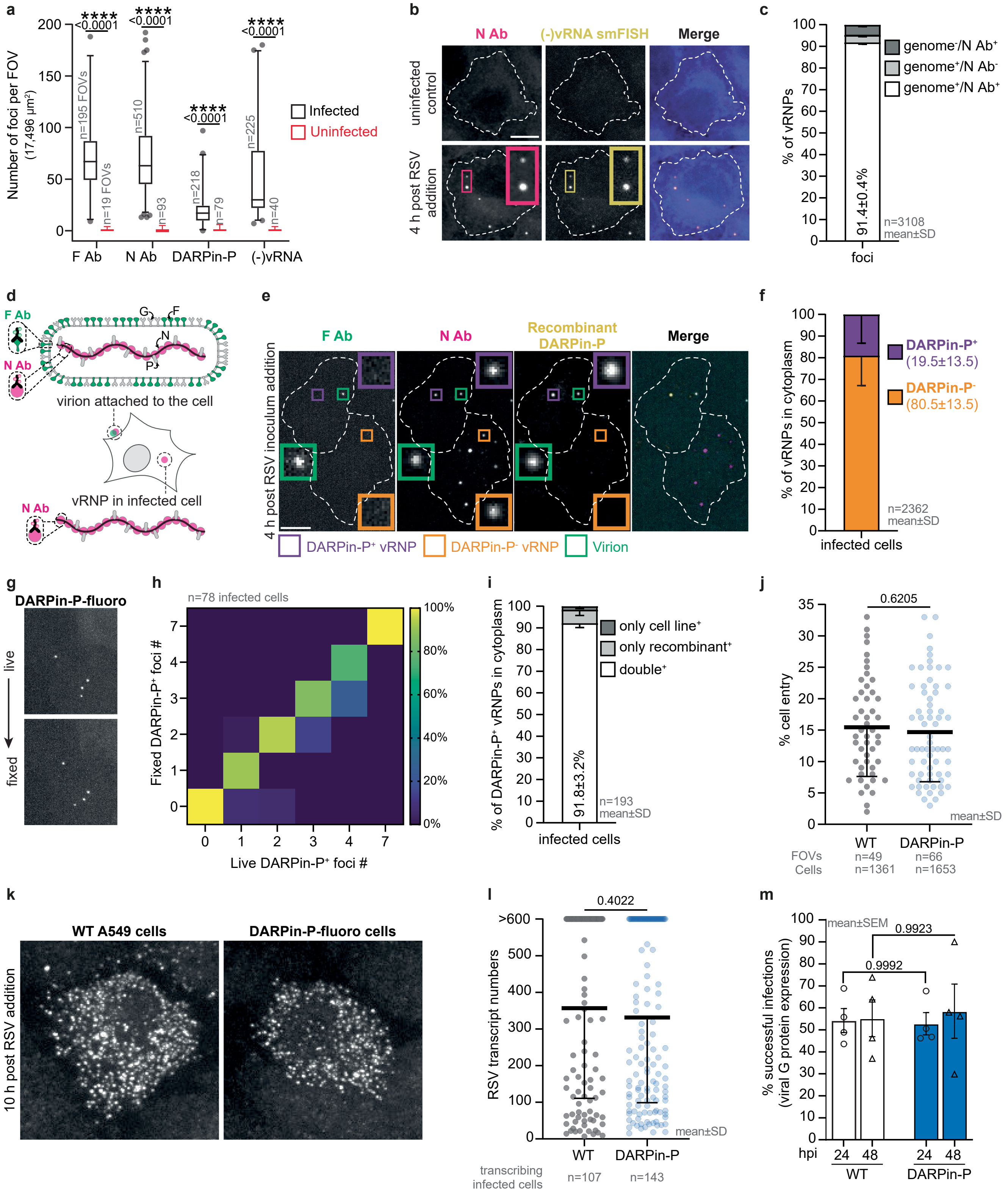

Extended Data Fig. 2 | See next page for caption.

Extended Data Fig. 2 | DARPin-P labels a subset of vRNPs in infected cells. **a**, Quantification of the false-positive foci detection for indicated antibodies, recombinant DARPin-P protein and RSV genome smFISH probe set used to detect RSV vRNPs and virions. Data are shown as a box and whiskers plots, with the box extending from the 25th to 75th percentiles, the center line indicating the median, and whiskers spanning the 1st to 99th percentiles representing the minima and maxima. **b, c**, RSV N antibody staining identifies RSV vRNPs. N antibody foci in infected cells colocalize with RSV genomic RNA ((-)vRNA). Representative images (**b**) and quantification of colocalization (**c**). **d**, Schematic highlighting dual antibody staining-based approach for distinguishing RSV vRNPs in virions (N^+/F^+) and in the cytoplasm of infected cells (N^+/F^-). **e**, Representative images of RSV infected WT A549 cells stained for RSV F, N and recombinant DARPin-P. The green insert highlights a virion attached to the cell while the orange and purple inserts highlight DARPin-P^- and DARPin-P^+ vRNPs in the infected host cell cytoplasm, respectively. **f**, For cytoplasmic vRNPs (F^-), the DARPin-P state was determined and quantified. Note that the analysis was performed at 4 h post RSV inoculum addition to ensure mostly single vRNPs were analyzed (see Fig. 2j). **g, h**, The effect of paraformaldehyde fixation on DARPin-P-fluoro foci observed following RSV infection was assessed. (**g**) Representative images of the same cells imaged live and after fixation. (**h**) Heat map visualizes the frequency of the number of DARPin-P-fluoro foci observed by live imaging and imaging following fixation, in the same cells. **i**, Quantification of the colocalization between DARPin-P signal from genetically-encoded DARPin-P-fluoro and recombinant DARPin-P signal of RSV vRNPs in infected DARPin-P-fluoro cells (related to Fig. 1f). **j, k, l**, RSV infection in the DARPin-P-fluoro cell line was comparable to that in WT A549 cells. (**j**) Quantification of the fraction of infected cells at 6 h post viral inoculum addition for DARPin-P-fluoro and WT A549 cells. Representative images (**k**) and quantification (**l**) of viral mRNA transcripts (using a smFISH probe set for all RSV mRNAs) in infected DARPin-P-fluoro and WT A549 cells at 10 h post viral inoculum addition. **m**, Flow cytometry-based quantification of the percentage of infected cells expressing viral G protein (a read-out of successful infections, see Extended Data Fig. 5j–p and Supplementary Fig. 1) at 24 and 48 h post viral inoculum addition for DARPin-P-fluoro and WT A549 cells. (**a, m**) Two-way ANOVA with Tukey's multiple comparisons test used for statistical analysis. (**j, l**) Two-tailed unpaired Student's t-test was used for statistical analysis. (**b, e, g, k**) Scale bar, 10 µm. The number of experimental repeats and fluorophores used are listed in Supplementary Table 1.

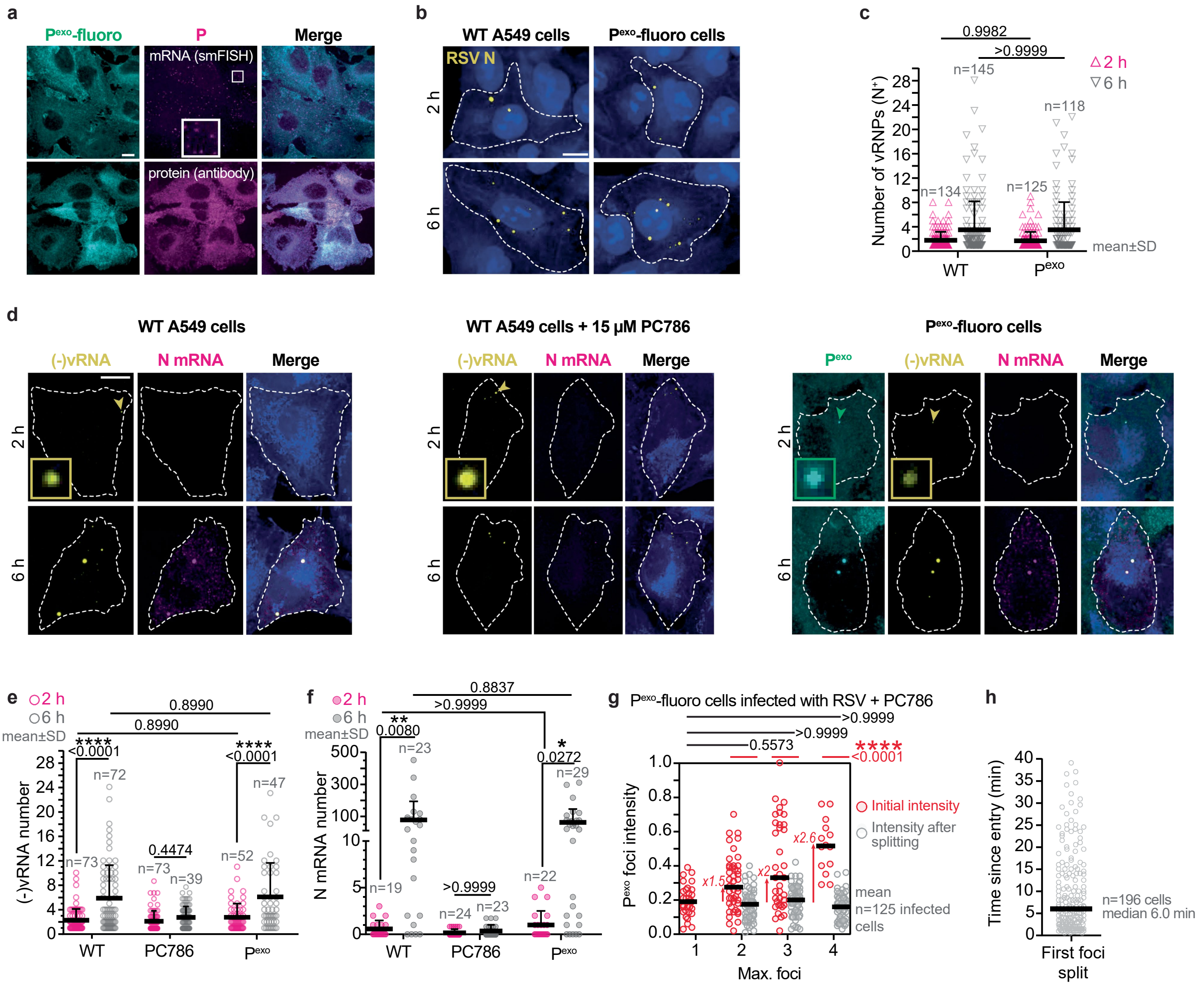

Extended Data Fig. 3 | Validation of the P^exo^-fluoro cell line and RSV polymerase inhibitor, PC786. a, The P^{exo}-fluoro cell line expresses low levels of RSV P-SunTag and fluorescently-tagged STAb. Representative images show the levels of P mRNA (via smFISH using a probe set for P) and protein (anti-RSV P antibody) in the cell line. **b, c**, RSV infection in the P^{exo}-fluoro cell line was compared to that in WT A549 cells at 2 and 6 h post viral inoculum addition by antibody staining for vRNPs (anti-RSV N antibody). Representative images (**b**) and quantification of the number of vRNPs per cell (**c**) is shown. **d, e, f**, RSV infection in the P^{exo}-fluoro cell line, WT A549 cells and in the presence of the RSV polymerase inhibitor, PC786, was assessed at 2 and 6 h post viral inoculum addition by smFISH staining towards the RSV genome and N transcripts. (**d**) Representative images are shown. Quantification of the (-)vRNA (**e**) and N mRNA (**f**) levels. **g**, Characterization of RSV vRNP separation after host cell entry observed for cells infected with virions containing 1-4 vRNPs. PC786 was added to all cells to ensure increases in vRNP number are caused by splitting of incoming vRNPs and not a consequence of genome replication. Foci intensities of P^{exo}-fluoro for the foci before splitting (red) and individual foci intensities after reaching the maximum foci number after splitting (grey). Each data point is an individual foci. **h**, High-time resolution imaging (10 sec interval) captured transient cytoplasmic co-localization of incoming vRNPs from the same virion in P^{exo}-fluoro cells. Cell were supplemented with PC786 to prevent infection progression. For virions carrying multiple vRNPs, the time interval from entry to initial vRNP separation was quantified. See also Supplementary Video 2. (**c, e, f, g**) Two-way ANOVA with Tukey's multiple comparisons test used for statistical analysis. (**a, b, d**) Scale bar, 10 µm. The number of experimental repeats and fluorophores used are listed in Supplementary Table 1.

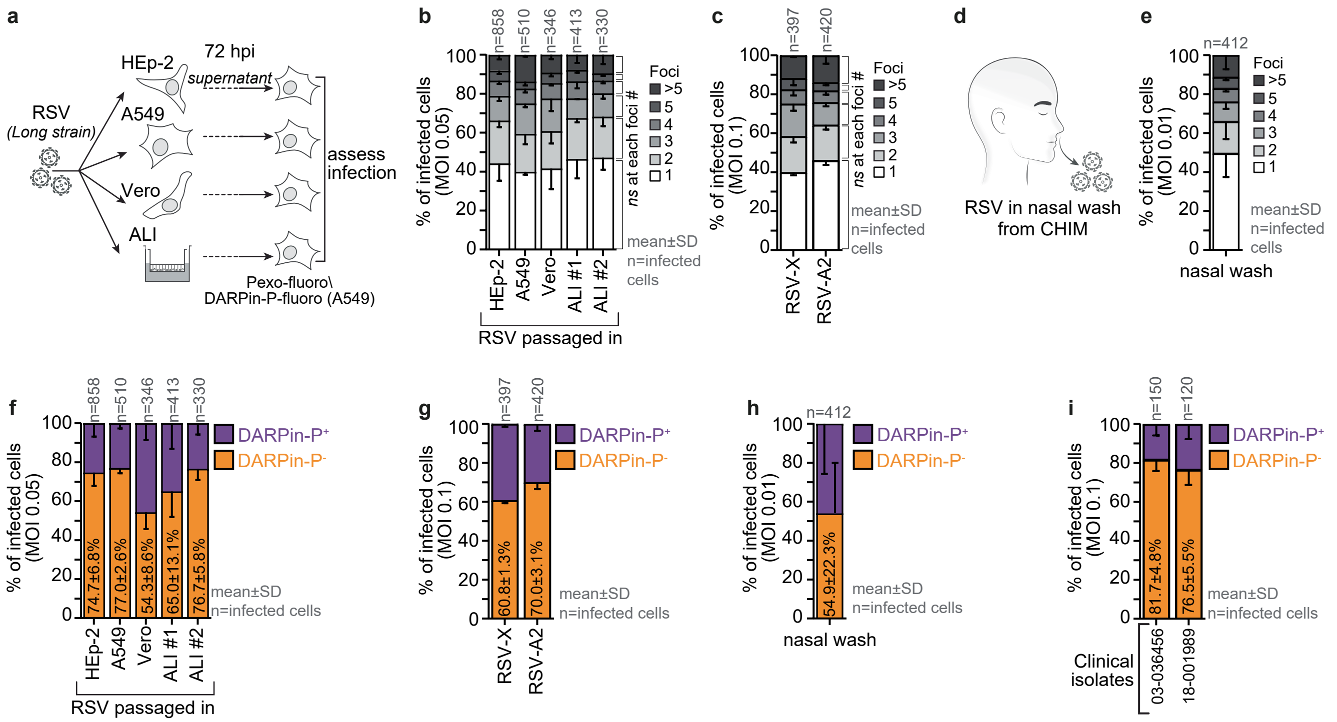

Extended Data Fig. 4 | Heterogeneity of RSV virions from different viral strains and origins. RSV virion heterogeneity, with respect to the number of vRNPs and their DARPin-P state was assessed. To study individual virions, A549 cells expressing P^{exo}-fluoro and DARPin-P-fluoro were infected at low MOI (0.01-0.1) to ensure that the majority of cells were infected with a single virion. In all analyses, all vRNPs in the same infected cell was considered to originate from a single virion. Analysis was carried out at 4 hpi to ensure all vRNPs from individually infecting virions had split. **a, b**, RSV Long strain was passaged once in HEp-2, A549 and Vero cell lines as well as in air-liquid-interface (ALI) cultures of primary human nasal epithelium obtained from 2 healthy donors. Virions of these different cellular origins were assessed. Schematic summarizing experimental protocol (**a**) and quantification of vRNP numbers (**b**). **c**, Two RSV strains, RSV-X and RSV-A2, were evaluated. The number of vRNPs per virion were quantified. **d, e**, RSV virions present in nasal wash samples of RSV-infected individuals was assessed. The samples were obtained from participants of a controlled human infection (CHIM) study, where healthy adults were inoculated with the challenge strain RSV-A Memphis-37 (refs. 57,58). Schematic (**d**) and quantification of vRNP numbers per virion (**e**) is shown. **f**, The DARPin-P state of virions produced in different cell lines and primary cells (see Extended Data Fig. 4a) is quantified. **g**, The DARPin-P state of virions from RSV-X and RSV-A2 is quantified. **h**, The DARPin-P state of virions from nasal wash samples (see Extended Data Fig. 4d) is quantified. **i**, The DARPin-P state of virions from two RSV clinical isolates is quantified. (**b, c**) Two-way ANOVA with Tukey's multiple comparisons test compared if there was significant variation of the frequencies between different samples for each of the foci numbers. The number of experimental repeats and fluorophores used are listed in Supplementary Table 1.

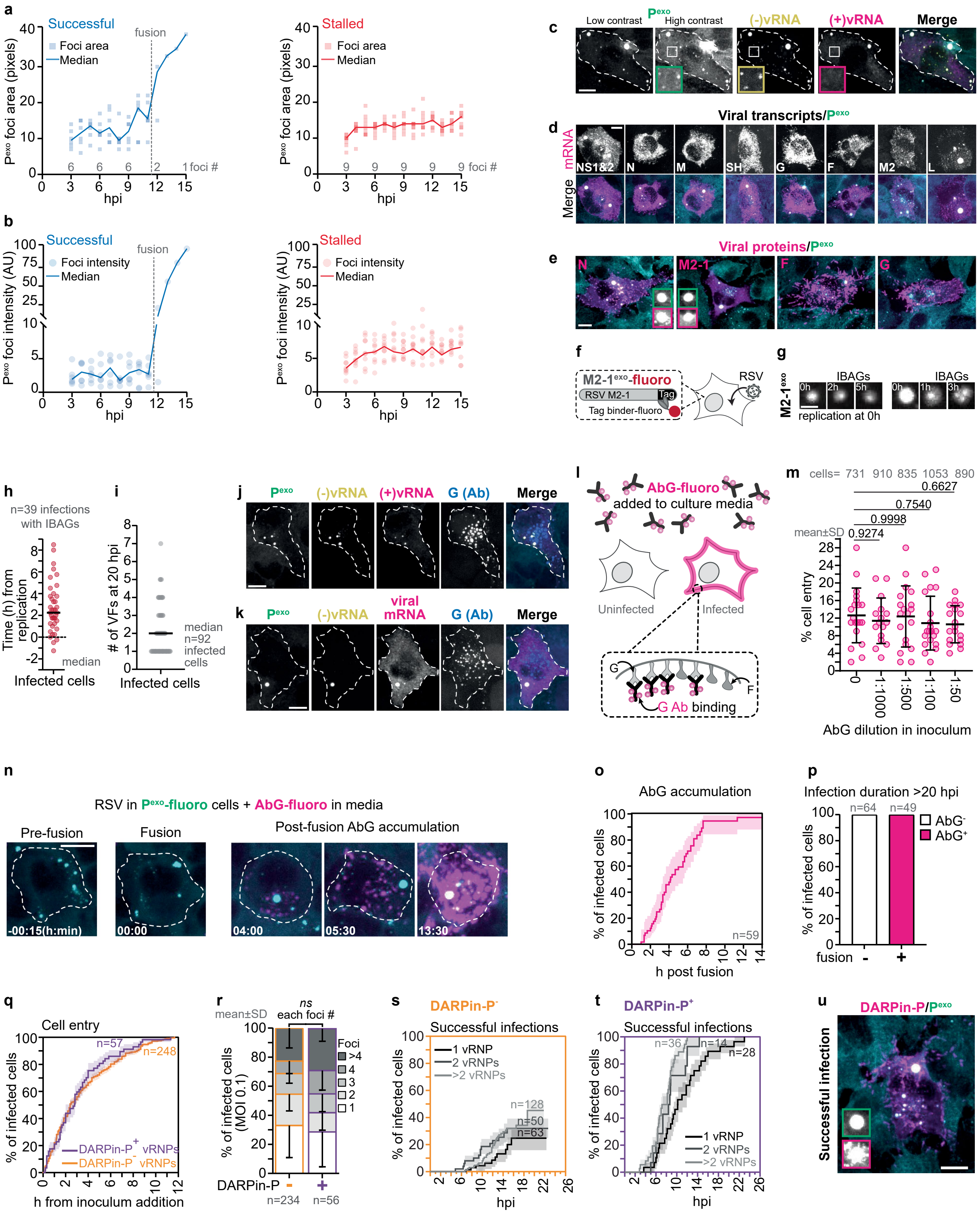

Extended Data Fig. 5 | See next page for caption.

Extended Data Fig. 5 | DARPin-P$^+$ vRNPs give rise to successful infections. **a, b**, WT RSV infections in P^{exo}-fluoro cells were further characterized. The P^{exo} foci area (**a**) and intensity (**b**) of the successful and stalled infections shown in Fig. 3a,b and Supplementary Video 3 were quantified. Foci were assessed post splitting from 3 hpi onwards, every hour, till 15 hpi. **c**, Following VF formation in RSV infected P^{exo}-fluoro cells, there is a rapid increase in foci. These are vRNP progeny that stain positive for RSV genomic RNA ((-)vRNA) by smFISH. **d, e**, Cells where a successful RSV infection was established were assessed for viral mRNA expression (**d**) and viral protein levels (**e**) in P^{exo}-fluoro cells at 24 hpi. **f, g, h**, M2-1^{exo}-fluoro allowed visualization of Inclusion Body-Associated Granules (IBAGs), internal substructures present in a subset of RSV VFs. (**f**) Schematic representation of the M2-1^{exo}-fluoro system. Here exogenous, fluorescently-tagged M2-1 is expressed in cells. Exogenous M2-1 encodes a SunTag peptide and the cells additionally co-express fluorescently-tagged STAb allowing its visualization. Combining with P^{exo}-fluoro (tagged with the ALFA-Tag, visualized by nanobody-ALFA-fluoro) and DARPin-P-fluoro allows visualization of IBAG formation during RSV infection. Two representative example image series (**g**) and quantification (**h**) assess the moment of IBAG formation in relation to RSV replication. **i**, The number of VFs present at 20 h post RSV infection was quantified. **j, k**, RSV infected cells that were positive for extracellular viral G protein were assessed for their viral RNA composition by smFISH. These cells always displayed viral antigenomes (**j**) as well as high levels of viral mRNA transcripts (RSV whole transcriptome smFISH probe set) (**k**). **l, m, n, o, p**, Cell culture supplemented fluorescently-conjugated RSV G antibody (AbG-fluoro) identifies successful RSV infections (as defined by observing VFs and vRNP replication). (**l**) Schematic of the AbG-fluoro labeling approach. (**m**) P^{exo}-fluoro cells were infected with viral inoculum supplemented with increasing concentrations of AbG-fluoro and infection assessed at 6 hpi. Quantification shows no inhibitory effect on viral entry at concentrations up to 1:50 of the antibody compared to no antibody control. Each data point represents an imaged FOV. A dilution of 1:1000 was used for all experiments. (**n**) Representative images of extracellular AbG-fluoro accumulation on infected cells relative to the moment of vRNP fusion. (**o**) The timing of AbG-fluoro labeling relative to vRNP fusion is displayed by a cumulative incidence graph. Only infections with >1 vRNP were included to analyze vRNP fusion. (**p**) For infections with >1 vRNP, AbG-fluoro positivity is exclusively observed in infections where vRNPs have fused. All cells were imaged for at least 20 hpi. **q, r**, The potential variations in infection by virions carrying DARPin-P$^+$ and DARPin-P$^-$ vRNPs were assessed. (**q**) Cumulative incidence graphs showing the time from inoculum addition to vRNP entry for both DARPin-P$^+$ and DARPin-P$^-$ virions. (**r**) The number of vRNPs per infected cell for DARPin-P$^+$ and DARPin-P$^-$ virions was quantified. Comparing DARPin-P$^+$ and DARPin-P$^-$ virions show no significant difference across all foci numbers. **s, t**, Infection success for DARPin-P$^-$ (**s**) and DARPin-P$^+$ (**t**) infections were assessed in relation to the number of vRNPs and displayed as cumulative incidence graphs. **u**, DARPin-P state of successfully infected cells was assessed. All VFs in these infections are DARPin-P positive. (**o, q, s, t**) Lines and shaded areas indicate mean and SE, respectively. (**m**) Ordinary one-way ANOVA with Dunnett's multiple comparisons test used for statistical analysis. (**r**) Two-way ANOVA with Tukey's multiple comparisons test used for statistical analysis. (**c, d, e, j, k, n, u**) Scale bar, 10 μm. (**g**) Scale bar, 2 μm. (**n**) Time, h: min. The number of experimental repeats and fluorophores used are listed in Supplementary Table 1.

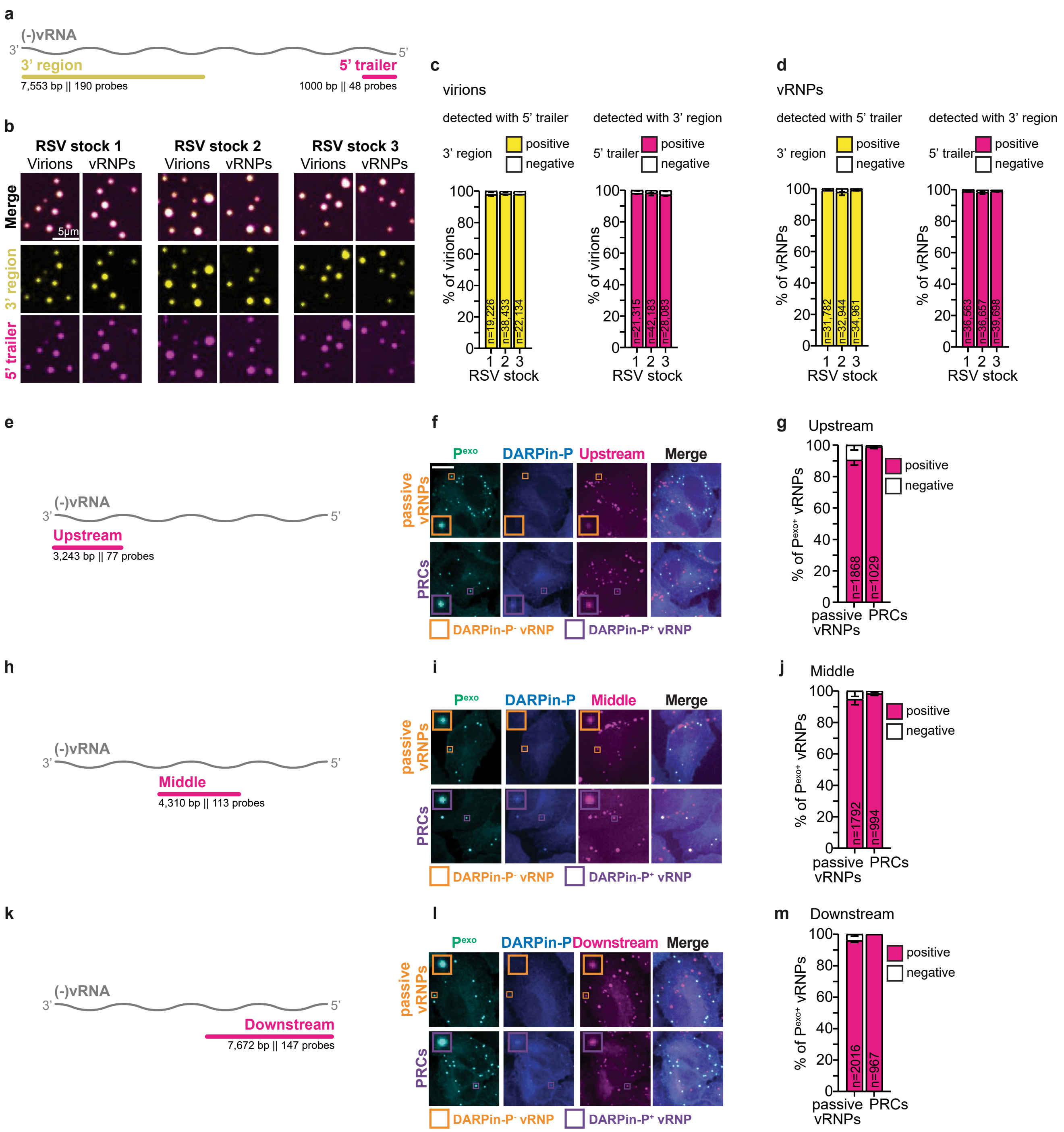

Extended Data Fig. 6 | Assessing vRNA integrity in RSV stocks. The integrity of genomic viral RNA ((-)vRNA) was assessed by smFISH. Probe sets targeting different (-)vRNA regions allowed identification of fully intact vRNPs and those missing genomic regions. **a, b, c, d**, Three RSV WT stocks were analyzed for defective viral genomes (DVGs) using a probe set targeting the 5′ trailer sequence. Many copy-back DVGs (cbDVGs), the predominant DVG type in RSV, contain break/rejoin events near the 5′ end of the genome, deleting large regions of the 3′ (-)vRNA[28,29]. Targeting the 5′ trailer region thus enables sensitive and specific detection of cbDVGs. Coupling the 5′ probe set with a 3′ region probe set distinguishes intact RSV genomes from DVGs. Virions and vRNPs were analyzed on glass. Virions were detergent treated to release vRNPs (see Methods). (**a**) Schematic of the smFISH-based DVG detection strategy. (**b**) Representative images showing probe labeling of virions and vRNPs in three RSV WT stocks. Colocalization of probe signals was quantified for virions (**c**) and vRNPs (**d**). **e, f, g, h, i, j, k, l, m**, The (-)vRNA integrity for passive vRNPs and PRCs in infected cells was assessed. Schematics (**e, h, k**), representative images (**f, i, l**) and quantification (**g, j, m**) for smFISH probe sets targeting upstream, middle and downstream regions of the (-)vRNA, respectively, are shown. Assessments were performed 4 h after viral inoculum addition in P^{exo}-fluoro/DARPin-P-fluoro cells. To prevent infection progression, the translation inhibitor emetine was added simultaneously with virus inoculation. (**f, i, l**) Scale bar, 10 µm. The number of experimental repeats and fluorophores used are listed in Supplementary Table 1.

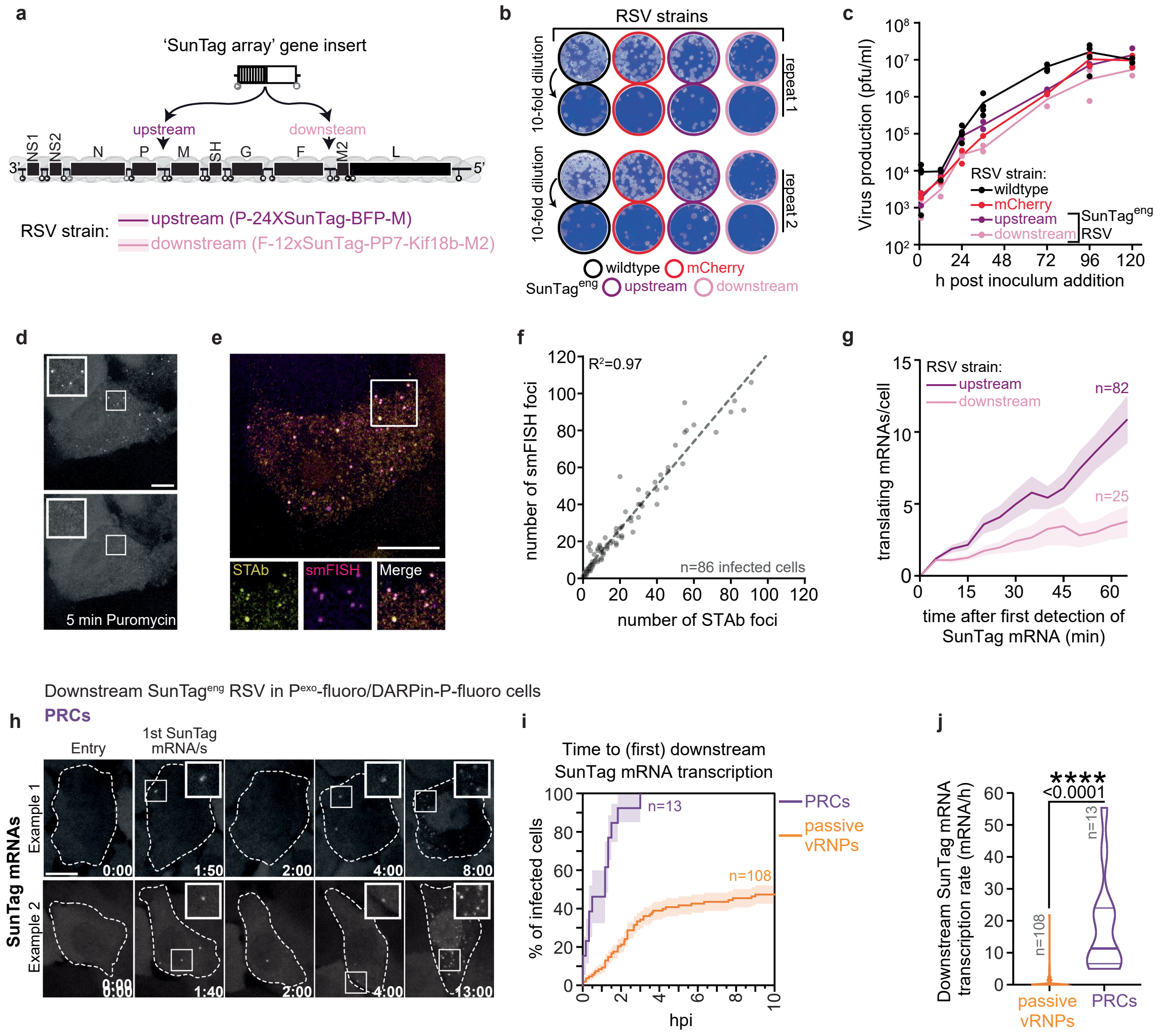

Extended Data Fig. 7 | Validation of the SunTag$^{\text{eng}}$ RSV strains that allow real-time visualization of viral mRNA expression. a, Schematic illustrating the upstream and downstream insertion locations of the 'additional SunTag genes' in the two SunTag$^{\text{eng}}$ RSV strains. **b, c**, Viral growth analysis based on plaque assays were carried out to determine the fitness of the engineered RSV strains compared to the WT. (**b**) Representative images of observed plaques 6 days post viral inoculation. For each viral strain, 2 repeats, each with 2 inoculum dilutions are shown. (**c**) Quantification of growth assay. Line connects mean of experimental repeats (dots). **d**, Representative images of time-lapse videos of cells expressing STAb-fluoro after infection with upstream SunTag$^{\text{eng}}$ RSV prior to (top panel) and following (bottom panel) puromycin administration. **e, f**, STAb-fluoro foci observed with the SunTag$^{\text{eng}}$ RSV strains were assessed by smFISH. (**e**) Representative images of smFISH for SunTag mRNA foci and STAb-fluoro foci in the same infected cell for the upstream strain is shown. (**f**) Scatter dot plot quantifies the number of SunTag mRNAs (via smFISH) and translation sites (via STAb) in the same cells. Each dot indicates a single cell and dashed line indicates linear correlation with Pearson R^2 (top left). **g**, The number of translating SunTag mRNAs over time was quantified for both the upstream and downstream SunTag$^{\text{eng}}$ strains. Overall, both strains show an increase in the number of translating SunTag mRNAs over time. Mean (line) and SE (shaded area) are shown. **h, i, j**, Downstream SunTag$^{\text{eng}}$ RSV viral mRNA expression dynamics were assessed for infections originating from passive vRNPs and PRCs in cell lines labelling all vRNPs (P$^{\text{exo}}$-fluoro) and DARPin-P^{+} vRNPs (DARPin-P-fluoro). (**h**) Two representative image series from time-lapse videos of SunTag mRNAs in cells infected with a PRC are shown. (**i**) Cumulative incidence graphs depict the start of viral transcription for infections with passive vRNPs and PRCs. Mean (line) and SE (shaded area) are shown. (**j**) The transcription rate was calculated and plotted as violin plots with the median and quartiles shown (horizontal lines). Two-tailed unpaired Student's t-test was used for statistical analysis. (**d, e, h**) Scale bar, 10 µm. (**h**) Time, h: min. The number of experimental repeats and fluorophores used are listed in Supplementary Table 1.

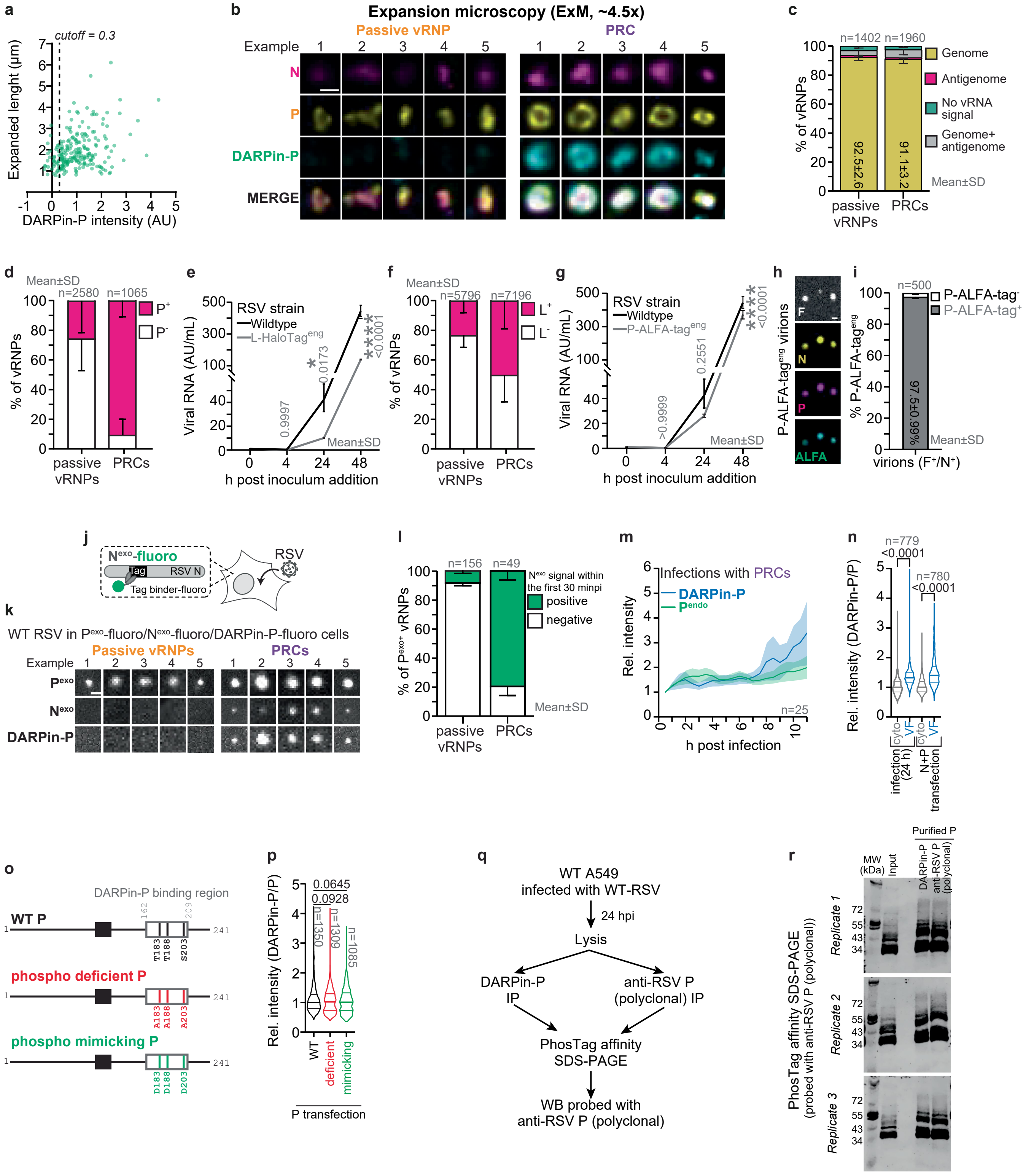

Extended Data Fig. 8 | See next page for caption.

Extended Data Fig. 8 | Further characterization of vRNPs, engineered RSV strains and DARPin-P interaction with P. a, b, Super-resolution imaging by expansion microscopy (ExM, ~4.5x) was performed on RSV infected cells to visualize the morphology of passive vRNPs and PRCs. (**a**) The DARPin-P-fluoro intensity cutoff used to classify vRNPs as wither DARPin-P$^-$ (passive vRNPs) or DARPin-P$^+$ (PRCs) is shown. (**b**) Additional representative ExM images are shown (see also Fig. 5a,b). **c**, The frequency of the different vRNA species in infecting vRNPs is quantified (related to Fig. 5c). **d**, Frequency of passive vRNPs and PRC foci that stains positive for P antibody is quantified (related to Fig. 5g,h). **e**, Viral growth analysis based on qPCR assays was carried out to determine the fitness of the engineered L-HaloTag^{eng} RSV strain compared to the WT strain. The reduced fitness was comparable to a previously reported RSV strain with an insertion in the L gene[72]. **f**, Frequency of passive vRNPs and PRC foci that are positive for L-HaloTag signal is quantified (related to Fig. 5j,k). **g, h, i**, The P-ALFA-Tag^{eng} RSV strain encodes for a single ALFA-tag in the P gene. This strain enables fluorescent-labelling of endogenous viral P protein (expressed from the viral genome) upon infection of cells expressing Nb ALFA-fluoro. (**g**) Viral growth analysis based on qPCR assays were carried out to determine the fitness of the engineered P-ALFA-Tag^{eng} RSV strain compared to the WT strain. Note, that the growth analysis for the WT strain is replicated from (**e**). Representative images (**h**) and quantification of the fraction of virions that are positive for the P-ALFA-tag (**i**) in P-ALFA-Tag^{eng} RSV virion population. The ALFA-tag in P-ALFA-Tag was detected using an anti-ALFA-tag antibody. **j, k, l**, The N^{exo}-fluoro system allows visualization of N^0 accumulation on vRNPs. (**j**) Schematic representation of the N^{exo}-fluoro system. Here exogenous, fluorescently-tagged N is expressed in cells. Exogenous N encodes a SunTag peptide and the cells additionally co-express fluorescently-tagged STAb allowing its visualization. Combining with P^{exo}-fluoro (tagged with the ALFA-Tag, visualized by nanobody-ALFA-fluoro) and DARPin-P-fluoro allows visualization of N^0 association with vRNPs during RSV infection. (**k**) Five representative example images of N^{exo}-fluoro labeling of vRNPs upon cytoplasmic entry. (**l**) Quantification of N^{exo} association in the first 30 min after a vRNP enters the host cell. **m**, Cells were infected with the P-ALFA-Tag^{eng} RSV strain, and the DARPin-P-fluoro and P^{endo}-fluoro intensities on PRCs were assessed over time. Foci intensity was normalized to the starting intensity. **n**, The ratio of DARPin-P to P intensity was quantified in the cytoplasm and in VFs, either following natural RSV infection or for pseudo-VFs induced by N and P transfection in uninfected cells. **o, p, q, r**, Effect of RSV P phosphorylation on the DARPin-P association with P was evaluated. The effect of phosphorylation on DARPin-P binding to P was evaluated by mutating phosphorylation sites within the DARPin-P binding region of P. (**o**) Schematic highlighting the assessed phosphorylation sites. (**p**) Quantification of DARPin-P intensity relative to P intensity was performed for wild-type and phospho-mutants of P. (**q, r**) DARPin-P recognition of alternatively phosphorylated isoforms of P was assessed by PhosTag gels. Experimental schematic is shown in (**q**), and three independent gel replicates are presented in (**r**). (**e, g, m**) Mean (line) and SE (shaded area) are shown. (**e, g**) Two-way ANOVA with Dunnett's multiple comparisons test was used for statistical analysis. (**n, p**) Kruskal-Wallis test with Dunn's multiple comparisons test used for statistical analysis. (**b, h, k**) Scale bar, 1 µm. Note, for (**b**) which were subjected to ~4.5 fold expansion, the1 µm scale bar in the image corresponds to ~222 nm before expansion. The number of experimental repeats and fluorophores used are listed in Supplementary Table 1.

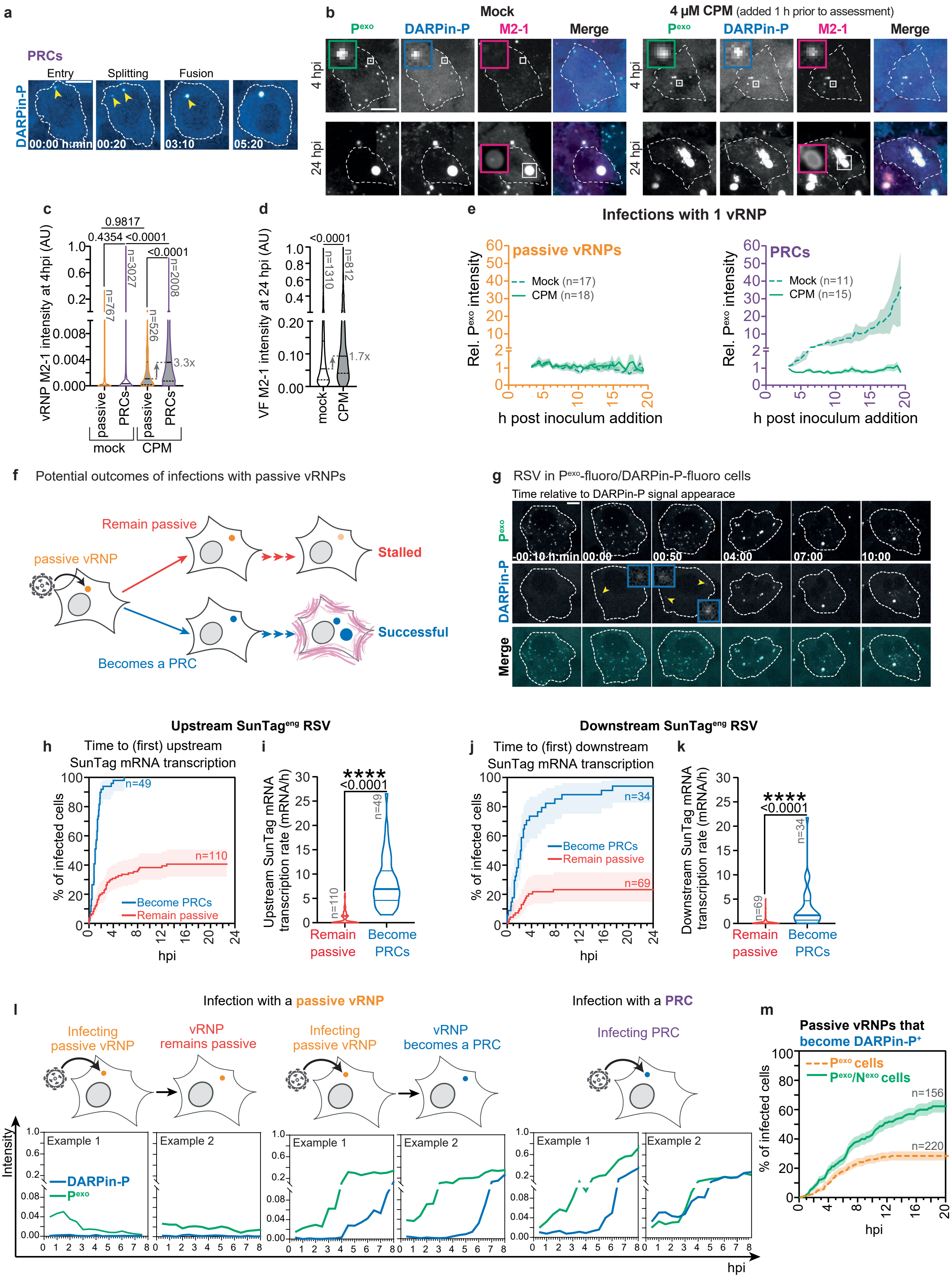

Extended Data Fig. 9 | See next page for caption.

Extended Data Fig. 9 | Additional analysis of the VF-like characteristics of PRCs and the conversion of a subset of passive vRNPs into PRCs. **a**, Representative image series from time-lapse videos showing an infection with PRCs, where the vRNPs initially split, then subsequently fuse and increase in intensity. **b, c, d, e**, The effect of cyclopamine (CPM) on infecting vRNPs and VFs was assessed. (**b**) Representative images of P^{exo}-fluoro/DARPin-P-fluoro cells infected with WT RSV and treated with CPM for 1 h prior to fixation. Images show infecting vRNPs (4 hpi) and VFs (24 hpi). M2-1 antibody staining was used to evaluate CPM effects. Quantification of M2-1 intensities on vRNPs (**c**) and VFs (**d**) is shown. (**e**) Time-lapse imaging following infections initiated by a single vRNP in control and CPM-treated conditions, showing P^{exo}-fluoro intensities normalized to the initial intensity of the foci. **f, g**, Infections with passive vRNPs were further characterized. (**f**) Schematic highlighting the potential outcomes of passive vRNP infections. (**g**) Representative image series from a time-lapse video showing an infection with multiple passive vRNPs where one vRNP becomes a PRC post cell entry. Yellow arrowheads indicate first appearance of DARPin-P positivity. **h, i, j, k**, Analysis of the transcriptional activity of passive vRNP infections that either become PRCs or remain passive. Cumulative incidence graphs depicting the start of viral transcription (**h**) and violin plots showing the transcription rate (**i**) for the upstream SunTag^{eng} RSV strain. Cumulative incidence graphs depicting the start of viral transcription (**j**) and violin plots showing the transcription rate (**k**) for the downstream SunTag^{eng} RSV strain. **l**, Example intensity-time traces of vRNP P^{exo}-fluoro and DARPin-P-fluoro foci intensities are shown for the following 3 infection scenarios: (1) infections arising from passive^{-} vRNPs that remain passive, (2) infections from passive vRNPs that becomes a PRC during infection and, (3) infections with a PRC. **m**, Cumulative incidence graphs showing the kinetics of passive vRNPs becoming PRCs during infection in cells expressing only exogenous P or expressing both exogenous P and exogenous N. Note that the data for P^{exo} cells is replicated from Fig. 6n for comparison purposes. (**e, h, j, m**) Mean (line) and SE (shaded area) are shown. (**c, d, i, k**) The median and quartiles are shown (horizontal lines) (**c**) One-way ANOVA with Tukey's multiple comparisons test was used for statistical analysis. (**d, i, k**) Two-tailed unpaired Student's t-test was used for statistical analysis.(**a, b, g**) Scale bars, 10 µm. (**a, g**) Time, h: min. The number of experimental repeats and fluorophores used are listed in Supplementary Table 1.

nature portfolio

Corresponding author(s): Marvin E. Tanenbaum

Last updated by author(s): Oct 6, 2025

Reporting Summary

Nature Portfolio wishes to improve the reproducibility of the work that we publish. This form provides structure for consistency and transparency in reporting. For further information on Nature Portfolio policies, see our Editorial Policies and the Editorial Policy Checklist.

Statistics

For all statistical analyses, confirm that the following items are present in the figure legend, table legend, main text, or Methods section.

n/a	Confirmed	
☐	☒	The exact sample size (*n*) for each experimental group/condition, given as a discrete number and unit of measurement
☐	☒	A statement on whether measurements were taken from distinct samples or whether the same sample was measured repeatedly
☐	☒	The statistical test(s) used AND whether they are one- or two-sided *Only common tests should be described solely by name; describe more complex techniques in the Methods section.*
☒	☐	A description of all covariates tested
☐	☒	A description of any assumptions or corrections, such as tests of normality and adjustment for multiple comparisons
☐	☒	A full description of the statistical parameters including central tendency (e.g. means) or other basic estimates (e.g. regression coefficient) AND variation (e.g. standard deviation) or associated estimates of uncertainty (e.g. confidence intervals)
☐	☒	For null hypothesis testing, the test statistic (e.g. *F*, *t*, *r*) with confidence intervals, effect sizes, degrees of freedom and *P* value noted *Give P values as exact values whenever suitable.*
☒	☐	For Bayesian analysis, information on the choice of priors and Markov chain Monte Carlo settings
☒	☐	For hierarchical and complex designs, identification of the appropriate level for tests and full reporting of outcomes
☐	☒	Estimates of effect sizes (e.g. Cohen's *d*, Pearson's *r*), indicating how they were calculated

Our web collection on statistics for biologists contains articles on many of the points above.

Software and code

Policy information about availability of computer code

Data collection

Imaging experiments were performed on the following systems:
1. Nikon TI2 inverted microscope equipped NIS Elements AR software (version 5.21.03).
2. Zeiss LSM900 microscope equipped with an Airyscan2 detector. Images were collected in Multiplex SR-2Y mode as z-stacks with 0.120 µm spacing.

NMR experiments were carried out on a Bruker 800 MHz Avance III spectrometer equipped with a TCI cryoprobe, data processed with TopSpin 4.0 software (Bruker) and analyzed with CcpNMRAnalysis software.

BLI experiments were performed using an Octet Red 96e system (Fortebio) and real-time binding kinetics were analyzed and calculated using the Octet Red software package.

FACS analysis was performed using Cytoflex S (Beckman Coulter) and CytExpert software (2.5.0.77).

Analysis of IP peptides was carried out using an Ultimate 3000 nano-LC 1000 system coupled to an Orbitrap Exploris (Thermo Fisher Scientific). Phospho-enriched peptides were analyzed using an Ultimate 3000 nano-LC 1000 system coupled to an Orbitrap Ascend Tribrid Mass Spectrometer (Thermo Fisher Scientific). Mass spectra were acquired in the Orbitrap (350-1400 m/z, resolution 60000, AGC target 3 x 106, maximum injection time 50 ms) in a data-dependent mode. Mass spectra were acquired in the Orbitrap (350-1400 m/z, resolution 60000, AGC target 3 x 106, maximum injection time 50 ms) in a data-dependent mode. For total IP samples, the top 40 most abundant peaks in the survey scan were fragmented using HCD (resolution 7500, AGC target 4 x104, maximum injection time 64 ms). For phospho-enriched samples, the top 30 most abundant peaks in the survey scan were fragmented using HCD (MS2 scans were acquired using the ion trap analyzer in Turbo mode, AGC target 2 x104, maximum injection time 35 ms).

Data analysis	For imaging data maximal intensity projections for all Z-slices (where multiple Z-slices were acquired) were generated using NIS Elements AR software (Nikon, 5.21.03)) and used for all downstream analyses. Image analyses were performed using ImageJ. For fixed cell experiments foci detection and foci integrated intensity quantification were performed using the ComDet (v.0.5.4) plugin (https://github.com/UU-cellbiology/ComDet). ExM image stacks were deconvolved in Huygens Professional (Scientific Volume Imaging, v20.10) using the Classic Maximum Likelihood Estimation (CMLE) algorithm with a theoretical PSF, allowing up to 40 iterations. Quantification was performed using Imaris software (Bitplane, v9.7.2). GraphPad prism (v 10.1.0) and Microsoft Excel were used for data visualization and statistical analysis. For video generation, the single-object-grid tool (https://github.com/TanenbaumLab/SingleObjectGrid) and the napari-animation plugin (https://napari.org/napari-animation/) was used. Identification and quantification of proteins from mass spectrometry were performed using Andromeda search engine implemented in MaxQuant under default parameters. R-package limma (3.52.4) was used for statistical analysis. AphaFold3 (https://alphafoldserver.com/, accessed on December 5, 2024) was used for protein complex prediction and Pymol (https://pymol.org/) for structure visualization.

For manuscripts utilizing custom algorithms or software that are central to the research but not yet described in published literature, software must be made available to editors and reviewers. We strongly encourage code deposition in a community repository (e.g. GitHub). See the Nature Portfolio guidelines for submitting code & software for further information.

Data

Policy information about availability of data

All manuscripts must include a data availability statement. This statement should provide the following information, where applicable:

- Accession codes, unique identifiers, or web links for publicly available datasets
- A description of any restrictions on data availability
- For clinical datasets or third party data, please ensure that the statement adheres to our policy

Further information and requests for resources and reagents should be directed to and will be fulfilled by the lead contact, Marvin E. Tanenbaum (m.tanenbaum@hubrecht.eu). The unique/stable reagents generated in this study are available from the lead contact with a completed Material Transfer Agreement. TThe plasmids generated in this study for the vRNP visualization tools (Pexo-SunTag, Pexo-ALFATag, M2-1exo-SunTag, Nexo-SunTag and DARPin-P-BFP) will be deposited in Addgene (at publication). A selection of raw imaging data has been made available through figshare.

Research involving human participants, their data, or biological material

Policy information about studies with human participants or human data. See also policy information about sex, gender (identity/presentation), and sexual orientation and race, ethnicity and racism.

Reporting on sex and gender	No human participants, their data or biological material has been used in this study.
Reporting on race, ethnicity, or other socially relevant groupings	No human participants, their data or biological material has been used in this study.
Population characteristics	No human participants, their data or biological material has been used in this study.
Recruitment	No human participants, their data or biological material has been used in this study.
Ethics oversight	No human participants, their data or biological material has been used in this study.

Note that full information on the approval of the study protocol must also be provided in the manuscript.

Field-specific reporting

Please select the one below that is the best fit for your research. If you are not sure, read the appropriate sections before making your selection.

☒ Life sciences ☐ Behavioural & social sciences ☐ Ecological, evolutionary & environmental sciences

For a reference copy of the document with all sections, see nature.com/documents/nr-reporting-summary-flat.pdf

Life sciences study design

All studies must disclose on these points even when the disclosure is negative.

Sample size	No sample size calculations were performed. The sample sizes for each experiment is given in Supplementary Table 1.

Data exclusions	No data was excluded.
Replication	Experiments were all performed in biological and technical independent replicates with comparable results. The sample size and number of independent replicates for each individual experiment is given in Supplementary Table 1. For the data included in Extended Data Fig. 5i, j and 7i, j an experimental repeat was analyzed independently by a researcher not involved in the original data acquisition or analysis. The results of this replication analysis was similar to the other replicates of the experiment and were collated and presented in the graphs.
Randomization	Randomization is not relevant in this study as all assessed phenotypes are all imaged in the same imaging well and the different outcomes arise during the experiment.
Blinding	Investigators were not blinded as the experimental work was predominantly performed by the same investigator that carried out the analysis.

Reporting for specific materials, systems and methods

We require information from authors about some types of materials, experimental systems and methods used in many studies. Here, indicate whether each material, system or method listed is relevant to your study. If you are not sure if a list item applies to your research, read the appropriate section before selecting a response.

Materials & experimental systems

n/a	Involved in the study	
☐	☒	Antibodies
☐	☒	Eukaryotic cell lines
☒	☐	Palaeontology and archaeology
☒	☐	Animals and other organisms
☒	☐	Clinical data
☒	☐	Dual use research of concern
☒	☐	Plants

Methods

n/a	Involved in the study	
☒	☐	ChIP-seq
☐	☒	Flow cytometry
☒	☐	MRI-based neuroimaging

Antibodies

Antibodies used	RSV Glycoprotein F Antibody (11-2-F3) [DyLight 550] - bio techne (NOVUS Biologicals) - Cat# NBP2-50412R RSV Glycoprotein F Antibody (11-2-F3) [Alexa Fluor® 488] - bio techne (NOVUS Biologicals) - Cat# NBP2-50412AF488 RSV Nucleoprotein Antibody (RSV3132 (B023)) - bio techne (NOVUS Biologicals) - Cat# NB100-64752 RSV Phosphoprotein Antibody (2H102) [Janelia Fluor® 646] - bio techne (NOVUS Biologicals) -Cat# NBP2-50276JF646 RSV Glycoprotein G Antibody (133) [Janelia Fluor® 646] bio techne (NOVUS Biologicals) -Cat# NBP2-50411JF646 RSV Glycoprotein G Antibody (133) [Alexa Fluor® 405] - bio techne (NOVUS Biologicals) - Cat# NBP2-50411AF405 RSV M2-1 Protein Antibody (5H5) [Alexa Fluor® 647] - bio techne (NOVUS Biologicals) - Cat# NBP2-50481AF647 FluoTag®-X2 anti-ALFA [Atto 488] - NanoTag Biotechnologies - Cat# N1502 rabbit anti-P antiserum (Ref: Castagné, N. et al. Biochemical characterization of the respiratory syncytial virus P–P and P–N protein complexes and localization of the P protein oligomerization domain. Journal of General Virology 85, 1643-1653 (2004)).
Validation	For all antibodies detecting viral proteins a negative control (uninfected) was included in the experiments. The false-positive foci detection rate for all antibodies used is negligible (see Extended Data Fig. 2a).

Eukaryotic cell lines

Policy information about cell lines and Sex and Gender in Research

Cell line source(s)	HEp-2 cells provided by the Rameix-Welti lab (ATCC, cat. no. CCL-23) BHK-21 cells (clone BSRT7/5) constitutively expressing the T7 RNA polymerase. Provided by the Rameix-Welti lab. A549 cells, Tanenbaum lab (ATCC, cat. no. CCL-185) HEK293T cells, Tanenbaum lab (ATCC, cat. no. CRL-3216) Vero cells, van Kasteren lab (ATCC, cat. no. CCL-81) Primary human nasal epithelial cells (HNECs) from healthy donors (Epithelix cat. no. EP51AB)
Authentication	The cell lines used were not authenticated.
Mycoplasma contamination	All cell lines were tested for mycoplasma contamination at multiple times during the study. Results were negative.
Commonly misidentified lines (See ICLAC register)	HEp-2 cells - are known to be derived via a HeLa contamination. ATCC recommends Hep-2 cells for RSV propagation.

Plants

Seed stocks	*Report on the source of all seed stocks or other plant material used. If applicable, state the seed stock centre and catalogue number. If plant specimens were collected from the field, describe the collection location, date and sampling procedures.*
Novel plant genotypes	*Describe the methods by which all novel plant genotypes were produced. This includes those generated by transgenic approaches, gene editing, chemical/radiation-based mutagenesis and hybridization. For transgenic lines, describe the transformation method, the number of independent lines analyzed and the generation upon which experiments were performed. For gene-edited lines, describe the editor used, the endogenous sequence targeted for editing, the targeting guide RNA sequence (if applicable) and how the editor was applied.*
Authentication	*Describe any authentication procedures for each seed stock used or novel genotype generated. Describe any experiments used to assess the effect of a mutation and, where applicable, how potential secondary effects (e.g. second site T-DNA insertions, mosiacism, off-target gene editing) were examined.*

Flow Cytometry

Plots

Confirm that:

☒ The axis labels state the marker and fluorochrome used (e.g. CD4-FITC).

☒ The axis scales are clearly visible. Include numbers along axes only for bottom left plot of group (a 'group' is an analysis of identical markers).

☒ All plots are contour plots with outliers or pseudocolor plots.

☒ A numerical value for number of cells or percentage (with statistics) is provided.

Methodology

Sample preparation	WT A549 cells and DARPin-P-fluoro cells were infected with RSV (0.001 PFU/cell). At 6 h cells were treated with the RSV fusion inhibitor,TMC353121. FACS assessment was carried out at 24 and 48 h following viral inoculum addition. Successfully infected cells were determined by the extracellular expression of RSV G protein. An hour prior to Flow cytometry, infected cells (and uninfected control cells) were incubated with RSV Glycoprotein G Antibody (133) - Janelia Fluor 646 (1:1000, in cell culture media) for 45 min at 37°C. After antibody incubation cells were rinsed in PBS, trypsinized, fixed (in suspension, with 4% paraformaldehyde for 10 min at RT with constant rotation) and suspended in PBS.
Instrument	Flow cytometry was performed using Cytoflex S (Beckman Coulter).
Software	Data was analyzed using CytExpert software (2.5.0.77).
Cell population abundance	The abundance of successfully infected cells was quantified based on RSV G protein staining. The gate for G positive and negative cells was set by using uninfected cells stained with the G protein antibody.
Gating strategy	Single cells were gated on FSC-A/FSC-H that were ensured to be free of debris by FSC-A/SSC-A assessment. Gating for RSV G protein antibody was determined by means of the uninfected control cell sample. The gating strategy is shown in Supplementary Fig. 1.

☒ Tick this box to confirm that a figure exemplifying the gating strategy is provided in the Supplementary Information.